UNIVERSITY OF CALIFORNIA, SAN DIEGO

Development of Solid-state NMR Spectroscopy for Membrane Proteins and the Application to Vpu from HIV-1

A dissertation submitted in partial satisfaction of the
requirements for the degree Doctor of Philosophy

in

Chemistry

by

Eugene Chun-Chin Lin

Committee in Charge:

Professor Stanley Opella, Chair
Professor Joseph Adams
Professor Patricia Jennings
Professor Judy Kim
Professor James McCammon

2015

The Dissertation of Eugene Chun-Chin Lin is approved, and it is acceptable in quality and form for publication on microfilm and electronically

_____

_____

_____

_____

_____
Chair

University of California, San Diego

2015

DEDICATION

To my parents, Shaw-Tao Lin and Pei-Jei Lin-Chiou,

and my sister, Iris Lin,

who provides their endless support over years.

TABLE OF CONTENTS

LIST OF ABBREVIATIONS

^{1}H	Proton
^{13}C	Carbon - 13
^{15}N	Nitrogen - 15
14-O-PC	1,2-di-O-tetradecyl-*sn*-glycero-3-phosphocholine
AP1	Adaptor protein 1
BST-2	Bone marrow stromal antigen 2 p
CCR7	C-C chemokine receptor type 7
CD4	Cluster of differentiation 4
COV	Covariance
CP	cross-polarization
CS	Compressed sensing
CSA	Chemical shift anisotropy
CW	Continuous wave
CXCR1	C-X-C chemokine receptor type 1
Cyto	Cytoplasmic
D-PISEMO	Dual- Polarization Inversion Spin Exchange Modulated Observation
Da	Dalton
DAAP	Dipolar assisted assignment protocol
DARR	dipolar assisted rotational resonance
DCP	double-cross-polarization
DEC	Decoupling

DHPC	1,2-dihexanoyl-*sn*-glycero-3-phosphocholine
DMPC	1,2-dimyristoyl-*sn*-glycero-3-phosphocholine
DNA	deoxyribonucleic acid
DNP	Dynamic nuclear polarization
ER	Endoplasmic reticulum
FID	Free induction decay
FT	Fourier transform
gp120	Envelope glycoprotein GP120
gp160	Envelope glycoprotein GP160
GPCR	G-protein coupled receptor
HETCOR	Heteronuclear correlation
HIV-1	Human immunodeficiency virus, type 1
INEPT	Insensitive Nuclei Enhanced by Polarization Transfer
IR	Infrared
IST	Iterative soft thresholding
LG	Lee-Goldberg
LP	Linear prediction
MAGC	modified Alderman Grant coil
MAS	Magic-angle-spinning
MaxEnt	Maximum entropy reconstruction
MDD	Multi-dimensional decomposition
MerF	Mercury transporter F
MINT	maximum entropy interpolation

MMHH	mismatched Hartmann-Hahn
MRI	Magnetic resonance imaging
NAL	N-acetyl-leucine
NAV	N-acetyl-valine
NCACX	^{15}N chemical shift / ^{13}Ca chemical shift / ^{13}C chemical shift
NCOCX	^{15}N chemical shift / ^{13}CO chemical shift / ^{13}C chemical shift
NK-cell	Natural killer cell
NKG2D	Natural killer group 2, member D
NMR	Nuclear magnetic resonance
NP-hard	Non-deterministic Polynomial-time hard)
NTB-A	NK-T-B antigen
NUS	Non-uniform sampling
OS	Oriented sample
PDB	Protein data bank
PDSD	proton-driven spin diffusion
PISEMA	Polarization Inversion Spin Exchange at the Magic Angle
PRE	paramagnetic relaxation enhancement
RA	Rotationally aligned
RDC	Residual dipolar coupling
REP-CP	repetitive cross-polarization
RF	Radiofrequency
S/N	Signal-to-noise
SLF	Separated-local-field

SPINAL-16	small phase incremental alternation, with 16 steps
t1	Incremented time interval in a two-dimensional experiment
t2	Signal acquisition interval in a two-dimensional experiment
TGN	trans-Golgi network
TM	Transmembrane
TSAR	Third-spin assisted polarization transfer
US	uniform sampling
Vpu	Viral protein U
WD-PISEMO	Window-detected D-PISEMO

LISTS OF FIGURES

LIST OF TABLES

ACKNOWLEDGEMENTS

First, I would like to thank Professor Stanely J. Opella providing me such opportunity to join his research group. I not only enjoy benefits from one of the best solid-state NMR centers in the world, but also learn the vision and attitude from Professor Opella. He dedicates his research career to develop solid-state NMR in order to understand structures of membrane proteins presenting in their native environments, for over thirty years. Both his determination and enthusiasm are valuable for a young researcher like me. I would also like to thank other members in my thesis committee, Professor Joseph Adams, Professor Patricia Jennings, Professor Judy Kim, and Professor J. Andrew McCammon, for their guidance, supportiveness and openness to the discussion of scientific questions.

I also would like to thank everyone working in Opella research group. They are always helpful and supportive. Special acknowledgement must be given to Dr. Chin (Albert) H. Wu for teaching me a lot the solid-state NMR spectroscopic techniques when I first joined the group. Albert is knowledgeable in NMR spectroscopy and has been always supportive in both research and personal life. Dr. Christopher V. Grant and Dr. Bibhuti B. Das are always helpful and guiding lots of NMR techniques (from hardwares to pulse sequences) in NMR facility (the Bubble).

Hua Zhang not only teaches and helps me a lot in Vpu project. More importantly, we joined the group in the same year, and we grew up, learned, and trained together as Ph.D.. All the process and memories are valuable for me. I also would like to thank Professor Francesca Marassi, Dr. Sang Ho Park, Dr. Yan Wang,

who worked on Vpu project and established the protocols of Vpu expression and purification. Thanks for other members: Dr. Anna De Angelis, Dr. Xuemei Huang, Dr. Anthony Mrse, Dr. Ye Tian, Lindasy Dawson, Mignon Chu, Jasmina Radiocic, Sabrina Berkamp, Vivian Wang, Mitchell Zhao, and the former group members: Dr. Yuan Yang, Dr. Gabriel Cook, Dr. Woo Sung Son, Dr. Henry Nothnagel, Dr. Dongtao Cui, Dr. George Jiaozhi Lu and Yanwen Mai. I also want to thank Elena Vitoshka-tarasov for her wonderful jobs as the administrative assistant of the laboratory.

Chapter 2, in full, is a reprint of the material "^{1}H-^{13}C separated local field spectroscopy of uniformly ^{13}C labeled peptides and proteins" as it appears in J. Magn. Reson. 206(1):105-111 by Lin EC, Wu CH, Yang Y, Grant CV, and Opella, SJ. The thesis author was the primary author of the paper.

Chapter 3, in full, is a reprint of the material "^{1}H assisted ^{13}C/^{15}N heteronuclear correlation spectroscopy in oriented sample solid-state NMR of single crystal and magnetically aligned samples" as it appears in J. Magn. Reson. 221(1):37-44 by Lin EC, Opella SJ. The thesis author was the primary author of the paper.

Chapter 4, in full, is a reprint of the material "Sampling Scheme and Compressed Sensing Applied to Solid-State NMR Spectroscopy" as it appears in J. Magn. Reson. 237:40-48 by Lin EC, Opella SJ. The thesis author was the primary author of the paper.

Chapter 5, in full, is a reprint of the material "Covariance Spectroscopy in High-Resolution Multi-dimensional Solid-state NMR" as it appears in J. Magn. Reson. 239:57-60 by Lin EC, Opella SJ. The thesis author was the primary author of the paper.

Chapter 6 is currently being prepared for submission for publication of the material.

VITA

2006 Bachelor of Science, National Chi Nan University, Nantou County, Taiwan

2008 Master of Science, National Chung Hsing University, Taichung City, Taiwan

2015 Doctor of Philosophy, University of California, San Diego

PUBLICATIONS

Lin E. C. and Opella, S. J. *Covariance Spectroscopy in High-Resolution Multi-dimensional Solid-state NMR*. J. Magn. Reson. 2014; 239: 57-60. PMCID: PMC3929046

Das B. B., **Lin E. C.**, and Opella, S. J. *Experiments Optimized for Magic Angle Spinning and Oriented Sample Solid-State NMR of Proteins*. J. Phys. Chem. B 2013; 117(41): 12422-12431 PMCID: PMC3846429

Lin E. C. and Opella S. J. *Sampling Scheme and Compressed Sensing Applied to Solid-State NMR Spectroscopy*. J. Magn. Reson. 2013; 237: 40-48 PMCID: PMC3851314

Chien M.-P., Thompson M.P., **Lin E. C.**, and Gianneschi N.C. *Fluorogenic Enzyme-Responsive Micellar Nanoparticles.* Chem. Sci. 2012; 3(9): 2690-2694. PMCID: PMC3622269 (**Cover**)

Lin E. C. and Opella S. J. *^{1}H assisted $^{13}C/^{15}N$ heteronuclear correlation spectroscopy in oriented sample solid-state NMR of single crystal and magnetically aligned samples*. J. Magn. Reson. 2011; 211(1): 37-44. PMCID: PMC3236683

Lin E. C., Wu C. H., Yang Y., Grant C. V., and Opella, S. J. *^{1}H-^{13}C separated local field spectroscopy of uniformly ^{13}C labeled peptides and proteins.* J. Magn. Reson. 2010; 206(1): 105-111. PMCID: PMC2926282

Tang H.-Y., **Lin C.-C.**, Wang L.-S., Yang W.-C., Liao K.-H., Li F.-Y., and Liao M. Y. *Quantum size effect on ^{67}Zn-NMR measurements of ZnS nanoparticles*. Phys. Rev. B 2008; 77: 165420-165425.

ABSTRACT OF THE DISSERTATION

Development of Solid-state NMR Spectroscopy for Membrane Proteins and the Application to Vpu from HIV-1

by

Eugene Chun-Chin Lin

Doctor of Philosophy in Chemistry

University of California, San Diego, 2015

Professor Stanley Opella, Chair

Solid-state nuclear magnetic resonance (NMR) spectroscopy is a robust method to solve the structures of membrane proteins in their native bilayer environments. Two systems have been well established: oriented samples (OS) are referred to proteins incorporated in the magnetic aligned bicelles, and rotationally aligned (RA) samples are referred to proteins undergoing fast rotational diffusion in proteoliposomes. ^{1}H-^{15}N and ^{1}H-^{13}C dipolar couplings are measured as the angular restraints for the structure calculations. New separated-local-field experiment, Dual-

PISEMO, is developed for OS solid-state NMR to measure ^{1}H-^{13}C dipolar couplings of the uniformly ^{13}C labeled proteins, which provide both backbone and side-chain conformations. In order to obtain the full assignments and restraints in OS solid-state NMR, ^{1}H-irradiations with mismatched conditions are implemented to improve the crucial step: the magnetization transfer between ^{15}N and ^{13}C. Non-uniform sampling (NUS) is an alternative approach to further the experimental time of high-dimensional solid-state NMR experiments. Compressed sensing (CS) is able to reconstruct the spectra with 25 ~ 33% of data with the optimized sampling scheme, and covariance spectroscopy provides promising results with alternative States sampling scheme, which requires 50% of data or less. Viral protein "u" (Vpu) from HIV-1 is a type I membrane protein consisting of a transmembrane domain and a cytoplasmic domain, which are associated with different biological activities to enhance viral infectivity. It is essential to determine the three-dimensional structure of Vpu in order to understand its mechanisms in the molecular level and to develop new classes of anti-viral drugs. Magic-angle spinning (MAS) experiments providing high-sensitivity and high-resolution spectra, are implemented to study Vpu incorporated into proteoliposomes. ^{15}N, ^{13}C chemical shift and ^{1}H-^{15}N, ^{1}H-^{13}C dipolar couplings are measured and converted to equivalent structural restraints.

Chapter 1 Introduction to solid-state NMR and viral protein U (Vpu)

1.1 Introduction

Solid-state nuclear magnetic resonance (NMR) is the must suitable technique to determine the high-resolution, three-dimensional structures of non-engineered and full-length membrane proteins presenting in the near-native environments, including the phospholipid bilayers, pH and temperature[1-8]. Membrane proteins play roles as receptors, transporters, and enzymes associated with biological membranes[9]. It is essential to understand the three-dimensional structures of proteins for interpreting and predicting the their functions, and discovering new drugs. 25% ~ 30% of proteins from the human genome are predicted as integral membrane proteins, which corresponds to about 6,000 proteins[10]. However, only about 500 unique membrane proteins are listed in the Protein Data Bank (PDB) according to the membrane protein database (Membrane Proteins of known 3D Structure, http://blanco.biomol.uci.edu/mpstruc/), and most of them are not from the human genome, indicating the needs for developing new technologies. G-protein coupled receptors (GPCRs) are the important receptors on cell surfaces, which are the targets of 30% of drugs[11]. C-X-C chemokine receptor type 1 (CXCR1), one of GPCRs, has 350 residues and seven transmembrane domains, and the structure of CXCR1 has been solved by solid-state NMR[3], suggesting that this technique can be applied to 40K Da proteins at least.

The overall goals of developing NMR techniques are improving the efficiency and obtaining more angular and distance restraints for the structure calculations. These

improvements are made by the developments of hardware (magnet, console and probe), pulse sequences, and techniques of signal processing. Alternatively, dynamics nuclear polarization (DNP)[12-14] is an emerging technique to enhance the signals with polarizations from electrons, but more efforts are required to make DNP feasible under physiological conditions.

Two non-uniform sampling (NUS) methods were implemented to speed up the two- or higher-dimensional experiments by reducing the samplings in the indirect dimension (second or higher dimensions). Compressed sensing (CS)[15-19] has been successfully applied to magnetic resonance imaging (MRI) within this decade. We introduce CS to solid-state NMR, and improved the accuracy and the reproducibility of the reconstructions significantly by adding the uniform sampling region in the optimized sampling schemes. Covariance (COV) spectroscopy was first applied to two-dimensional infrared (IR) spectroscopy[20; 21], and then it was also applied to NMR spectroscopy[22-24]. COV gives better resolution and signal-to-noise (S/N) ratios in the indirect dimension comparing to traditional Fourier transform (FT) spectroscopy. Alternative States sampling scheme is proposed to further reduce the experimental time for COV NMR spectroscopy by 50% or more. These two methods can be generally applied to the two main techniques in solid-state NMR: oriented sample (OS) solid-state NMR[4; 7] and magic-angle-spinning (MAS) solid-state NMR[1; 2; 5].

The conventional strategy to solve the protein structures by OS solid-state NMR is measuring all the angular-dependent ^{1}H-^{15}N heteronuclear dipolar couplings and ^{15}N chemical shift anisotropies (CSAs) from the ^{15}N labeled proteins, and the backbone structures are determined from these angular restraints. Uniformly ^{13}C labeled proteins

allow us to characterize the side-chain conformations of proteins and provide stronger signals; however, ^{13}C homonuclear dipolar couplings result, which shorten the correlation time of the signals and reduces the resolution and S/N ratios. The Dual-PISEMO pulse sequence was developed for uniformly ^{13}C labeled samples; it suppresses both ^{1}H and ^{13}C homonuclear dipolar couplings, and simultaneously measures ^{1}H-^{13}C heteronuclear dipolar couplings. To fully assign the signals and measure all the restraints in a protein requires heteronuclear correlation experiments. The magnetization transfer between ^{15}N and ^{13}C is the crucial step. For the S = 1/2 nuclei, dipolar couplings are the major interactions in the solid-state NMR. ^{15}N-^{13}C dipolar couplings are relatively weak compared to other interactions in the spin system, and result in the inefficient magnetization transfers. ^{1}H-assisted $^{15}N/^{13}C$ transfer is introduced in to OS solid-state NMR, and provides a complementary method to the conventional magnetization transfer between ^{15}N and ^{13}C.

Rationally aligned (RA) solid-state NMR is applied to determine the structure of the viral protein U (Vpu) from HIV-1, which is composed of 81 amino acids, and has one helix in the transmembrane domain and two helices in the cytoplasmic domain. Vpu is relative dynamic comparing to other membrane proteins studied by solid-state NMR[3; 25-27], due to the fact that two-third of the protein is exposed in the cytoplasm, and this character could be related to the multiple functions of the cytoplasmic domain[28-33]. Even though Vpu is a small protein, it has been reported that several downmodulation mechanisms are induced by Vpu to interfere the immune system[28-37]. To solve the structure of Vpu, the proteins are reconstituted in the proteoliposomes, and the spectra are

acquired when the proteins are undergoing fast rotational diffusion along the bilayer normal[1; 5; 8].

1.2 Internal spin interactions in solid-state NMR

NMR spectroscopy mainly relies on the phenomenon that states of nuclear spins split under the magnetic field, known as Zeeman effect, which is proportional to the magnitude of the magnetic field and the gyromagnetic ratio of the nucleus. The energy gaps caused by Zeeman effect are in the radiofrequency range, and therefore, we can manipulate the spin states with sequences of radiofrequency pulses. When the motions of the samples are slower than the timescale of NMR, we consider them to be in the solid-state regime. Nuclear spins are sensitive to their environment, so by measuring the interactions of spins it is possible to acquire structural or dynamic information. The interactions for S = 1/2 are important for most biological systems, and by considering the natural abundance and the amounts in the biological samples we refer to ^{1}H as abundant spins, and ^{13}C and ^{15}N as dilute spins.

Chemical shifts are determined by the electron densities of the molecular structures, which provide the shielding for the nuclei to resist external magnetic field. In solution NMR, the isotropic chemical shift is the only part surviving from the averaging of fast tumbling. He frequencies are characteristic for different types of residues. Chemical shift anisotropies (CSAs) are observable when the isotropic tumbling rates are slow, which provides the angular-dependent restraints for determine the orientations of the residues.

J-coupling is the interaction correlated the nuclear pair through chemical bond. It is relatively small and is only observed when the tumbling rate is fast enough (i.e. solution samples), or the local structures are highly dynamic in the solid-state samples.

Dipolar coupling reflects the distance of the nuclear pair and the angle between the nuclear pair and the magnetic field. Heteronuclear dipolar couplings are negligible based on secular approximation in the laboratory frame, and only the homonuclear dipolar couplings are observable. ^{1}H homonuclear dipolar couplings are detrimental to the qualities of the spectra due to their strong interactions; and therefore, the goal is to remove these interactions in most situations. To build up heteronuclear dipolar couplings we need to bring them into the same rotation frame with the radiofrequency irradiations. Heteronuclear dipolar couplings are utilized to transfer the magnetizations when the spin temperatures are different. As the spin temperatures reach the equilibrium, oscillations of heteronuclear dipolar couplings provide the angular information in solid-state NMR.

1.3 Signal processing in NMR

Modern NMR spectroscopy relies on Fourier transform (FT) to increase both resolution and sensitivity, and window functions, zero filling, and linear prediction[38] are routinely used in FT-NMR spectroscopy to further improve the qualities of spectra. Linear prediction is applied to the truncated signals, which predict the signals from the sampled ones, and gives promising results when the S/N ratio is high. Non-uniform sampling (NUS) is an alternative way to speed up the experiments by reducing the samplings in the indirect dimensions, and several methods, such as, maximum entropy

reconstruction (MaxEnt)[39-41], multi-dimensional decomposition (MDD)[42; 43], compressed sensing (CS)[15-19], etc., have been applied to reconstruct the NMR signals. CS has been rapidly developed for magnetic resonance imaging (MRI) in this decade, and has been applied to NMR spectroscopy as well. CS only works well for sparse data, which is suitable for high-resolution NMR spectra, and for the non-sparse data, CS also works in their sparse representations, for instance, the frequency domain of wavelet transform. It has been shown that CS reconstructs a four-dimensional solution NMR experiment with 0.8% of data. Covariance (COV) spectroscopy[22-24] is another way to generate high-dimensional spectra, especially for homonuclear correlation spectra. Instead of transforming the signals from time domain to frequency domain, COV treats the time domain signals as trials, and obtains the correlations from statistical methods. The qualities of COV spectra are highly depend on the direct dimension, which usually has higher resolution and S/N ratio. Since the growth of experimental time is non-linear when we expand the dimensions of the NMR experiments, these NUS methods are necessary for high-dimensional experiments.

1.4 Oriented-sample (OS) solid-state NMR

Solid-state NMR origins from the stationary samples, such as single crystals and powder, and accompanying with the discovery of magnetically aligned biological samples, for instance, Pf1 and fd bacteriophages[44-46], bicelles[47], and macrodiscs[48], it has been applied to solve the structures of membrane proteins[4; 7]. OS solid-state NMR measures ^{15}N CSAs and ^{1}H-^{15}N dipolar couplings of the ^{15}N-labeled

proteins, and these tensors provide the angular restraints for the structure calculations. Separated-local-field (SLF) experiments have been developed for this purpose, such as, PISEMA[49; 50], SAMMY[51; 52], PISEMO[53], etc.. The concept of SLF experiments is removing the ^{1}H homonuclear dipolar coupling and observing the heteronuclear couplings by matching the rotating frames in the indirect dimension, and measures the CSAs in the direct dimension. The removal of ^{1}H homonuclear dipolar couplings is the key in SLF experiments. Several approaches are utilized in SLF experiments to bring the nuclei to the magic angle (54.7°) in the spin space in order to remove dipolar couplings: the Lee-Goldberg (LG)[54] condition refers to applying a continuous wave to the nuclei with an offset, which makes the overall effect of irradiation at the magic angle. LG irradiation is implemented in PISEMA. The magic angle can also be created with different combinations of the pulses. “Magic sandwich”[55], and multi-pulse[56] belonge to this category, and they are implemented in SAMMY and PISEMO, respectively. The assignments of signals are made by combining fitting of “PISA wheel”[57-59] and selectively ^{15}N labeled amino acids, and to increase the resolution or obtain more angular restraints three-dimensional SLF experiments and shiftless spectroscopy[60] have been developed.

1.5 Rotationally aligned (RA) solid-state NMR

The unoriented samples, such as, proteoliposomes, all possible orientations are presented, and therefore, they give broad signals in chemical shift and dipolar coupling dimensions, called powder pattern. ^{1}H-^{15}N or ^{1}H-^{13}C dipolar powder patterns from

proteins are highly similar, due to the powder averaging and the similarities of bond lengths, so the structure information is difficult to obtain under this condition. However, when the proteins are undergoing fast rotational diffusion (~10^6 s) about the bilayer normal[61], chemical shift and dipolar tensors perpendicular to the bilayer normal are averaged, and result in reduced chemical shift and dipolar powder patterns. Reduced dipolar powder patterns only depend on the bilayer normal, so the angular restraints are available under this condition. Series of symmetry-based pulse sequence[62-64] are introduced to recouple CSAs or heteronuclear dipolar couplings, and assignments are feasible with NCACX and NCOCX experiments or dipolar assisted assignment protocol (DAAP)[65]. RA solid-state NMR has been used to solve the 7-transmembrane protein, CXCR1 (350 residues)[3], showing the power of this technique.

1.6 Viral protein U (Vpu)

Viral protein U (Vpu) is one of the accessory proteins from HIV-1, which consists of one helix in the transmembrane (TM) domain and two helices in the cytoplasmic (Cyto) domain. Here we focus on NL4-3 strain, which belongs to group M and subtype B, and has 81 amino acids. Vpu has been reported to downmodulate several proteins to interfere immune system, such as, CD4[29; 66; 67], BST-2[28; 33], NTB-A[37; 68-70], CCR7[35], etc. The free form of CD4 can active the immune system, and CD4 can also bind to glycoprotein, gp160, which is the precursor of gp120. gp120 is found on the surface of HIV virus particles and is able to interact with the CD4 on the T-cells for transfection. BST-2 (also named tetherin, HM1.24, or CD 317) has glycophosphatidylinositol (GPI anchor) to hinder the mature virus particles and prevent

the virus release. One of the mechanisms to promote NK-cell degranulation is the coactivation of NTB-A and NKG2D protein complex on the surface of NK-cell. Once NTB-A is downmodulated, the survival rate of infected T-cell increases significantly. Downregulation of CCR7 by Vpu was reported recently, and CCR7 plays an important role to home naïve T-cells to peripheral lymphoid organs.

To summarize theses interactions in the molecular level, we know that: (1) A14, A18, and W22 in the TM domain are the key residues to interact with the TM domains of CD4, NTB-A, BST-2, and CCR7, and the interactions of BST-2 and NTB-A have been confirmed by NMR experiments. These TM/TM interactions retains the downmodulated proteins in the cell organelles, for instance, CD4 is retained in endoplasmic reticulum (ER) and NTB-A, BST-2, and CCR7 are retained in trans-Golgi network (TGN). (2) S52 and S56 are the phosphorylation sites in the cytoplasmic domain, and once they are phosphorylated, cytoplasmic domain can recruit the ubiquitin-ligase complex to lead CD4 and BST-2 to proteasomes and lysosomes for degradations, respectively. (3) The leucine motif in the third helix can recruit adaptor protein 1 (AP1) and results in the mistraffic of BST-2 between TGN and endosomes.

Chapter 2 ^{1}H-^{13}C Separated Local Field Spectroscopy of Uniformly ^{13}C Labeled Peptides and Proteins

2.1 Abstract

By incorporating homonuclear decoupling on both the ^{1}H and ^{13}C channels it is feasible to obtain high-resolution two-dimensional separated local field spectra of peptides and proteins that are 100% labeled with ^{13}C. Dual-PISEMO (Polarization Inversion Spin Exchange Modulated Observation) can be performed as a conventional two-dimensional experiment, or with windowed detection as a one-dimensional experiment that offers flexibility as a building block for Shiftless and other multidimensional triple-resonance experiments with the inclusion of ^{15}N irradiation. The triple-resonance MAGC probe used to perform these experiments at 500 MHz is described.

2.2 Introduction

Extending the scope of uniform labeling with ^{15}N from molecular biology [71] to NMR spectroscopy [72] has opened up many opportunities for structural studies of DNA as well as proteins. The further extension of uniform labeling to include both ^{13}C and ^{15}N has led to the wide spread implementation of triple-resonance ^{1}H/^{13}C/^{15}N experiments in solution-state NMR [73] and in magic angle spinning (MAS) solid-state NMR [74] of

proteins. In contrast, there have been few applications of $^{1}H/^{13}C/^{15}N$ triple-resonance experiments to stationary solid samples, single crystals, or uniaxially aligned samples [75]. The principal reason is that the tight network of ^{13}C-^{13}C homonuclear dipole-dipole couplings in molecules where all carbon sites are 100% labeled with ^{13}C interferes with most solid-state NMR experiments, including the direct detection of single-line ^{13}C resonances and the evolution of ^{1}H-^{13}C dipolar couplings in various separated local field (SLF) spectroscopy [76]. These coupling undoubtedly interfere with a wide variety of other experiments as well.

We have made some progress in developing triple-resonance experiments for stationary samples by implementing homonuclear ^{13}C-^{13}C decoupling in indirect dimensions [77] and through the use of tailored ^{13}C labeling [78] to minimize the number of directly bonded pairs of ^{13}C nuclei with strong homonuclear dipole-dipole couplings. In this article we describe further development of $^{1}H/^{13}C/^{15}N$ triple-resonance experiments for solid-state NMR of stationary samples that involves the use of pulse sequences that integrate homonuclear ^{13}C-^{13}C decoupling into the previously described PISEMO (Polarization Inversion Spin Exchange Modulated Observation) version [53] of SLF experiments. By simultaneously employing both ^{1}H-^{1}H and ^{13}C-^{13}C homonuclear decoupling in the pulse sequence, experiments can be performed on 100% uniformly ^{13}C labeled samples. Further, these experiments have the option of enabling the ^{13}C magnetization to be detected in the windows of the multiple-pulse cycle, reducing the dimensionality and serving as an essential building block for Shiftless NMR experiments where heteronuclear dipolar couplings provide all of the frequency dimensions [60].

The dipole-dipole couplings between two nuclei are manifested as doublets in solid-state NMR spectra when they are either spatially isolated [79] or when homonuclear decoupling procedures [54; 56] are applied. Pulse sequences that perform homonuclear decoupling without removing the chemical shift or heteronuclear dipolar interactions are of particular interest for structural studies, since the principles of selective averaging enable the measurement of structural constraints. SLF experiments in particular provide a powerful approach to obtaining distance and/or angular constraints for structure determination, since the heteronuclear dipole-dipole couplings associated with sites with resolved chemical shifts are measured [76]. For studies of proteins it is essential to use a high resolution version of SLF spectroscopy, such as PISEMA (Polarization Inversion Spin Exchange at the Magic Angle) [50], SAMPI4 [80], or PISEMO (Figure 2.1.A) [53] experiments because they provide narrow linewidths in both the chemical shift and heteronuclear dipolar coupling frequency dimensions. The vast majority of applications of these experiments have focused on isolated ^{1}H-^{15}N amide and ^{1}H-^{13}Cα sites in the backbone of proteins where the heteronuclear dipolar couplings of these two-spin systems are observed as doublets; the pulse sequences perform homonuclear ^{1}H-^{1}H decoupling, and the homonuclear couplings among the 'dilute' ^{15}N or ^{13}C sites are negligible and can be ignored. Because the bond lengths are constant, the angular dependence of the frequency splittings between the doublets provides valuable input for structure determinations in oriented-sample (OS) solid-state NMR [27; 81; 82].

In order to integrate ^{1}H/^{13}C/^{15}N triple-resonance spectroscopy into OS solid-state NMR of ^{13}C and ^{15}N labeled proteins, it is essential to deal with the ^{13}C-^{13}C homonuclear dipole-dipole couplings. ^{13}C-detected versions of solid-state NMR experiments are of

particular interest because of the potential for increased sensitivity over the more commonly employed ^{15}N-detected experiments. We are taking two distinct approaches in our studies of proteins. In one approach, tailored isotopic labeling [78] is employed, since this can provide samples where ^{13}C sites are not bonded to other ^{13}C nuclei, and hence do not have strong homonuclear dipole-dipole couplings. It has the advantage that it does allow for direct ^{13}C detection. However, it has several disadvantages. With most metabolic labeling schemes based on incorporation of specifically ^{13}C labeled precursors, for example glycerol, multiple samples are required in order to obtain signals from all carbon sites in the protein, and the limited number of vicinal ^{13}C labeled sites reduces the opportunities for homonuclear correlation experiments. Experiments can be performed on samples with about 25% of the carbon sites randomly labeled with ^{13}C, since on a statistical basis there are few pairs of ^{13}C bonded to each other in this situation, and all sites are equally represented in the spectra. However, not only does this suffer from an absence of vicinal ^{13}C labeled sites for making spectral correlations, but also, the overall dilution of the ^{13}C reduces the sensitivity to approximately one-fourth of what it would be if the same sites were 100% labeled with ^{13}C. Since the increase in sensitivity from direct ^{13}C detection compared to ^{15}N detection is about four-fold under comparable conditions, the dilution effectively cancels out any gain in sensitivity from the direct ^{13}C detection. The second approach is to implement pulse sequences that incorporate ^{13}C-^{13}C homonuclear decoupling at critical evolution periods [53; 60; 77; 83-85], and this is the subject of this article.

2.3 Results

The PISEMO pulse sequence diagramed in Figure 2.1.A differs from the original version [53] in that each cycle has four windows, instead of two, on the ^{13}C channel. The additional windows enable direct ^{13}C detection of frequency oscillations due to the evolution of the ^{1}H-^{13}C dipolar couplings with high sensitivity without degrading the line width of the signals in the dipolar coupling frequency dimension of the spectrum. Following conventional spin-lock Hartman-Hahn matched cross-polarization transfer of magnetization from ^{1}H to ^{13}C in the preparation period [86], both the ^{1}H and ^{13}C magnetization are spin-locked by the radiofrequency pulses to allow heteronuclear magnetization exchange during the evolution period. On the ^{1}H channel, an eight-pulse cycle is applied, the first half of which is a four-pulse WaHuHa cycle (X, -Y, Y, -X) [56], and the second half is a phase inverted four-pulse WaHuHa cycle (-X, Y, -Y, X). This eight-pulse cycle can be viewed as a "flip-flop" WaHuHa cycle, analogous to the irradiations applied in PISEMA [50] or SAMPI4 [80]. We have obtained similar results using other eight-pulse cycles such as MREV8 [87] and HW8 [88]. In general, these experiments are limited to eight-pulse cycles because the cycle times of longer pulse sequences prohibit the measurement of the largest ^{1}H-^{13}C heteronuclear dipolar couplings present in stationary solid samples. The original PISEMO pulse sequence was designed for the situation most commonly encountered in studies of proteins, where ^{1}H is the only type of abundant spin present, and one or a few ^{1}H are strongly coupled to a single spatially isolated ^{13}C or ^{15}N; as a result, only the effects of the multiple-pulse homonuclear decoupling sequence on the ^{1}H channel were taken into account in its design.

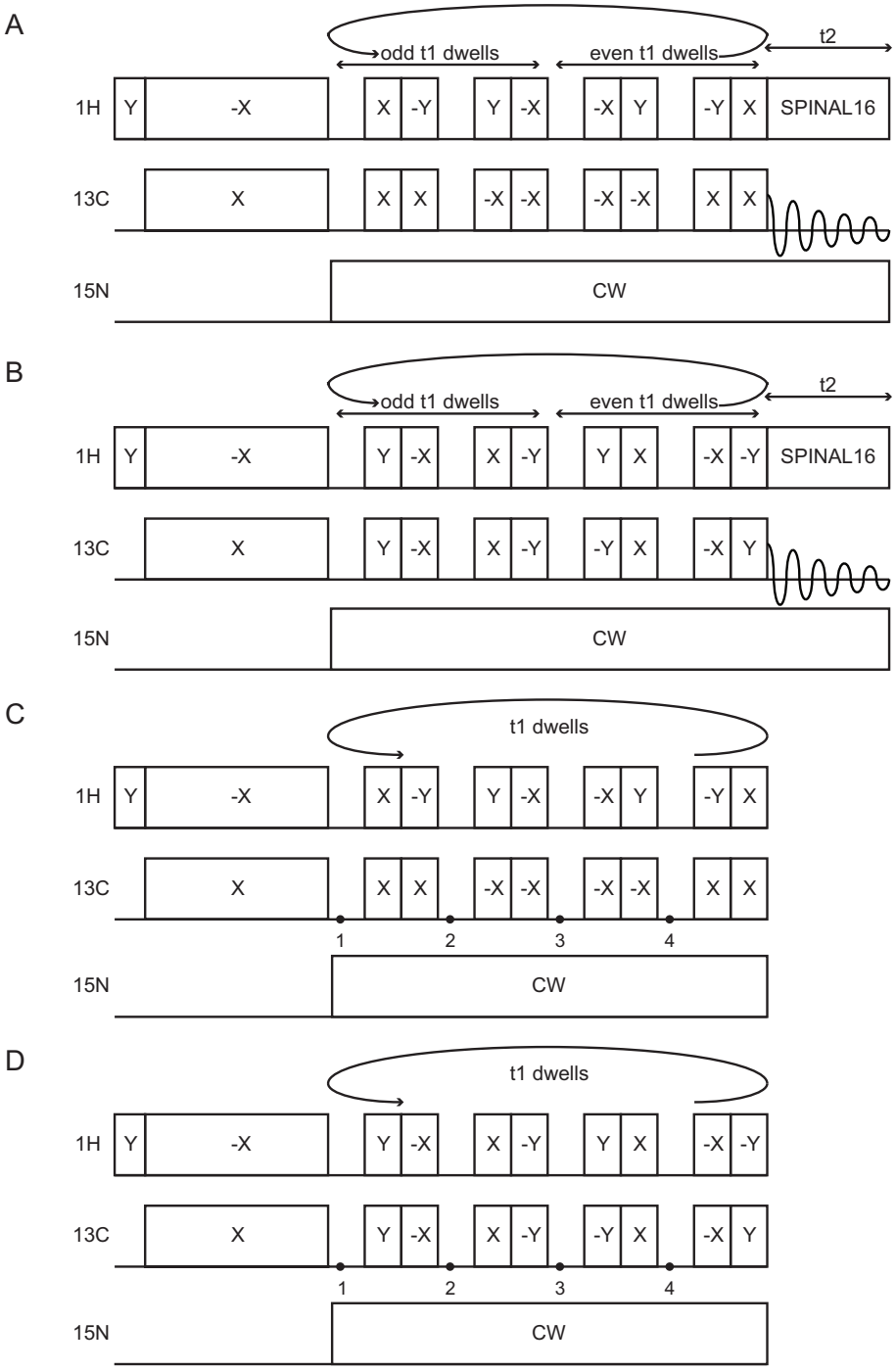

Figure 2.1 Timing diagrams for pulse sequences.
A. $^{1}H/^{13}C$ (with ^{15}N decoupling) PISEMO. B. $^{1}H/^{13}C$ (with ^{15}N decoupling) Dual-PISEMO. C. $^{1}H/^{13}C$ (with ^{15}N decoupling) Window-detected PISEMO. D. $^{1}H/^{13}C$ (with ^{15}N decoupling) Window-detected Dual-PISEMO. CW refers to continuous wave irradiation. SPINAL-16 refers to modulated irradiation [21].

For spin systems with two different types of abundant spins coupled to each other, as in 100% uniformly ^{13}C labeled proteins, where both the ^{1}H and ^{13}C spins are regarded as 'abundant', it is essential to apply multiple-pulse sequences capable of performing homonuclear decoupling on both ^{1}H and ^{13}C channels. This is accomplished in the D-PISEMO pulse sequence diagrammed in Figure 2.1.B where the flip-flop WaHuHa sequence (Y, -X, X, -Y, -Y, X, -X, Y) is applied on the ^{13}C channel and MREV8 (Y, -X, X, -Y, Y, X, -X, -Y) is applied on the ^{1}H channel. Similar results can be obtained by applying the MREV8 cycle to the ^{13}C channel while applying the flip-flop WaHuHa cycle to the ^{1}H channel. Other combinations are also possible. In all the experiments, continuous irradiation at the ^{15}N frequency provides heteronuclear decoupling from both the ^{1}H and ^{13}C spins.

Comparisons among spectra obtained with the pulse sequences diagrammed in Figure 2.1 demonstrate the critical features of D-PISEMO applied to 100% uniformly ^{13}C labeled peptides and proteins. These pulse sequences can be used to detect ^{13}C chemical shifts (Figure 2.1.B) in two-dimensional experiments, or ^{1}H-^{13}C heteronuclear dipole-dipole couplings (Figure 2.1.D) in a one-dimensional version. Conventional single-contact spin-lock cross-polarization was used to obtain the ^{1}H and ^{15}N decoupled one-dimensional ^{13}C NMR spectra in Figure 2.2.A and 2.2.D. The spectrum in Figure 2.2.A consists of four single-line resonances, one from each unique site in the unit cell of a single crystal where there is only one ^{13}C labeled site in each molecule of the model peptide ^{15}N, $^{13}C\alpha$ N-acetyl-leucine (NAL). In contrast, the spectrum shown in Figure 2.2.D, which was obtained from a 100% uniformly ^{13}C labeled single crystal of the model peptide N-acetyl-valine (NAV), is poorly resolved with broad, overlapping resonance

intensity due to the effects of the homonuclear ^{13}C-^{13}C dipole-dipole couplings. By itself, the comparison between the one-dimensional spectra in Figure 2.2.A and 2.2.D demonstrates why it is essential to incorporate homonuclear ^{13}C-^{13}C decoupling into experiments that are to be applied to 100% uniformly ^{13}C labeled stationary samples.

Homonuclear decoupling in solids is generally accomplished with either multiple-pulse sequences, such as WaHuHa [56], or continuous off-resonance (Lee-Goldburg) irradiation [54]. Previously, we demonstrated that resonances with different ^{13}C chemical shifts could be resolved in samples by applying ^{13}C-^{13}C homonuclear decoupling in the indirect dimension of experiments performed with direct ^{15}N detection [77], since only heteronuclear ^{1}H and ^{13}C decoupling is required during data acquisition to obtain high resolution spectra with single-line resonances. However, our goal is to utilize direct ^{13}C detection in order to gain sensitivity and flexibility in experimental design, and this requires the use of homonuclear decoupling during data acquisition in order to obtain high-resolution ^{13}C NMR spectra. Moreover, the same ^{13}C-^{13}C homonuclear couplings that result in poor spectral resolution, as in Figure 2.2.D, interfere with the evolution of ^{1}H-^{13}C heteronuclear dipolar couplings in SLF experiments performed on samples that are 100% uniformly labeled with ^{13}C [89].

PISEMO yields two-dimensional SLF spectra with resolution and sensitivity similar to those obtained using the original PISEMA experiment with the benefit of increased bandwidth, which is a significant advantage for experiments performed at high fields. We have shown that PISEMO can be performed with either direct ^{13}C detection as a two-dimensional experiment, or with indirect ^{1}H detection as a one-dimensional experiment, depending on whether the observation windows in the multiple pulse

sequence are used to detect the magnetization as it is transferred in an oscillatory manner between the ^{1}H and ^{13}C nuclei [53]. The frequency of the oscillations can be used to measure the magnitudes of individual heteronuclear ^{1}H-^{13}C dipolar couplings. The D-PISEMO variant presented here effects both homonuclear ^{1}H-^{1}H and homonuclear ^{13}C-^{13}C decoupling during the heteronuclear ^{1}H-^{13}C spin-exchange period. Passive ^{15}N heteronuclear decoupling is applied through continuous irradiation when necessary in molecules labeled with ^{15}N in addition to ^{13}C. This enables D-PISEMO to be performed with direct ^{13}C detection in either a one- or two-dimensional experiment, considerably increasing its flexibility and potential applications.

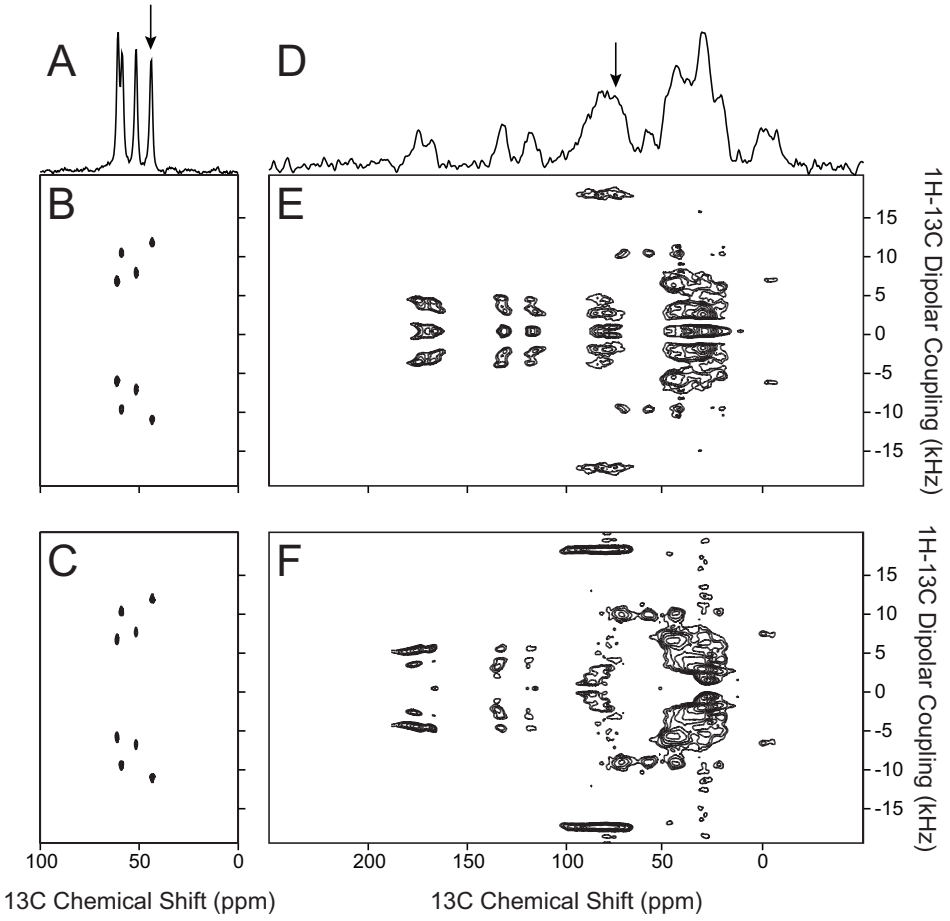

Figure 2.2 ^{13}C-detected PISEMO and D-PISEMO single-crystal spectra.
A. - C. were obtained from a ^{15}N, ^{13}Cα N-acetyl leucine (NAL) single crystal. D. - F. were obtained from a 100% uniformly ^{15}N, ^{13}C labeled N-acetyl valine (NAV) single crystal. A. One-dimensional ^{1}H and ^{15}N decoupled ^{13}C NMR spectrum obtained by cross-polarization. B. and E. Two-dimensional PISEMO spectra. C. and F. Two-dimensional D-PISEMO spectrum. The ^{1}H carrier frequency was set at 4.7 ppm for all spectra; the ^{13}C carrier frequency was set at 50 ppm for A. - C. and at 100 ppm for D. - F. All spectra were acquired with 4scans, 64 t_1 points and 512 t_2 points. The dwell times were 36 μs and 20 μs for t_1 and t_2 dimensions respectively. The cross-polarization time was 1 ms and the recycle delay was 6 s. The experimental data were zero filled to 512 and 1024 data points in t_1 and t_2 dimensions and were multiplied by a sine bell window function prior to Fourier transformation.

The two-dimensional SLF spectra in Figure 2.2.B and 2.2.C are very similar; they serve as controls to demonstrate the similarity of the performance of PISEMO and D-PISEMO for isolated ^{13}C sites unaffected by homonuclear ^{13}C-^{13}C dipole-dipole

interactions. In both spectra, a doublet due to heteronuclear ^{1}H-^{13}C dipole-dipole coupling is associated with each ^{13}C resonance resolved by its chemical shift that is observed in the one-dimensional spectrum. The dipolar coupling spectra in Figure 2.3.A and 2.3.B are associated with the $^{13}C\alpha$ resonance marked with an arrow in Figure 2.2.A. The frequencies of the signals, their line widths, and their intensities are essentially the same whether the spectra were obtained with the original version of PISEMO or D-PISEMO, demonstrating that for spatially isolated ^{13}C sites it is not necessary to apply homonuclear decoupling on the ^{13}C channel. In contrast, the situation is quite different for experiments performed on similar but 100% uniformly ^{13}C labeled samples. There are substantial differences between the spectra obtained with PISEMO (Figure 2.2.E and Figure 2.3.C) and D-PISEMO (Figure 2.2.F and Figure 2.3.D). Although it is somewhat difficult to visualize in the contour plots that include overlapping patterns from carbons bonded to between zero and three hydrogens, the PISEMO spectrum (Figure 2.2.D) is clearly much more complex and has more spectral artifacts, especially for resonances with relatively small dipolar couplings than the D-PISEMO spectrum (Figure 2.2.F). The arrow in Figure 2.2.D marks the frequency for a single $^{13}C\alpha$ resonance, as identified by analysis of individual spectral slices through the ^{1}H-^{13}C heteronuclear dipolar coupling dimension.

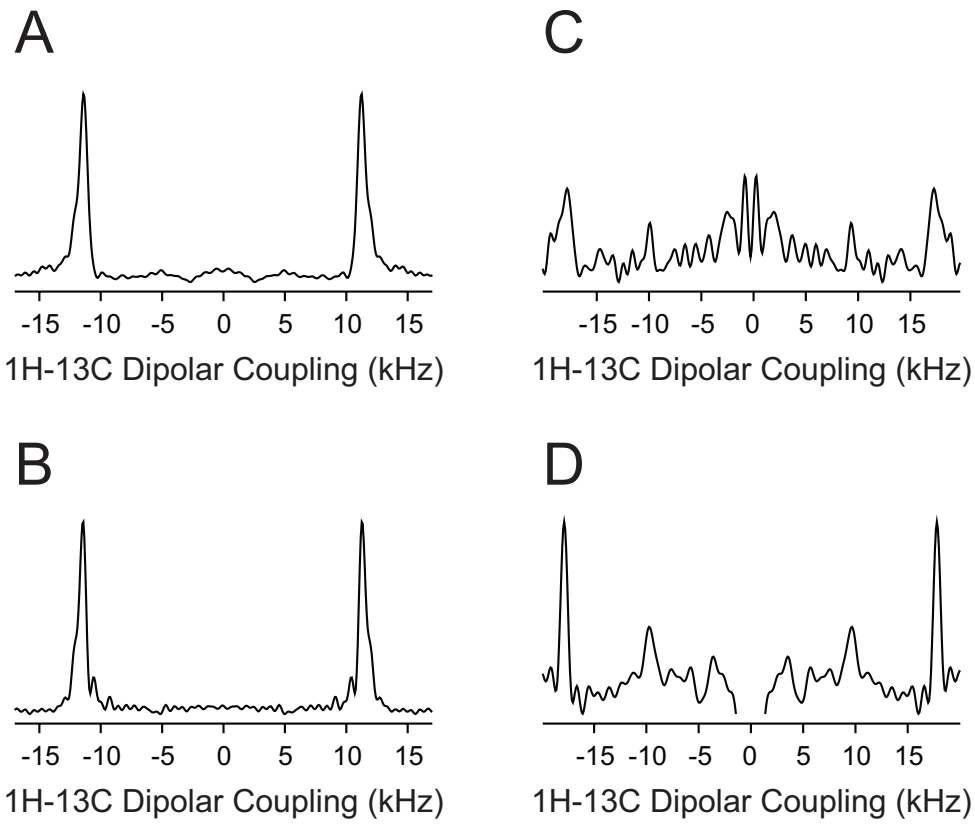

Figure 2.3 One-dimensional slices along the ^{1}H-^{13}C dipolar coupling dimension from PISEMO and D-PISEMO single-crystal spectra.
They correspond to a selected ^{1}H-$^{13}C\alpha$ dipolar coupling. A. and B. are associated with the resolved peak marked with an arrow in Figure 2.2.A., 2.2.C. and 2.2.D. are associated with the partially resolved$^{13}C\alpha$ peak at 75 ppm marked with an arrow in Figure 2.2.D.

The spectral slices associated with the position of the arrow in Figure 2.2.D shown in Figure 2.3.C and 2.3.D are dramatically different. Only with D-PISEMO is it possible to resolve and measure the splitting of the ^{1}H-^{13}C dipolar coupling doublet without distortions due to broadenings, splittings, and spectral artifacts emanating from the presence of ^{13}C-^{13}C dipole-dipole couplings. The sensitivity is dramatically improved as well, demonstrating that D-PISEMO enables the measurement of individual dipolar couplings in 100% uniformly ^{13}C labeled peptides.

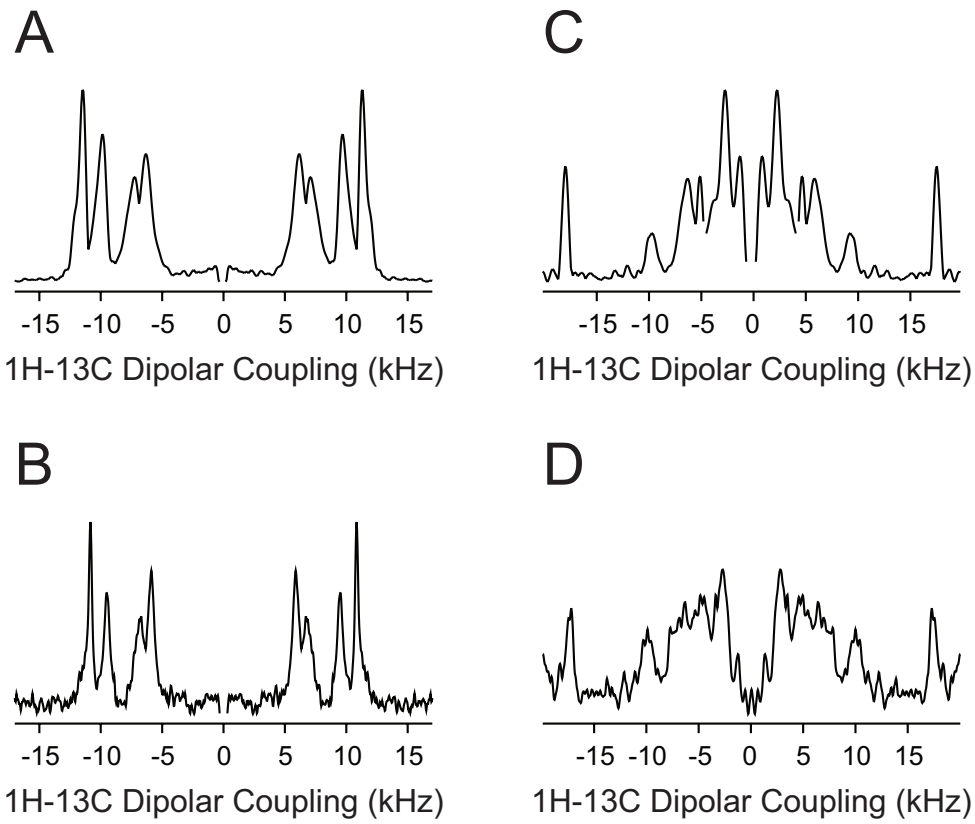

Figure 2.4 One-dimensional ^{1}H-^{13}C dipolar coupling spectra of window-detected PISEMO and the projections of D-PISEMO.
A. and C. are projections of two-dimensional spectra. B. and D. are window-detected one-dimensional spectra. A. and B. were obtained from a ^{15}N, $^{13}C\alpha$ N-acetyl leucine (NAL) single crystal. C. and D. were obtained from a 100% uniformly ^{15}N, ^{13}C labeled N-acetyl valine (NAV) single crystal. uniformly ^{15}N, ^{13}C NAV single crystal.

In the window-detected version of the experiment (W-PISEMO) diagrammed in Figure 2.1.C individual data points are acquired at the designated intervals of each WaHuHa cycle. Plotted as a function of time, these intensities constitute a dipolar free induction decay that can be subsequently Fourier transformed to yield a one-dimensional dipolar frequency spectrum. The evolution of the magnetization generated by the initial cross-polarization reflects only the ^{1}H-^{13}C heteronuclear dipole-dipole coupling, therefore this is a one-dimensional Shiftless NMR spectrum [60]. Since it contains all the dipolar

coupling frequencies, it corresponds to the projection of the two-dimensional spectrum along the dipolar coupling frequency axis. As illustrated in Figure 2.4, the projections of the two-dimensional spectra (Figure 2.4.A and 2.4.C) are similar to the spectra obtained using the window-detected version of the same pulse sequences (Figure 2.4.B and 2.4.D, respectively). Although many sites in the uniformly labeled NAV single crystal contribute to the one-dimensional spectrum obtained with WD-PISEMO, the strong intensity and evidence of many individual splittings demonstrate that the experiment can deal with the network of ^{13}C-^{13}C homonuclear couplings. As Shiftless NMR spectra, the spectral resolution in Figure 2.4.B and 2.4.D result entirely from the $^{13}C\alpha$ sites having different ^{1}H-$^{13}C\alpha$ heteronuclear dipolar coupling frequencies. Neither the ^{1}H nor the ^{13}C chemical shift interactions affect these spectra. Notably, it is feasible to obtain a high-resolution shiftless NMR spectrum even in situations where the sites have identical chemical shifts or the spectral resolution is limited by magnetic field inhomogeneities or instabilities. The feature illustrated here is that the one-dimensional projection derived from a two-dimensional experiment (Figure 2.4.A and 2.4.C) can be replicated (Figure 2.4.B and 2.4.D) in an experiment with reduced dimensionality. The windowed versions of D-PISEMO (Figure 2.1.B) can also be used as building blocks for more complex multidimensional experiments, in particular new classes of Shiftless NMR experiments.

To demonstrate applicability to a 100% uniformly ^{13}C labeled residues in a protein, the NMR spectrum in Figure 2.5.B is a slice taken from a two-dimensional spectrum obtained with D-PISEMO. The sample is fd bacteriophage that is aligned by the magnetic field of the NMR spectrometer. The coat protein contains uniformly ^{13}C leucine residues.

The doublet in Figure 2.5.B is from the ^{1}H-^{13}C dipolar coupling associated with the leucine residue whose $^{13}C\alpha$ resonance is marked by the arrow in Figure 2.5.A.

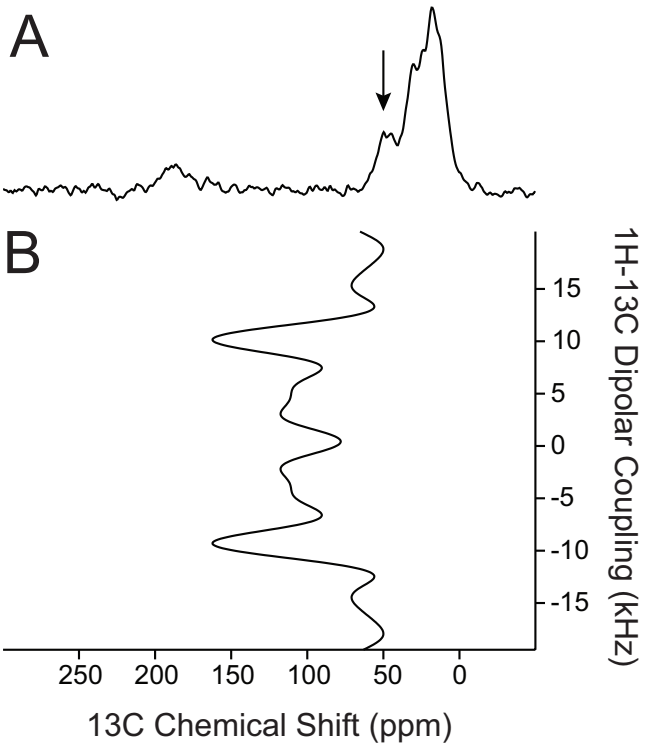

Figure 2.5 D-PISEMO spectrum of uniformly ^{13}C, ^{15}N leucine labeled fd bacteriophage. A. One-dimensional 13C chemical shift spectrum. B. One-dimensional ^{1}H-$^{13}C\alpha$ dipolar coupling slice taken from a two-dimensional D-PISEMO spectrum. The spectra were obtained from the coat protein labeled 100% uniformly at its two leucine residues in fd bacteriophage magnetically aligned at 65 °C. The slice of the peak marked by the arrow (50 ppm) corresonds to a $^{13}C\alpha$ resonance. The two-dimensional NMR spectrum was acquired with 128 scans, 12 t_1 points, and 512 t_2 points. The dwell time was 36 μs and 20 μs for t_1 and t_2 dimensions, respectively. The cross-polarization time was 1 ms and the recycle delay was 6 s. The experimental data were zero filled to 512 and 1024 data points in t_1 and t_2 dimensions and were multiplied by a sine bell window function prior to Fourier transformation.

2.4 Discussion

Separated local field spectroscopy is a particularly powerful experiment because it provides direct measurements of heteronuclear dipolar couplings associated with individual atomic sites in molecules as complex as proteins. When the ^{1}H and dilute spin, either ^{13}C or ^{15}N, are directly bonded, which fixes their internuclear distance, then the frequency of the dipolar coupling provides a strong orientational constraint for structure calculations. The chemical shift of each resonance provides a complementary orientational constraint. In this type of spectroscopy, the resolution also results from difference in orientations rather than chemical environments.

In order to extend the method beyond the ^{15}N amide backbone sites of proteins it is essential to utilize ^{13}C labeling and $^{1}H/^{13}C/^{15}N$ triple-resonance experiments. Although now in routine use in solution NMR and MAS solid-state NMR, these experiments require substantial development for applications to proteins in OS solid-state NMR. The combination of many ^{13}C-^{13}C dipole-dipole couplings in tight networks, the wide frequency range for isotropic chemical shift, and the wide frequency ranges for carbonyl and aromatic carbon chemical shift anisotropy make these challenging experiments.

In this article, we demonstrate the feasibility of simultaneously applying homonuclear dipolar coupling to the ^{1}H and ^{13}C nuclei to reveal individual dipolar couplings associated with single resonances. The use of D-PISEMO provides substantial improvements in both resolution and sensitivity by performing homonuclear ^{13}C-^{13}C decoupling. It can be performed as a conventional two-dimensional experiment, or with windowed detection as a one-dimensional experiment that offers flexibility for Shiftless and other multidimensional triple-resonance experiments on peptides and proteins.

2.5 Methods

2.5.1 NMR spectroscopy

The NMR experiments were performed on a Varian Inova spectrometer with ^{1}H, ^{13}C, and ^{15}N frequencies of 500.125 MHz, 125.76 MHz, and 50.68 MHz, respectively. In all experiments, the measured B_1 field was 50 kHz for the ^{1}H and ^{13}C channels, and 30 kHz for the ^{15}N channel. The ^{1}H chemical shift frequencies were referenced to the water as 4.7 ppm (25^{o}C). The ^{13}C chemical shift frequencies were referenced to the $^{13}CH_2$ resonance of adamantane as 38.47 ppm and the ^{15}N chemical shift frequencies were referenced to a ^{15}N labeled ammonium sulfate as 26.8 ppm, all as external references.

The windows between the multiple pulses can be utilized for signal acquisitions, and it is possible to acquire multiple sample points within each window. However, in these early experiments the observed signal-to-noise ratios are limited by practical aspects of optimizing analog and digital filters for windowed detection in multiple-pulse sequences. The numbers shown in Figure 2.1.C and 2.1.D represent the timing of the data acquisitions in the windows, and the delay between the last pulse and acquisition is 2.6 μs which is limited by probe ringing. Two free induction decays (FIDs) were acquired in each window-detected experiment. The sample points acquired in the first and the third windows are taken as the data points in the first FID, and these points correspond to the odd and even t_1 dwells in PISEMO or D-PISEMO experiments. Similarly, the second FID is constituted from the sample points obtained in the second and the fourth windows. Because of the change in effective B1 field, the two FIDs are added together after applying a 45° phase correction to the second FID. This results in an increase in the

signal-to-noise ratio of approximately 20%. The scaling factors of W-PISEMO and WD-PISEMO are the same to those observed for PISEMO and D-PISEMO (0.67).

2.5.2 Triple-resonance NMR probe

A home-built triple resonance probe was constructed specifically for these experiments using design principles consistent with applications to lossy biological samples [90]. It has an outer coil that is a modified Alderman Grant coil (MAGC), which operates at the proton (^{1}H) tuning frequency, and an inner solenoid coil that generates an orthogonal B_1 field. A similar double-resonance probe utilizing MAGC and solenoid coils has been previously described [91], and the probe described here is an extension of this design with the incorporation of a third channel. In this triple resonance version of the probe, the inner 5 mm ID solenoid coil is double-tuned to the ^{15}N and ^{13}C frequencies. The resulting cross-coil probe pictured in Figure 2.6 offers several advantages over a more traditional modified Cross-Waugh circuit [92], in which a single solenoid sample coil is triply tuned, as used in our previous studies [93] and designs from other laboratories [94; 95]. The main advantage of the MAGC is the dramatically reduced radio frequency (RF) heating that results from the low inductance of the MAGC. The low voltage drop across the leads of the coil significantly decreases the scalar electric field across the sample volume, which is the principal mechanism of sample heating during high frequency RF irradiation. Furthermore, the low inductance and relatively low filling factor ensure that the MAGC ^{1}H tuning frequency and resonance Q factor are not significantly altered by the introduction of high dielectric, lossy biological samples that are extensively hydrated, such as the bacteriophage particles in aqueous solution in

Figure 2.5. The separation of the ^{1}H tuning circuit and coil assembly from the low frequency coil and circuit enables the choice of a solenoid inner sample coil of optimal inductance and filling factor for the ^{13}C and ^{15}N frequencies. A seven turn solenoid coil provides optimal inductance of the inner coil, and along with the simplified double resonance inner coil tuning circuit, we were able to obtain a significant increase in sensitivity compared to similarly constructed Cross-Waugh style single solenoid coil probes, which typically utilized a five or six turn 5 mm ID coil to ensure adequate ^{1}H performance in a triple tuned configuration. The ^{15}N and ^{13}C channels of the probe are isolated using a pair of band stop filters containing a significant amount of inductance (L4 and L6 in Figure 2.6). This provides a durable double tuned inner coil circuit that can withstand high power irradiation on one of the low frequency channels while observing the other. The probe performance is summarized in Table 2.1. The disadvantage of this design is that the low inductance and reduced filling factor of the outer MAGC make it rather insensitive for direct proton observation. This is not an issue in the class of experiments described in this article, since they are focused on direct ^{13}C detection.

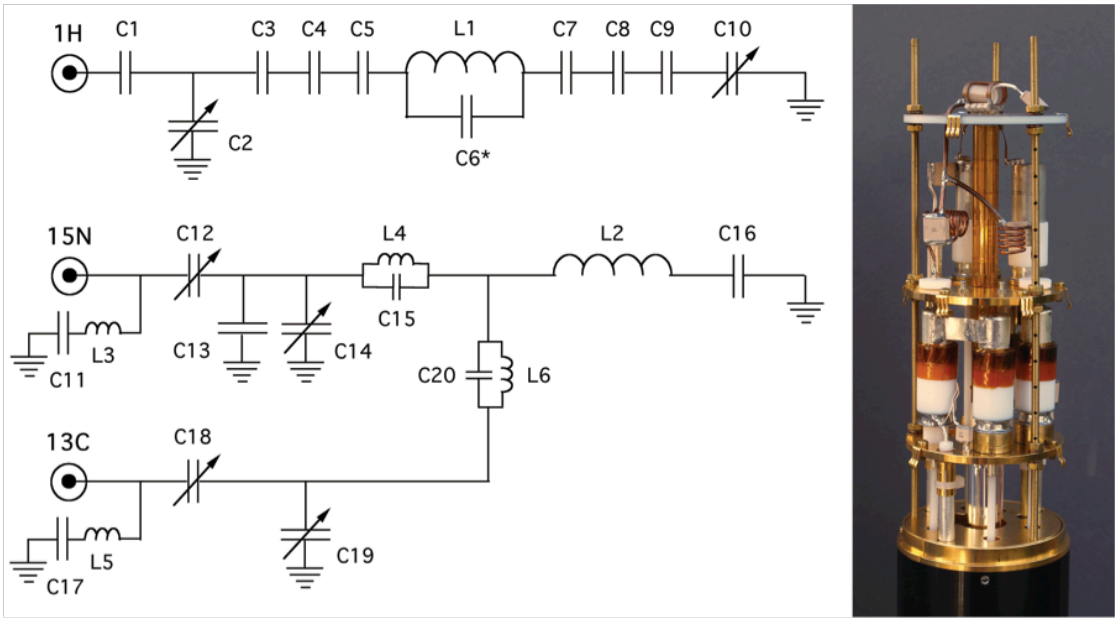

Figure 2.6 Photograph and circuit diagram of triple-resonance MAGC probe.
Right: Photograph of the triple-resonance probe used in these experiments. Left: Circuit diagram for the triple-resonance MAGC probe pictured. L1 represents the outer 9 mm ID Modified Alderman-Grant Coil and L2 is the seven turns 5mm ID inner solenoid coil. The values of the capacitors are: C1 = 2.7 pF, C3 = 6.8 pF, C4 = 6.8 pF, C5 = 6.8 pF, C7 = 12 pF, C8 = 12 pF, C9 = 12 pF, C11 = 6.8 pF, C13 = 33 pF, C15 = 12 pF, C16 = 56 pF, C17 = 6.8 pF, C20 = 56 pF. The capacitance C6* is 8.19 pF total integrated into the MAGC and consists of three parallel strings of four series ceramic chip capacitors. Capacitors C2, C10, C12, C14, C18 and C19 are variable capacitors with a range of 1-10 pF. Inductors L4 and L6 are 8 turn and 5 turn 8 mm coils respectively.

Table 2.1 Summary of probe performance.

Channel	Nutation frequency,RF Power	RF Homogeneity (A810/A90)X100%
^{1}H	71 kHz, 109W	73%
^{13}C	55 kHz, 99W	70%
^{15}N	55 kHz, 280W	70%

2.5.3 Samples

The preparation of uniformly ^{13}C leucine labeled fd bacteriophage for high resolution NMR spectroscopy followed previous methods [27]. The samples for the solid-

state NMR experiments were 5-mm o.d. thin-wall glass tubes containing 180 μl of 50 mg/ml solutions of bacteriophage in 5 mM sodium borate buffer, pH 8.0. Under these conditions, the bacteriophage particles align with their long axis parallel to the direction of the applied magnetic field. All of the isotopically labeled compounds and media described in this article are from Cambridge Isotope Laboratories (www.isotope.com).

Chapter 2, in full, is a reprint of the material "^{1}H-^{13}C separated local field spectroscopy of uniformly ^{13}C labeled peptides and proteins" as it appears in J. Magn. Reson. 206(1):105-111 by Lin EC, Wu CH, Yang Y, Grant CV, and Opella, SJ. The thesis author was the primary author of the paper.

Chapter 3 ^{1}H Assisted ^{13}C/^{15}N Heteronucealer Correlation Spectroscopy in Oriented Sample Solid-State NMR of Single Crystal and Magnetically Aligned Samples

3.1 Abstract

^{1}H-irradiation under mismatched Hartmann-Hahn conditions improves the efficiency of selective ^{15}N/^{13}C transfers in triple-resonance heteronuclear correlation spectroscopy (HETCOR) on stationary samples of single crystals and aligned samples of biopolymers. Sensitivity is improved by taking advantage of the $^{13}C_{\alpha}$ and ^{15}N labeled peptides and proteins with ^{13}C detection. The similarities between experimental and simulated spectra demonstrate the validity of the recoupling mechanism and identify opportunities for applying these methods to membrane proteins in phospholipid bilayers.

3.2 Introduction

Solid-state NMR spectroscopy is playing an increasingly important role in the determination of the structures of proteins in biological supramolecular assemblies, such as membrane proteins in phospholipid bilayers[96-99], coat proteins of virus particles[100], aggregates of amyloid proteins[101], etc. Oriented Sample (OS) solid-state NMR is particularly well suited to molecular assemblies that can be mechanically or magnetically[102] aligned in the field. This allows angular constraints to be derived from the measured frequencies relative to a single external axis, which fully defines the alignment tensor, unlike the situation for residual dipolar couplings (RDCs) in solution

NMR where determination of the alignment tensor can be a major source of error [103]. Significantly, since each measurement is independent of the others on the molecule, any experimental errors in the measurements of frequencies or uncertainties in the magnitudes or molecular orientations of the spin-interaction tensors do not accumulate. This results in high-resolution and accurate structure determinations.

OS solid-state NMR has been successfully applied to DNA, membrane proteins, and viral coat proteins, primarily through the use of uniform and selective ^{15}N labeling. ^{15}N labeling of biopolymers has many advantages[104]. Uniform ^{15}N labeling is easy and inexpensive to implement by expressing the protein or nucleic acid of interest in bacteria grown on chemically defined media where there is only a single source of nitrogen, typically a salt of ammonia. Since no nitrogens are directly bonded in biopolymers, and in the critical polypeptide backbone of proteins each amide nitrogen is separated from another by two carbon atoms and three bonds, homonuclear $^{15}N/^{15}N$ decoupling is not necessary at any stage of the experiments because of the combination of the low gyromagnetic ratio and spatial separation of nitrogen atoms. Many double-resonance $^{1}H/^{15}N$ experiments have been developed to measure frequencies from the three spin-interactions available at a single ^{15}N labeled site: ^{1}H chemical shift, ^{15}N chemical shift, and $^{1}H/^{15}N$ heteronuclear dipolar couplings[50; 105-107]. A number of assignment schemes have been developed based on both through-space interactions and the regularity of structural and spectral features that accompany the mapping of the structure onto the spectra by the anisotropic spin-interactions in the secondary structures of the α-helix and β-sheet[108; 109]. Recently, through-space methods of identifying proximate nuclei have been improved by invoking assistance from a third spin[110] .

In order to further advance OS solid-state NMR methods, triple-resonance experiments on ^{13}C and ^{15}N double labeled samples are an essential next step. This would enable spectroscopic interrogation of essentially all sites in a biopolymer. Since all backbone sites of a protein would be labeled it offers the possibility of systematic assignment schemes, and with ^{13}C detection higher sensitivity. However, in fully labeled biomolecules there is a significant problem. The ^{13}C form a dense network of homonuclear dipole-dipole coupled nuclei that interfere with most multi-dimensional solid-state NMR experiments as well as ^{13}C detection. We have taken two approaches to ameliorating these difficulties. One is to use 'tailored' ^{13}C labeling through judicious choice of ^{13}C-containing precursors in the growth media[111]. This enables either uniform dilution of the ^{13}C nuclei or high levels of labeling at selected sites where nearby carbons are unlabeled. The strong homonuclear dipole-dipole couplings are attenuated by the effect of the dilution on their spatial proximity. The second approach is to develop NMR experiments that incorporate homonuclear decoupling on both the ^{1}H and ^{13}C channels[112]. The implementation of triple-resonance experiments provides ^{13}C chemical shift, and ^{1}H-^{13}C angular constraints that complement those from ^{15}N especially since some of them are out of the peptide plane, and as a result add unique information to the structure calculations. Moreover, ^{13}C detection offers increased sensitivity compared to the corresponding ^{15}N detection.

Cross-polarization (CP) between abundant spins and dilute spins has been demonstrated successfully both in magic angle spinning (MAS) and stationary solid-state NMR experiments. The magnetization can be transferred from ^{1}H to either ^{15}N or ^{13}C easily because of the strong dipolar couplings, up to 11 kHz or 22 kHz in peptides,

respectively. In the basic cross-polarization experiment introduced by Waugh and coworkers[113], the observed signals are enhanced by up to ten- or four-fold for ^{15}N and ^{13}C, respectively[114]. Here we are interested in using these large initial increases in magnetization to enable subsequent transfers to provide additional frequency dimensions for resolution, and to initiate the development of systematic assignment methods for OS solid-state NMR.

The first goal of the pulse sequence is to transfer magnetization from the initially polarized dilute spin to the second type of dilute spin. In general, this is referred to as double-cross-polarization (DCP)[115], although the details of the spectroscopy can vary significantly among the pulse sequences used to carry out this procedure. In the simplest example, the magnetization can be transferred from ^{1}H to ^{15}N, and then from ^{15}N to ^{13}C; alternatively, the magnetization can be transferred from ^{1}H to ^{13}C, and then from ^{13}C to ^{15}N. In general, the efficiency of the magnetization transfer between dilute spins (^{15}N and ^{13}C) is low due to the relatively small dipolar couplings between these two nuclei, which are generally less than 1 kHz because of their relatively low gyromagnetic ratios.

Here we demonstrate that it is possible to obtain two-dimensional $^{13}C/^{15}N$ HETCOR spectra for all directly bonded pairs of ^{15}N and $^{13}C_{\alpha}$ in the backbone of a peptide or protein. Ideally, we would like all of the correlation resonances to have equal intensity, however, for now we have to settle for reliable detection of the correlation resonances for all pairs of ^{15}N and $^{13}C_{\alpha}$ in the peptides or proteins. Since the input for the structure calculations is in the form of the orientationally-dependent frequencies, not intensities or line shapes, this is much less of a handicap than in other classes of

experiments, such as spin-exchange where the intensities of the off-diagonal peaks are important.

Longer mixing times generally improve the extent of magnetization transfer, especially when the dipolar couplings are small. However, the longer mixing times can also result in non-selective magnetization transfer or spin diffusion, depending on the various laboratory and rotating relaxation times. For solid-state NMR of stationary samples, selective magnetization transfers between ^{1}H and ^{15}N or ^{1}H and ^{13}C are feasible when the homonuclear $^{1}H/^{1}H$ dipole-dipole couplings are strongly attenuated, allowing individual heteronuclear dipolar couplings to dominant during specified time intervals of multi-dimensional experiments. Polarization inversion spin exchange at the magic angle (PISEMA)[50], SAMMY,[105] and related pulse sequences are able to decouple the homonuclear ^{1}H dipolar networks and selectively transfer the magnetization between ^{1}H and ^{15}N[116; 117]. Alternatively, dipolar-based INEPT[118], also is effective for transferring magnetization when the ^{1}H network of homonuclear couplings is suppressed. However, during many trials, we were unable to obtain efficient magnetization transfer between ^{15}N and ^{13}C using this family of pulse sequences. In contrast, spin-lock on both ^{15}N and ^{13}C with matched continuous wave irradiation does transfer magnetization between coupled ^{15}N and ^{13}C sites.

Third-spin assisted polarization transfer (TSAR) has been proposed as a method to recouple dilute spins under MAS condition[119]. However, instead of spinning the sample, the offsets can be created under the mismatched Hartmann-Hahn conditions between the abundant and dilute spins[110] that effect recoupling in stationary solid-state NMR experiments, as shown in the following equations:

$$H_{\pm} = -\frac{1}{8\Delta\omega_I}\sum_{n=1}^{N} a_{1n}a_{2n}I_z^{(n)}(S_+^{(1)}S_-^{(2)} + S_-^{(1)}S_+^{(2)})$$ Equation 3.1

$$H_{II} = \frac{1}{8\Delta\omega_I}\sum_{i<j}^{N}(a_{1i}a_{1j}S_z^{(1)} + a_{2i}a_{2j}S_z^{(2)})(I_+^{(i)}I_-^{(j)} + I_-^{(i)}I_+^{(j)})$$ Equation 3.2

$$H_{\Delta} = \frac{1}{16\Delta\omega_I}\sum_{n=1}^{N} a_{1n}^2(S_z^{(1)} - I_z^{(n)}) + a_{2n}^2(S_z^{(2)} - I_z^{(n)})$$ Equation 3.3

$\Delta\omega_I$ is the mismatched Hartmann-Hahn condition that makes the Hamiltonians significant when the mismatch is small. The first term, the recoupling term, recouples two dilute spins by the ^{1}H, and therefore, the ^{1}H dipolar network is used to create couplings among dilute spins. It is this alternative pathway that provides an opportunity to transfer magnetization when the dipolar couplings between dilute spins are weak. The second term, the equilibrating bath term, enable the equilibration of the spin temperature among the spins. For spin diffusion driven by this mechanism[110], ^{15}N is polarized to achieve higher spin temperatures, and then, a z-filter is applied to eliminate any residual ^{1}H magnetization that could result in non-selective transfer. Hence, the spin temperature is always higher for the ^{15}N spins, and that drives the magnetization to redistribute to the proton bath and results in decreasing the transfer efficiencies. The third term can be neglected when the lattice sum of each dilute spin is equal; otherwise, the magnetization will be brought to the orthogonal frame according to the commutator. This term could decrease the transfer efficiency in the heteronuclear correlation experiments, because it is difficult to make the lattice sums of ^{13}C and ^{15}N equal to each other. Spin diffusion experiments among ^{15}N in OS solid-state NMR with ^{1}H-irradiation under mismatched Hartmann-Hahn conditions show that even if several different spin dynamics are

involved, the recouping term still can assist the magnetization transfers. The Hamiltonians also suggest the feasibility of heteronuclear correlations in triple-resonance experiments on stationary samples. Here we demonstrate ^{13}C-detected HETCOR experiments where the ^{15}N/^{13}C transfer is assisted by ^{1}H-irradiation under mismatched Hartmann-Hahn conditions. In addition, we show that the enhancement of signal intensities and the selectivity depend upon experimental conditions.

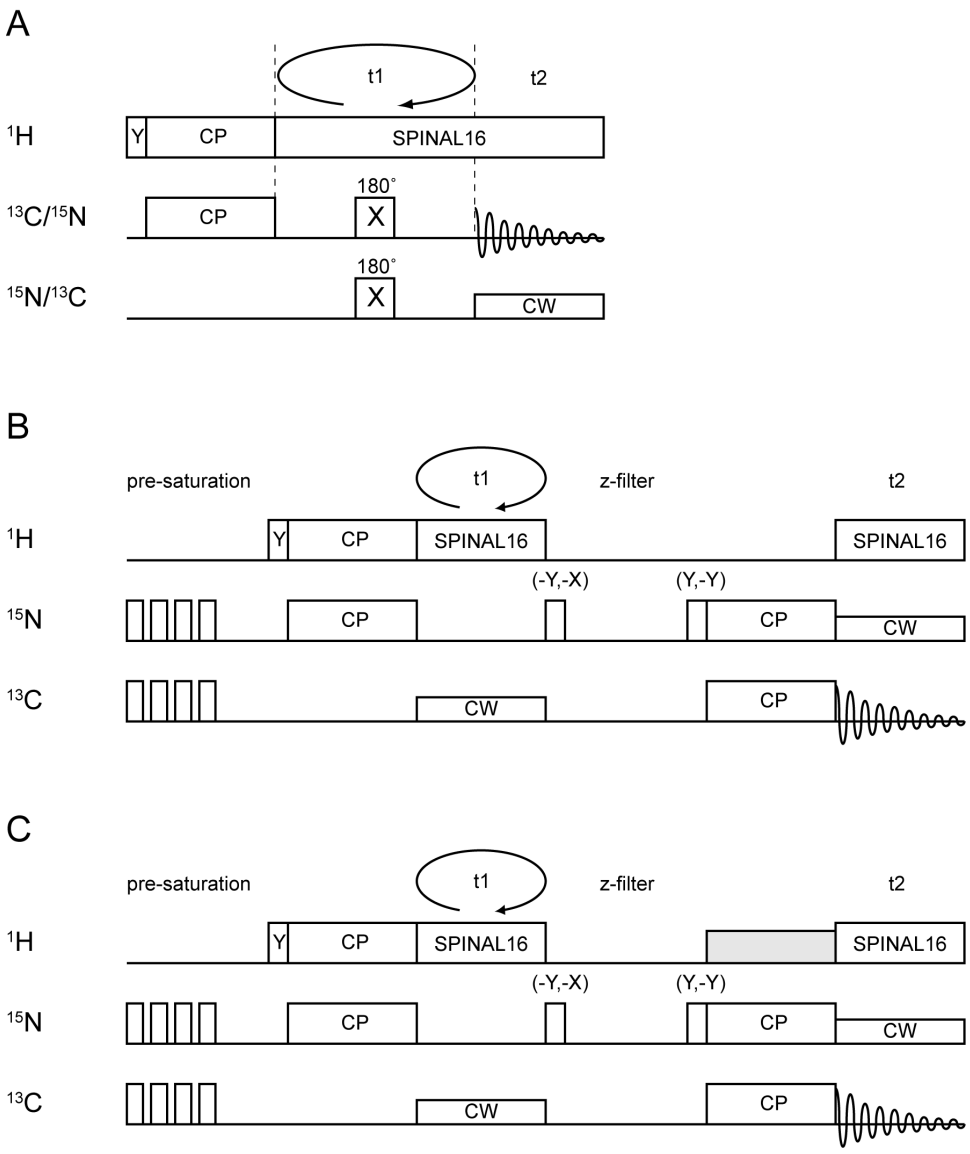

Figure 3.1 Timing diagrams for the pulse sequences.
A. ^{15}N-^{13}C dipolar coupling / ^{13}C chemical shift or ^{15}N-^{13}C dipolar coupling / ^{15}N chemical shift separated-local-field (SLF) experiment. B. ^{15}N/^{13}C HETCOR experiment. C. ^{15}N/^{13}C HETCOR experiment with ^{1}H-irradiation. SLF experiments provide the local fields (dipolar couplings) affecting on the observed spins in the t1 dimension, and the pulse scheme in the t1 dimension can be modified for different demands (^{1}H-^{15}N, ^{1}H-^{13}C, or ^{15}N-^{13}C dipolar couplings). Therefore, the chemical shifts acquired in the t2 dimension can be resolved by these two-dimensional experiments[76; 89]. CW refers to continuous wave irradiation and SPINAL-16[120] refers to the modulation used for heteronuclear decoupling. Pre-saturation is accomplished with thirty 90° pulses separated by 200 μs delay. The z-filter is 5 ms. Mix time for ^{1}H/^{15}N cross-polarization is 1ms, and for ^{15}N/^{13}C cross-polarization is 1ms or 3ms.

3.3 Results and Discussion

Improvement in $^{13}C/^{15}N$ heteronuclear correlation spectra results from ^{1}H-irradiation under mismatched Hartmann-Hahn conditions. This is demonstrated with two samples, and all experiments are performed under stationary conditions. One sample is a single crystal of ^{15}N, $^{13}C_{\alpha}$ N-acetyl-leucine (NAL), which as four unique molecules in its unit cell. The other sample is selectively ^{15}N, $^{13}C_{\alpha}$ alanine-labeled Pf1 bacteriophage coat protein in magnetically aligned virus particles. There are 8 alanine residues in the protein sequence.

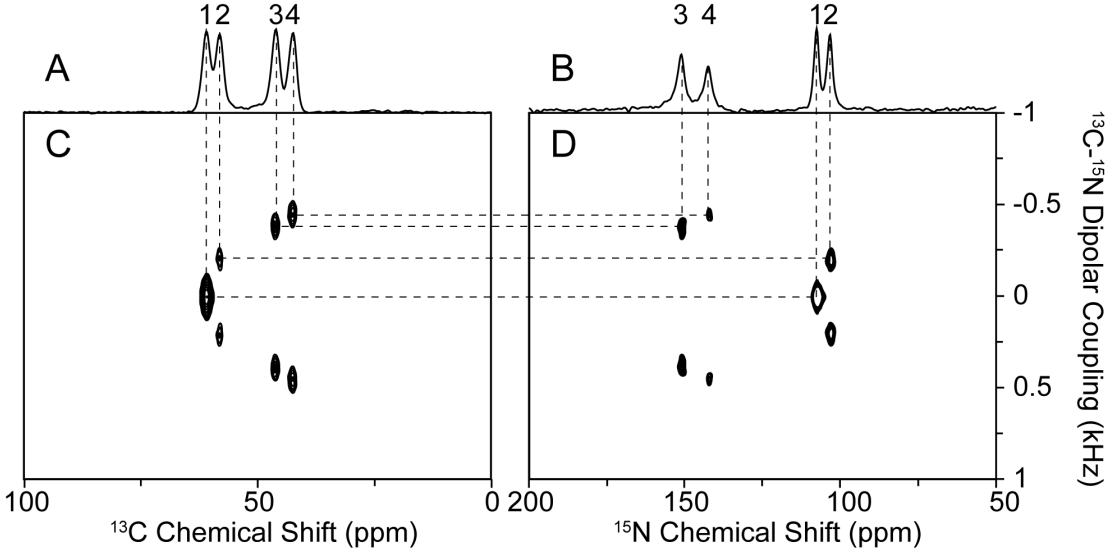

Figure 3.2 ^{15}N-^{13}C SLF spectra of a ^{15}N, $^{13}C_{\alpha}$ NAL single crystal.
A. ^{15}N decoupled ^{13}C NMR spectrum. B. ^{13}C decoupled ^{15}N NMR spectrum. C. ^{13}C-detected ^{15}N-^{13}C heteronuclear dipolar coupling SLF spectra. D. ^{15}N-detected ^{15}N-^{13}C heteronuclear dipolar coupling SLF spectra. The observed ^{15}N-$^{13}C_{\alpha}$ heteronuclear dipolar couplings are: ~0 Hz (pair 1); 200 Hz (pair 2); 374 Hz (pair 3); and 451 Hz (pair 4).

One-dimensional ^{13}C and ^{15}N NMR spectra obtained by conventional spin-lock cross-polarization are shown in Figure 3.2.A and 3.2.B; the four resolved resonances in each spectrum correspond to the four molecular orientations in the unit cell of the single

crystal. The ^{15}N-^{13}C heteronuclear dipolar coupling doublets generated in the t1 dimension by the separated-local-field (SLF) experiment using the pulse sequence diagramed in Figure 3.1.A are shown in Figure 3.2.C and 3.2.D. Both the chemical shift and heteronuclear dipolar coupling frequencies depend on the angles between ^{15}N-$^{13}C_{\alpha}$ bonds and the magnetic field. As a result, the ^{15}N and $^{13}C_{\alpha}$ sites in a single peptide plane have the same ^{15}N-^{13}C dipolar coupling. By matching the ^{15}N-^{13}C dipolar couplings in the ^{15}N- and ^{13}C-detected ^{15}N-^{13}C dipolar coupling SLF spectra, all four resonances in the ^{15}N and ^{13}C one-dimensional spectra can be correlated. The ^{15}N and $^{13}C_{\alpha}$ pairs are identified in Figure 3.2. The ^{15}N-$^{13}C_{\alpha}$ dipolar couplings are 200 Hz, 374 Hz, and 451 Hz for pair 2, pair 3 and pair 4, respectively. These doublets show the ^{15}N-^{13}C dipolar couplings are small, as predicted for the peptide system. The ^{15}N-$^{13}C_{\alpha}$ dipolar coupling of pair 1 is below the resolution limit of this particular experiment, and therefore we classify the heteronuclear dipolar coupling of this pair to be ~ 0 kHz.

The conventional $^{15}N/^{13}C$ HETCOR experiments were performed using the pulse sequence in Fig. 1B. ^{15}N and ^{13}C are pre-saturated to ensure that the magnetization is transferred from other spins without interference from residual magnetization. The magnetization is first transferred from ^{1}H to ^{15}N, and the ^{15}N nucei then evolve according to their chemical shift interactions by removing heteronuclear dipolar couplings. Subsequently, a 5ms z-filter is applied to remove any residual ^{1}H magnetization. The first 90° pulse brings the ^{15}N magnetization to the z-axis, and is alternated between –Y and –X phase to achieve quadrature detection in the t1 dimension; the second 90° pulse brings the magnetization back, and is alternated between Y and –Y phase to suppress the effects of probe ringing. The magnetization is subsequently transferred with the continuous wave

irradiation applied on the ^{15}N and ^{13}C channels simultaneously, and ^{13}C chemical shifts are detected in the t2 dimension.

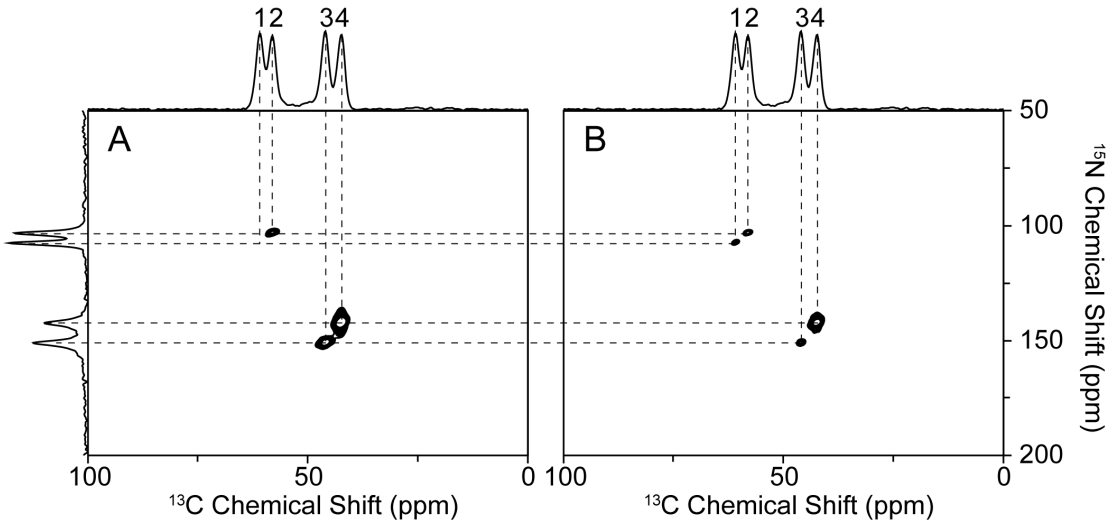

Figure 3.3 Traditional and ^{1}H mismatched irradiation (lower mismatch condition) HETCOR spectra.
A. ^{13}C-detected $^{15}N/^{13}C$ HETCOR spectrum of a ^{15}N, $^{13}C_{\alpha}$ NAL single crystal. B. ^{13}C-detected $^{15}N/^{13}C$ HETCOR with ^{1}H-irradiation at 40 kHz. The one-dimensional spectra aligned on the top and side are the same ^{13}C and ^{15}N CP spectra shown in Figure 3.2.A and B, respectively. Note in Figure 3.3.B that the signal from pair 1 is detectable only in the presence of ^{1}H-irradiation. The experiments were performed with 1ms (shown) and 3ms $^{15}N/^{13}C$ mixing time with similar results.

Three resonances shown in Fig. 3.3.A were obtained in the regular $^{15}N/^{13}C$ HETCOR experiment with 1ms $^{15}N/^{13}C$ mixing time. The missing resonance corresponds to resonance 1, which has ~ 0 kHz ^{15}N-^{13}C dipolar coupling. Notably, no magnetization transfer is observed for pair 1 even with the mixing time extended to 3 ms.

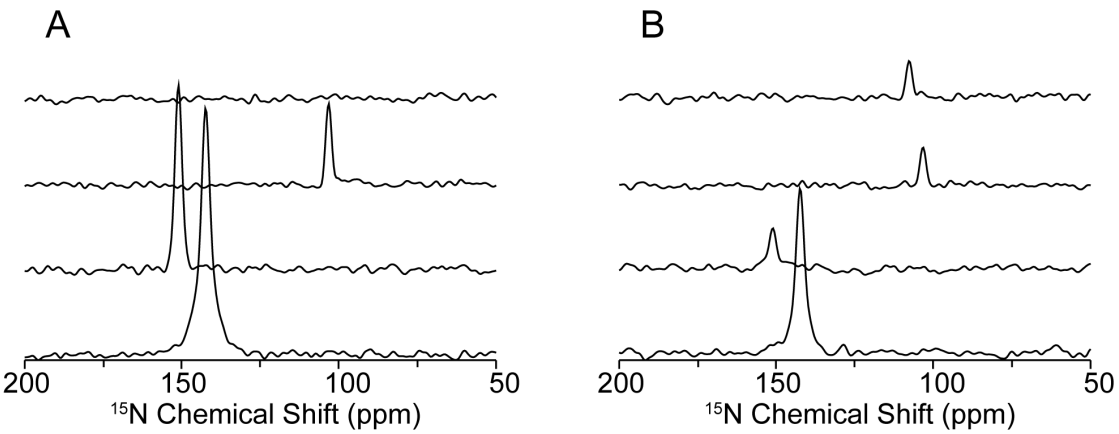

Figure 3.4 One-dimensional spectral slices along the ^{15}N chemical shift dimension from the two-dimensional spectra shown in traditional and ^{1}H mismatched irradiation (lower mismatch condition) HETCOR spectra.
A. ^{15}N/^{13}C HETCOR. B. ^{15}N/^{13}C HETCOR with ^{1}H-irradiation at 40 kHz. From top to bottom, the slices correspond to pairs 1 to 4, respectively. In Figure 3.4.A, the measured signal-to-noise ratios are 36 (pair 2), 83 (pair 3) and 111 (pairs 4). In Figure 3.4.B, the measured signal-to-noise ratios are 17 (pair 1), 18 (pair 2), 18 (pair 3) and 74 (pair 4). Reductions in some signal intensities result from competing pathways. The narrow single-line peaks and the flat baselines demonstrate that the transfer from ^{15}N to ^{13}C is selective.

Four resonances are present in Figure 3.3.B with ^{1}H-irradiation at 40 kHz during the ^{15}N/^{13}C mixing period (Figure 3.1.B). Slices through all the resonances in the t1 dimension are shown in Fig. 4. The experimental results on the single crystal are fully consistent with the described model: ^{1}H-irradiation provides another pathway to transfer the magnetization from ^{15}N to $^{13}C_{\alpha}$ via the proton bath. The weaker intensities of the pair 2 to pair 4 imply that the other two terms (Equation 3.2 and 3.3) are involved as well and result in loss of signal intensity. The benefit of ^{1}H-irradiation is shown on pair 1. Although, there are other processes competing with recoupling, the experimental results show that recoupling can drive the magnetization transfer without direct dipolar couplings. Non-selective transfer from the proton bath when ^{1}H-irradiation is applied can

be ruled out by inspecting the slices in Figure 3.4, since the sharp peaks and flat baselines show only that a specific frequency is transferred.

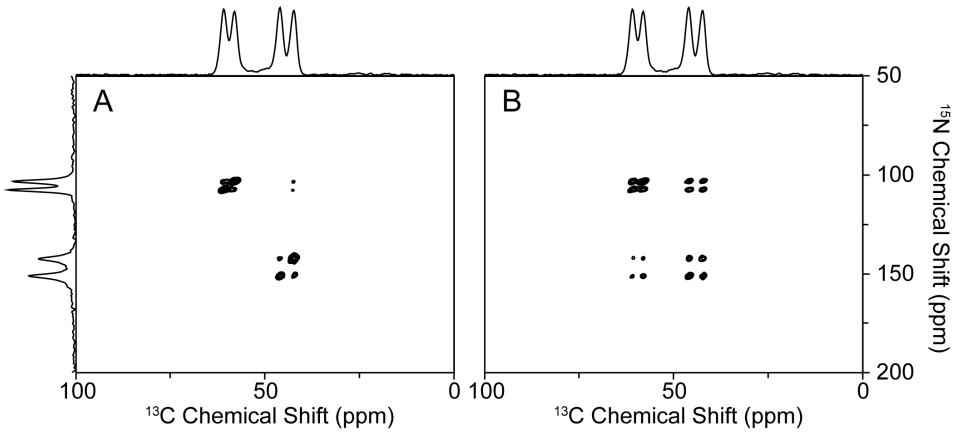

Figure 3.5 HETCOR spectra at higher mismatched condition with different mixing time. A. and B. ^{15}N/^{13}C HETCOR spectra obtained with ^{1}H-irradiation of 60 kHz with 1ms and 3ms ^{15}N/^{13}C mixing times, respectively, of a ^{15}N, $^{13}C_{\alpha}$ NAL single crystal. One-dimensional spectra on the top and the side are the ^{13}C and ^{15}N CP spectra shown in Figure 3.2.A and 3.2.B. Strong inter-molecular correlations in a single crystal are achieved only under the higher mismatched condition.

Recoupling has been shown to assist the ^{15}N/^{13}C transfers when the mismatches are lower than the Hartmann-Hahn condition by 10 kHz. According to the Hamiltonians, the same effect should occur when the mismatch is higher as well. The stronger ^{1}H-irradiation brings the ^{1}H magnetization into the rotating frame more efficiently, and should provide superior recoupling; once the proton bath recouples the dilute spins, all the correlations between ^{15}N and ^{13}C should be observed in the HETCOR spectra. However, we only observed the intra-molecular correlations in the ^{15}N, $^{13}C_{\alpha}$ NAL single crystal sample in the presence of ^{1}H-irradiation at 40 kHz. When the field strength of ^{1}H-irradiation was increased to 60 kHz not only the intra- but also some inter-correlations were observed in the spectra (Figure 3.5.A). Comparing the spectrum in Figure 3.3.B, the

only difference is the strength of ^{1}H-irradiation, and it shows that the recoupling efficiency is improved by increasing the strength of the B_1 field. All the correlations expected in the unit cell were observed when mixing time was extended to 3ms (Figure 3.5.B).

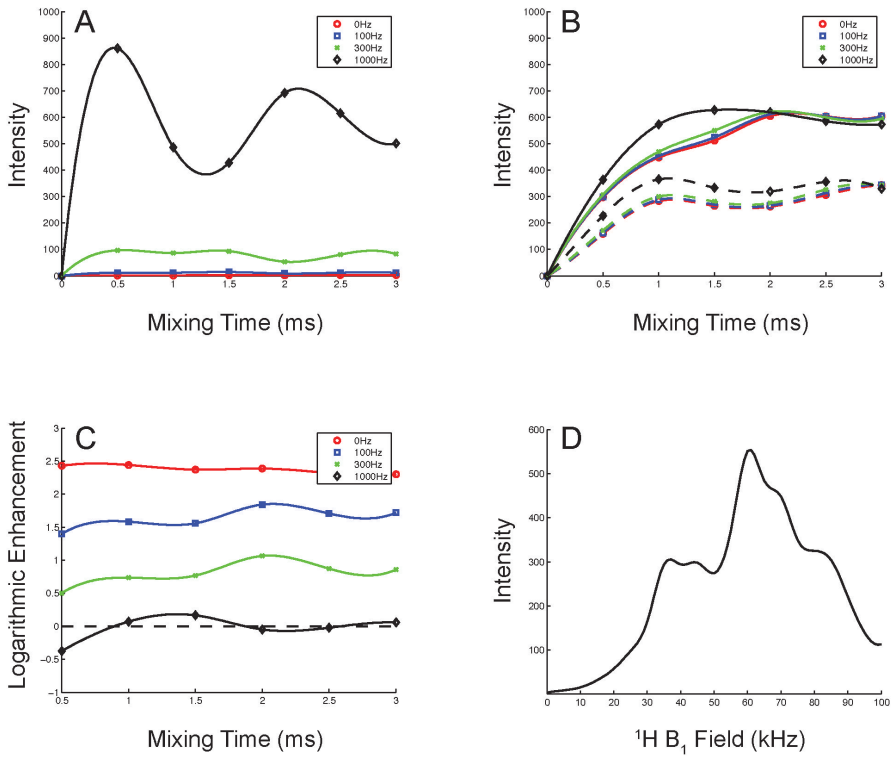

Figure 3.6 Simulations of the transfer efficiencies between ^{15}N and ^{13}C with various ^{15}N-^{13}C heteronuclear dipolar couplings.
A. Conventional ^{15}N/^{13}C CP transfer. B. ^{15}N/^{13}C CP transfer with ^{1}H-irradiation at 59 kHz (solid line) and 43 kHz (dash line). C. Logarithmic plot of enhancement by ^{1}H-irradiation. D. Mismatched profile of ^{1}H-irradiation. A. - C. the ^{15}N-$^{13}C_{\alpha}$ dipolar couplings were simulated for 0 (red), 100 (blue), 300 (green), 1000 (black) Hz with all other parameters kept the same. The buildup curves were sampled every 500 ms, and the lines connecting between the data points show the tendencies. D. The simulation was done when ^{15}N-$^{13}C_{\alpha}$ dipolar coupling equal to zero, and the strength of ^{1}H-irradiation was varied from 0 kHz to 100 kHz.

Simulations of the magnetization transfer in a ^{15}N, $^{13}C_{\alpha}$ NAL peptide were carried out with SIMPSON 3.0.1[121]. To simplify the spin system, only ^{1}H nuclei attached to the ^{15}N, C_{α}, C_{β}, and N-methyl groups were considered, and only the $^{15}N/^{13}C$ mixing period was simulated to evaluate the transfer efficiency. In the simulations, a 1kHz ^{15}N-^{13}C dipolar coupling was considered to be the best case. The regular $^{15}N/^{13}C$ transfer (Figure 3.6.A) is sensitive to ^{15}N-^{13}C dipolar couplings because they provide the only transfer pathway. The typical CP buildup curve[122] is observed in the simulation when the ^{15}N-^{13}C dipolar coupling is strong; the intensities increase proportionally to the magnitudes of the dipolar couplings, and the dipolar modulation also causes the oscillations in the magnetization buildup curve. The transfer efficiencies are poor when the ^{15}N-^{13}C dipolar couplings are small. However, in the presence of ^{1}H-irradiation (Figure 3.6.B), no matter the magnitude of the dipolar couplings, they tend to have similar transfer efficiencies. This demonstrates that the transfer mechanism is dominated by recoupling with the proton bath. The data in Figure 3.6.C show that transfers for weak ^{15}N-^{13}C dipolar couplings benefit from ^{1}H-irradiation, but that it can decrease the efficiencies for strong ^{15}N-^{13}C dipolar couplings. The mismatched profile (Figure 3.6.D) was simulated under the small dipolar coupling condition. Two local maxima show up asymmetrically when mismatched conditions are about ±10 kHz, which is similar to the simulations of ^{1}H-irradiation assisted ^{15}N spin diffusion, where the optimal mismatched conditions occur at ± 8%[110]. Both the experimental results and simulations suggest that the optimal conditions for ^{1}H-irradiation lie between ±5 kHz and ±15 kHz, mainly depending on the properties of the proton dipolar network. Better transfer efficiency can be observed at the higher mismatch condition because of the larger ^{1}H magnetization in

the rotating frame. In practice, the higher mismatched condition drives the inter-peptide correlations that distribute the magnetizations to the proton bath and more distant dilute spins. As a result, the transfer efficiencies would be decreased as shown in Figure 3.5.

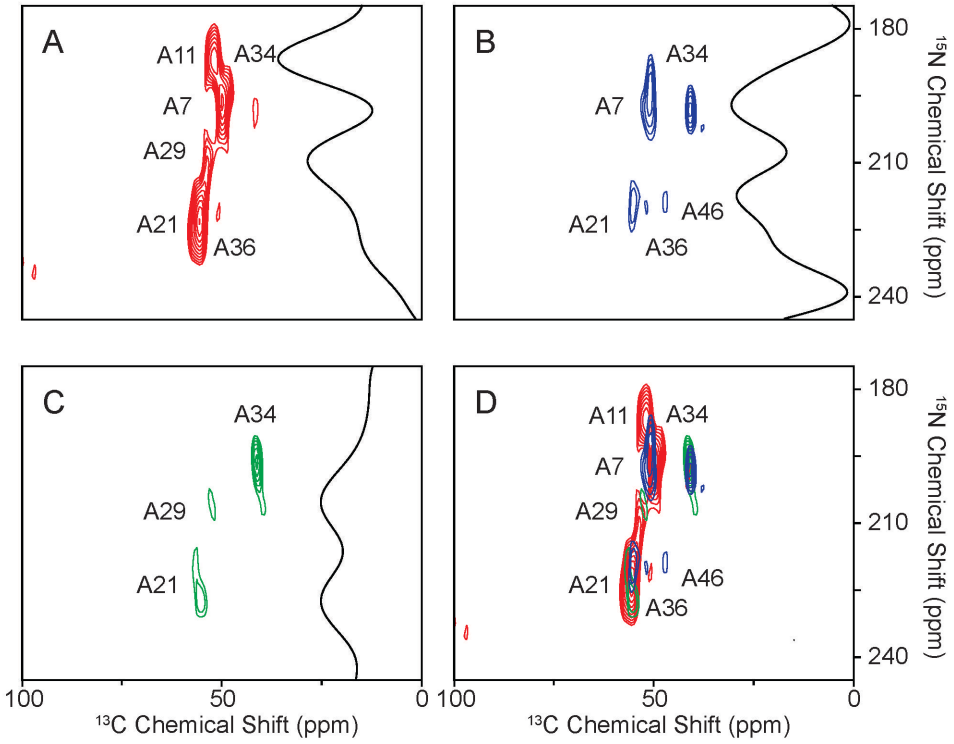

Figure 3.7 HETCOR spectra of selectively ^{15}N, $^{13}C_{\alpha}$ alanine-labeled Pf1 bacteriophage. The protein has eight alanine residues. A. Two-dimensional $^{15}N/^{13}C$ HETCOR without ^{1}H-irradiation. B. Two-dimensional $^{15}N/^{13}C$ HETCOR with ^{1}H-irradiation at 33.8 kHz. C. Two-dimensional $^{15}N/^{13}C$ HETCOR with ^{1}H-irradiation at 67.7 kHz. The slices shown in panels A., B., and C. were taken from 53.7 ppm in ^{13}C chemical shift dimension, corresponding to A29. D. This spectrum is a superposition of the spectra in panels A.(red), B.(blue), and C.(green); it displays all of the $^{15}N/^{13}C$ correlations in the alanine-labeled Pf1 bacteriophage, and demonstrates the possibility of observing all $^{15}N/^{13}C$ correlations regardless of the strength of their heteronuclear dipolar couplings by obtaining spectra under several different transfer conditions.

^{15}N, $^{13}C_{\alpha}$ alanine-labeled Pf1 bacteriophage was used to demonstrate the feasibility for the applications to aligned protein samples. The experiments were

performed at a relatively low temperature, to ensure that a single conformation of the protein was present. [123] All the resonances were assigned by comparisons to previous results. Signals from seven out of the eight alanine residues were observed with the regular HETCOR experiment (Figure 3.7.A). A7, A11, and A21 are strong and well resolved. A29 is merged with A21, and A34 and A36 are relatively weak comparing to the other peaks. The signal from A46 is not observed. With ^{1}H-irradiation at a lower mismatched condition of 33.8 kHz, two changes are apparent in the spectrum in Figure 3.7.B: the signal from A34 is increased by 50%, and the signal from A46 can be observed. For the higher mismatched condition at 67.7 kHz, A34 still gains 50% enhancement, while A21 is significantly reduced, which distinguishes between A21 and A29 in Figure 3.7.C. Other peaks were reduced in intensity in the presence of ^{1}H-irradiation, which serves to reinforce the agreement between the single crystal spectra and simulations. The superimposed spectrum shown in Figure 3.7.D contains all resonances that are expected from ^{15}N, $^{13}C_{\alpha}$ alanine-labeled Pf1 bacteriophage. Thus, be performing multiple experiments with varying strengths of ^{1}H-irradiation, it is possible to detect all ^{15}N/^{13}C correlation peaks from a protein, despite their widely varying magnitudes of heteronuclear dipolar couplings.

3.4 Conclusions

^{13}C-detected triple-resonance experiments provide spectra with higher sensitivity and more correlation resonances, as long as they performed under several different conditions of ^{1}H radiofrequency irradiations. The frequencies of the ^{15}N/^{13}C correlation

resonances provide valuable constraints for the calculation of protein structures in OS solid-state NMR. Moreover, $^{15}N/^{13}C$ transfer can be used as a filter to eliminate interference from natural abundance signals from the lipids[111]. ^{1}H-irradiation under mismatched Hartmann-Hahn conditions assists magnetization transfer from ^{15}N to ^{13}C. The experimental results obtained on single crystal and aligned protein samples, and simulations demonstrate the validity of the recoupling mechanism. The transfer mechanism relies primarily on the ^{1}H dipolar network, which is well-suited for OS solid-state NMR experiments, because the dipolar couplings are not averaged out by molecular or spinning motions. The spin dynamics are complex once the spins are recoupled by ^{1}H-irradiation, and therefore, some of the transfer efficiencies may be lost, especially when the ^{15}N-^{13}C dipolar couplings are large. However, this method is a complementary to other procedures because of the improved transfer efficiencies for small ^{15}N-^{13}C dipolar couplings. Both mismatched conditions are used in order to enhance the intensities of different signals. Combined with conventional spin-lock CP transfer, these experiments have the potential to correlate essentially all of the nearby residues in a protein, providing the basis for a systematic assignment method and the simultaneous measurement of both the ^{13}C and ^{15}N chemical shift frequencies.

3.5 Methods

3.5.1 ^{15}N, $^{13}C_{\alpha}$ NAL single crystal spectra

The NMR experiments were performed on a Varian Inova spectrometer with ^{1}H, ^{13}C, and ^{15}N frequencies of 500.125 MHz, 125.76 MHz, and 50.68 MHz, respectively. A

home-built modified Alderman Grant coil (MAGC) triple-resonance probe[112], which was designed for the lossy biological samples, was used for these experiments. All the spectra were obtained at room temperature. The ^{1}H carrier frequency was set at 4.7 ppm; the ^{13}C carrier frequency was set at 54.94 ppm; and the ^{15}N carrier frequency was set at 79.26 ppm. ^{13}C- and ^{15}N-detected spectra were acquired with 512 and 1024 complex points in the direct dimensions, respectively. CP spectra were acquired with 64 scans and 40 μs dwell time. ^{15}N-^{13}C dipolar coupling SLF spectra were acquired with 4 scans, 100 μs dwell time and 96 points in the indirect dimension, and 40 μs dwell time in the direct dimension. HETCOR spectra were acquired with 4 scans, 100 μs dwell time and 192 complex points in indirect dimension, 40 μs dwell time and 512 complex points in the direct dimension. Mixing time of $^{1}H/^{15}N$ and $^{1}H/^{13}C$ CP was 1ms, and $^{15}N/^{13}C$ CP was 1ms or 3ms. For all the experiments the recycle delay was 6 s. Pre-saturation consisted of thirty 90° pulses with 200 μs delay in between, and the z-filter delay was 5 ms. The strength of the continuous wave decoupling on ^{15}N and ^{13}C channels was 40 kHz, and all other irradiations were performed at 50 kHz, except for the variable ^{1}H-irradiation during $^{15}N/^{13}C$ mixing period. The experimental data were zero filled to 512 and 1024 data points in the indirect and direct dimensions, respectively, and were multiplied by a sine bell window function prior to Fourier transformation.

3.5.2 ^{15}N, $^{13}C_{\alpha}$ alanine-labeled Pf1 bacteriophage spectra

The phage sample was prepared as described previously[124]. The final phage sample was diluted to 40 mg/ml with sodium borate buffer (pH=8), and the final volume was 150 μl. The spectra were obtained at -2°C to ensure that the coat protein was in its

'low temperature' conformation. The ^{1}H carrier frequency was set at 4.7 ppm; the ^{13}C carrier frequency was set at 100 ppm, and the ^{15}N carrier frequency was set at 213 ppm. HETCOR spectra were acquired with 400 scans, 100 μs dwell time, 32 complex points in the indirect dimension, and 25 μs dwell time and 256 complex points in the direct dimension. Mixing time of $^{1}H/^{15}N$ CP was 1ms and $^{15}N/^{13}C$ CP was 3ms. The recycle delay was 4 s. All other conditions were the same as described above for the single crystal.

3.5.3 Simulations

Only the $^{15}N/^{13}C$ mixing period was simulated to evaluate the transfer efficiency. The simulations were carried out with SIMPSON 3.0.1. The model was based on the single crystal structure[110]; however, the spin system was simplified to ^{15}N, $^{13}C_{\alpha}$, the ^{1}H attached to the N, C_{α}, C_{β}, and N-methyl group. Euler angles "β" in the input file were manually adjusted to 90° for ^{1}H-^{15}N, ^{1}H-$^{13}C_{\alpha}$ and ^{15}N-$^{13}C_{\alpha}$ dipolar couplings, and therefore, the dipolar couplings can be varied without angular considerations. For all the simulations, ^{1}H-^{15}N and ^{1}H-$^{13}C_{\alpha}$ dipolar couplings were 12.18 and 22.80 kHz according to the bond lengths. ^{15}N-$^{13}C_{\alpha}$ dipolar couplings were adjusted manually according to each case. $^{15}N/^{13}C$ mixing period was 3 ms for the mismatched profile simulation.

Chapter 3, in full, is a reprint of the material "^{1}H assisted $^{13}C/^{15}N$ heteronuclear correlation spectroscopy in oriented sample solid-state NMR of single crystal and magnetically aligned samples" as it appears in J. Magn. Reson. 221(1):37-44 by Lin EC, Opella SJ. The thesis author was the primary author of the paper.

Chapter 4 Sampling Scheme and Compressed Sensing Applied to Solid-State NMR Spectroscopy

4.1 Abstract

We describe the incorporation of non-uniform sampling (NUS) compressed sensing (CS) into Oriented Sample (OS) Solid-state NMR for stationary aligned samples and Magic Angle Spinning (MAS) Solid-state NMR for unoriented 'powder' samples Both simulated and experimental results indicate that 25% to 33% of a full linearly sampled data set is required to reconstruct two- and three-dimensional solid-state NMR spectra with high fidelity. A modest increase in signal-to-noise ratio is accompanies the reconstruction.

4.2 Introduction

NMR spectroscopy has intrinsically low sensitivity. As a result, long periods (days – weeks) of signal averaging are often required to obtain signals in multidimensional experiments on proteins and other biopolymers that can be confidently identified above the noise level. However, progress is being made along several avenues to improve the sensitivity of the NMR experiments and decrease the amount of time required for signal averaging, including the use of very low probe and sample temperatures[125], dynamic nuclear polarization (DNP)[12; 14], and shortening the recycle delay by reducing T_1 of the detected magnetization[91]. However, these

approaches may be inapplicable to some samples, especially proteins and their complexes, because of the destabilizing and denaturing effects of adding chemicals or freezing the samples. For example, membrane proteins must reside in liquid crystalline phospholipids under physiological conditions of temperature and pH in order to function and adopt their native structures. Alternatively, several spectroscopic approaches generally referred to as non-uniform sampling (NUS) are being developed to improve sensitivity that do not require perturbation of the sample or its environment [13].

The most general approach to increasing the efficiency of NMR experiments is to acquire less data. Either lengthening the sampling interval or truncating the acquisition time in the indirect dimensions can reduce the experimental time, but at the cost of lower resolution or aliasing of signals. Here we describe a NUS scheme that consists of random sampling grids that can minimize these disadvantages for applications to solid-state NMR of stationary, aligned samples as well as unoriented 'powder' samples undergoing magic angle spinning. The archetypical examples are single- and poly- crystalline samples of small molecules, such as model peptides. However, our primary motivation is to improve the sensitivity of structure determination proteins in biological supramolecular assemblies, such as virus particles and membranes using orientated samples (OS) solid-state NMR and rotationally aligned (RA) solid-state NMR, which involve stationary and spinning experiments, respectively.

The free induction decays (FIDs) are the directly or indirectly observed time dependent signals that decrease in intensity over time due to relaxation. Traditionally, the intensities in the form of voltages at audio frequencies are measured at regular intervals in order to accommodate the requirements of the fast Fourier transform algorithm, which

enables the analysis of signals in the frequency domain instead of the time domain where they are acquired. The most commonly used approach to reducing the number of data points collected in the indirect dimension of a multidimensional experiment is to perform uniformly distributed random sampling, for example under-sampling the signal in the indirect dimensions and reconstructing the spectra by numerical methods. Linear prediction (LP)[126] and maximum entropy (MaxEnt)[38; 40; 41; 127] are widely applied to multi-dimensional NMR signal reconstructions, and recently maximum entropy interpolation (MINT)[128; 129] has been applied successfully in MAS solid-state NMR experiments. LP extrapolation is applicable when the signal-to-noise ratio is high or the signals are not highly truncated, otherwise the signal processing creates artifacts or decreases resolution[38]. To avoid these issues and provide high quality reconstructions, NUS and MaxEnt or MINT can be combined. Other approaches are proposed to reconstruct the spectra without using entropy as constraint, such as, projection-reconstruction (PR)[130; 131], multi-dimensional decomposition (MDD)[42; 43], GFT[132], non-uniform Fourier transformation (nu-FT)[133], spectroscopy by integration of frequency and time domain information (SIFT)[134-136], among others. Compressed sensing (CS) [18; 19; 137], a method under rapid development in the fields of imaging and signal reconstruction, has been successfully applied to MRI [16; 17]. Recent applications of CS in solution NMR experiments [15; 138-141] have shown that it requires less data than MaxEnt for comparable results, and has better performance on weak signals [138]. Remarkably, this method has been used to reconstruct three- and four-dimensional solution NMR data sets with only 0.8% sampling [141]. The underlying principle of CS is that if the data set is sparse enough, then very limited information is

sufficient to reconstruct the whole data set with high fidelity. Consequently CS is well suited for NMR spectroscopy because experimental NMR data can be treated as sparse, although there are significant quantitative differences between the data from solution NMR and solid-state NMR experiments. Here we describe the adaptation and steps towards optimization of CS for the stationary sample and MAS solid-state NMR.

Non-uniformly distributed data sampling has several advantages. First of all, it can be tailored to emphasize the early, more intense portion of the FIDs, where the signal-to-noise ratios are the highest. Several schemes have been proposed for solution NMR conditions [142-146]. Even though these methods are robust, they still have higher risks of distortions for sampling the signals in solid-state NMR experiments due to the generally faster signal decay in the time domain. Among these methods, the sine-weighted Poisson-gap sampling method[144] appears to be closest to the requirements for solid-state NMR. Here we demonstrate the effects of varying the most relevant parameters, such as the sampling percentage, uniform sampling region, and the exponential decay weighting function in order to tailor the NUS schemes for solid-state NMR experiments [146]. Sampling percentage refers to the ratio of non-uniformly sampled points (Figure 4.1.B) to the uniformly sampled points (Figure 4.1.A). The uniform sampling region is set in the beginning of the free induction decays. An exponential decay weighting function modulates the random sampling in order to minimize sampling the low signal-to-noise ratio region, as shown in Figure 4.1.B. We optimized the NUS schemes for oriented samples, such as single crystals of model peptides and magnetically aligned proteins, and then extended the schemes to unoriented ‘powder’ samples of model proteins and proteins undergoing magic angle spinning.

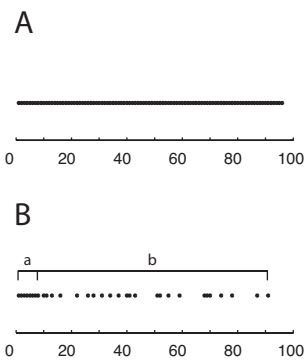

Figure 4.1 Illustrations of sampling schemes.
A. Uniform sampling scheme (regular experiments). B. Non-uniform sampling (NUS) scheme consisted by a. the uniform sampling region and b. the sampling region that the sampling probabilities are modulated by an exponential decay weighting function.

A sparse data set refers to the situation where only a few basis functions have non-zero coefficients in a defined space. Under this condition, it is possible to use only a small amount of information to reconstruct the entire data set; therefore, the concept is referred to as compressed sensing[19]. Theoretically, using l_0 norm minimization it is feasible to find the sparest solution (the original data) subjected to the constraints (the limited information obtained). However, l_0 norm minimization is a NP-hard (non-deterministic polynomial-time hard) problem, which means that the upper bound of computational time is the polynomial expression of the size of input; as a result, it is not possible to solve this problem efficiently. Instead, l_1 norm minimization is used to obtain an approximation of the solution. By applying Fourier transformation to these data, high-resolution spectra can be obtained from sparse data.

Based on the properties of NMR signals, we can solve the minimization problem by using a Lagrange multiplier, as shown in Equation 4.1.

$$\left\| wSFx - y \right\|_2^2 - \lambda \left\| x \right\|_1 \qquad \text{Equation 4.1}$$

F is the discrete Fourier transform operator; *S* is the under sampling operator; *w* is the weighting; *x* is the solution, *y* is the observation, and λ is Lagrange multiplier. In terms of NMR spectroscopy, *y* is the FID measured in the time domain, *x* is the reconstructed signal in the frequency domain, *S* is the NUS scheme, and *w* is the decay rates of the signals. *w* should be estimated from the knowledge, and the NUS schemes are generated with the same conditions. Since the reconstructed space is larger than the sampling space, the under sampling operator is applied first so that both dimensions are in agreement, as shown in the first term in Equation 4.1. Iterative soft thresholding (IST)[18; 137] is applied to efficiently solve this minimization problem. The thresholding is adjusted during each iteration, and only signals with intensities higher than the thresholding are included in the reconstruction.

4.3 Results

Compressed sensing was originally developed for sparse data. It is highly effective with solution NMR spectra because the resonance line widths are often <20 Hz and spread over a range of ~10 kHz. In contrast, in solid-state NMR spectra, individual signals and the dipolar doublets generated in separated local field experiments usually have much broader line widths, between 200 Hz and 400 Hz, spread over a similar frequency range.

We randomly generated one-dimensional FIDs from five or ten frequencies. Each example consisted of forty different FIDs with a decay rate corresponding to 400 Hz ± 100 Hz line widths of signals observed in solid-state NMR spectra. These decay rates

correspond to typical sold-state NMR signals, and once CS is demonstrated to work under these conditions it is likely to work with narrower line width signals (sparser data) obtained with improved experiments and instrumentation, and in favorable cases. The FIDs consist of 128 points with a dwell time of 40 μs. Various amplitudes of noises were added to each FID. In addition to a noiseless spectrum, we obtained spectra with signal-to-noise ratios of 32, 16, 8, 4 and 2. Fifty NUS schemes were randomly generated under each set of conditions, which were varied by the parameters listed above. Sampling percentages of 50%, 33%, 25%, 20%, 15%, and 10% were applied to the128 points in the time domain. The uniform sampling regions were 75%, 50%, 25%, 10%, and 0% of the sampling size. The exponential decay rates of the weighting functions were chosen to be 1, 2, 3, 4 and 5-times the decay rates of original FID. Taken together a very large number of tests were performed in this semi-empirical analysis; 150 NUS schemes with different parameters were randomly generated fifty times, and were applied to eighty spectra with six different signal-to-noise ratios. We evaluated the performance of reconstructions by l_2 norm (L2) as indicated in Equation 4.2 [146],

$$\sum_{i} \left| x_i - y_i \right|^2 \qquad \text{Equation 4.2}$$

where y_i and x_i are the intensities in the noiseless and reconstructed spectra respectively at the frequency i.

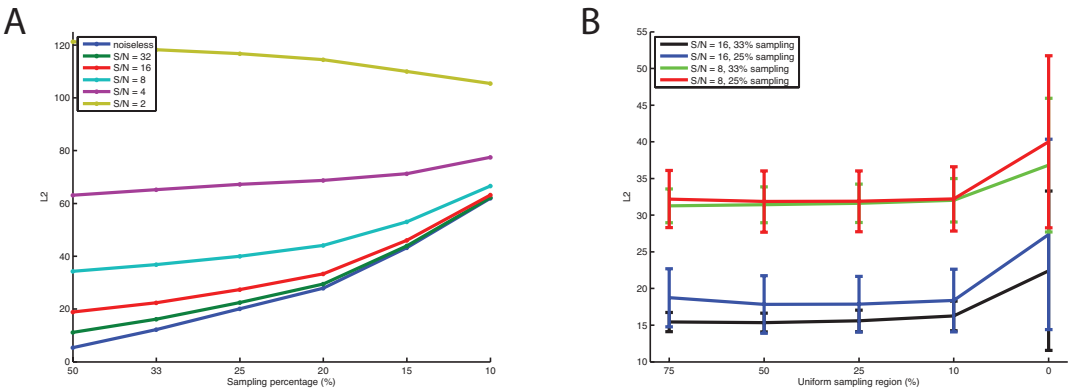

Figure 4.2 The performance evaluations of sampling schemes.
The values shown in the figure are the averages of every fifty NUS schemes generated by different conditions that are applied to the simulated spectra. Lower L2 values indicate higher similarities between the reconstructed and noiseless spectra. A. The qualities of reconstructions with various sampling percentages under different S/N ratios. It shows that the reconstructions have similar tendencies to the ideal signal if the signals have S/N ratios ~10, and the errors of reconstructions increase much faster if the sampling percentage lower than 20%. B. The qualities of reconstruction by adding uniform sampling region for 33% and 25% sampling. The reconstructions are improved by adding for 10% to 25%uniform sampling region. The error bars indicate the standard deviations of L2, which are significantly improved by introducing uniform sampling region, implying the qualities reconstructions are more stable.

The forty simulated spectra that were generated were used to evaluate the overall performance of each NUS scheme. The averaging of L2 was determined by comparing the noiseless and reconstructed spectra (Figure 4.2.A). Since the primary goal of this development is to reduce the experimental time while preserving the quality of the experimental data, we first investigated the percentage of under-sampling that could be tolerated by CS with solid-state NMR signals. The probability of the random sampling is modulated by an exponential decay function with the decay rate of 400 Hz. The relationships between sampling percentages under different signal-to-noise ratios in terms of L2 are shown in Figure 4.2.A. The trends of L2 rising with decreasing sampling percentage were observed for spectra with signal-to-noise signal ratios > 4. As expected,

larger errors were apparent when the signals were generated with fewer restraints. The results suggest that to obtain a reliable reconstruction, the lowest signal-to-noise ratio that is viable is ~ 10. The growth rates of L2 are faster when the sampling percentage is < 20%, suggesting that to maintain the quality of reconstructions, at least 20% of the original data is needed. These results have been confirmed under other spectroscopic conditions where most reconstructions were performed with at least 20% of the full data set [15; 138].

The performance of NUS schemes is improved by incorporating a uniform sampling region at the beginning of the FID because this is where the signal-to-noise ratios are highest. The first few points are especially important, especially when the total number of sampled points is very limited. The uniform sampling regions examined ranged from 0% to 75% of the sampled data, and this provides similar results to both "Poisson-Gap Sampling"[144] and "Non-uniform weighted sampling"[147]. Figure 4.2.B shows that including 10% and 25% uniform sampling regions improves L2 by 10% to 20%. As the uniform region becomes a larger percentage of the data, the effect of its inclusion becomes similar to truncation, and the reconstructed spectra lose resolution, which is reflected in the case of 25% sampling with 75% uniform sampling region. The standard deviations of L2 were significantly reduced by the inclusion of the uniform region at the beginning of the FID, demonstrating that the stability of reconstructions is improved.

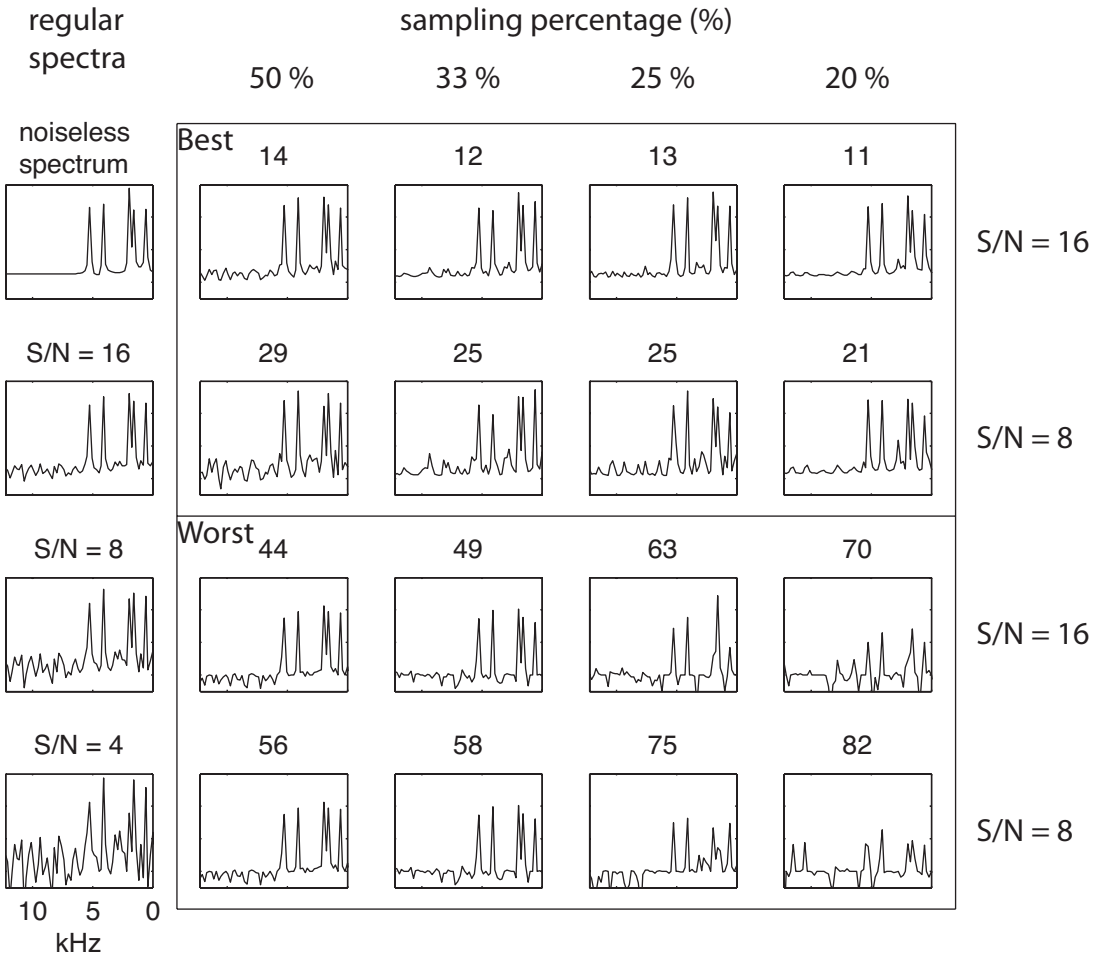

Figure 4.3 Best and worst reconstructed spectra of 25% sampling with 0% to 50% uniform sampling region on the spectra with S/N ratios equal 16 and 8.
These spectra are chosen from fifty reconstructions of a selected simulated spectrum, and the criterion is based on L2, which is shown on each spectrum. The regular spectra shown in the left column for comparing the qualities of spectra acquired with the same amount of time. 25% sampling with S/N=16 should be compared to the regular spectrum with S/N=8, and 25% sampling with S/N=8 should be compared to the regular spectrum with S/N=4. Most of the peaks can be reasonably identified after the improvement.

One of the simulated spectra and its “best” and “worst” reconstructed spectra are compared in Figure 4.3. In order to investigate the limits of this approach to NUS, we examined reconstructions of 25% sampling with 0%, 10%, 25%, and 50% uniform sampling region for the signals with signal-to-noise ratios equal to 16 and 8, as shown in

Figure 4.3 based on the L2 behaviors shown in Figure 4.2.B. From the analysis of L2, we find that 25% sampling and a signal-to-noise ratio of ~ 8 are about the minimums for reliable reconstructions, thus spectra obtained under these conditions are most sensitive to improvements due to variations in the sampling scheme. By adding the uniform sampling region, even the most difficult cases can be improved. The resolutions degrade slightly when the uniform sampling region increases, and, therefore, we find that 10% or 25% uniform sampling regions give the best results. Generally speaking, the signals can be identified with reasonable confidence, and the spectral resolution maintained even in the low frequency region (<2 kHz) in separated local field (SLF) spectra. Simulated spectra that would require the same amount of experimental time but have different signal-to-noise ratios are also provided for comparisons of the quality of reconstructed spectra.

As is well known, the signal-to-noise ratios can be doubled by a four-fold increase of experimental time. Conversely, using one quarter of the experimental time gives one half of the signal-to-noise ratio. Therefore, we compare spectra with signal-to-noise ratios of 4, 8, and 16 obtained with uniform sampling to equivalent spectra obtained with between 8 % and 25% non-uniform sampling. The reconstructed spectra all have higher signal-to-noise ratios than the uniformly sampled spectra acquired in the same amount of experimental time. In addition, two- to five-fold increases in the decay rates from the weighting function were tested, but the reconstructions were not improved even with the addition of uniform sampling regions at the beginning of the FIDs.

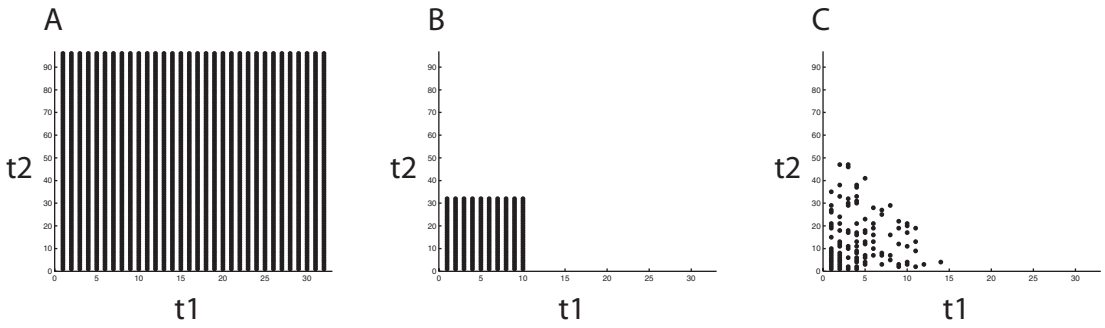

Figure 4.4 Illustrations of two-dimensional sampling schemes.
A. Regular sampling scheme B. Truncated sampling scheme (10% of regular sampling scheme) C. NUS scheme (33% of truncated sampling scheme).

Similar results were obtained with more crowded spectra (10 dipolar doublets with line widths of 400 ± 100 Hz span spread over +/- 10 kHz). We found the optimal conditions to correspond to 33% sampling with a 25% uniform sampling region at the beginning of the FID. However, 25% sampling is also adequate to provide reliable reconstructions. The same methods used to optimize the two-dimensional NUS schemes were applied to three-dimensional schemes. In practice, it generally takes too long to sample the whole space (Figure 4.4.A) in these higher-dimensional experiments. Therefore, the typical strategy is to truncate the sampled space (Figure 4.4.B) to 10% - 25% of the full space to perform the experiments within a reasonable amount of time, and then use LP to improve the resolution of the signals. Taking this into consideration, we designed the sampling percentage for two-dimensional NUS schemes based on the truncated space instead of the whole sampling space (Figure 4.4.C). The optimized two-dimensional NUS schemes correspond to 25% - 33% sampling with 12.5% uniform sampling region over a 15% truncated space.

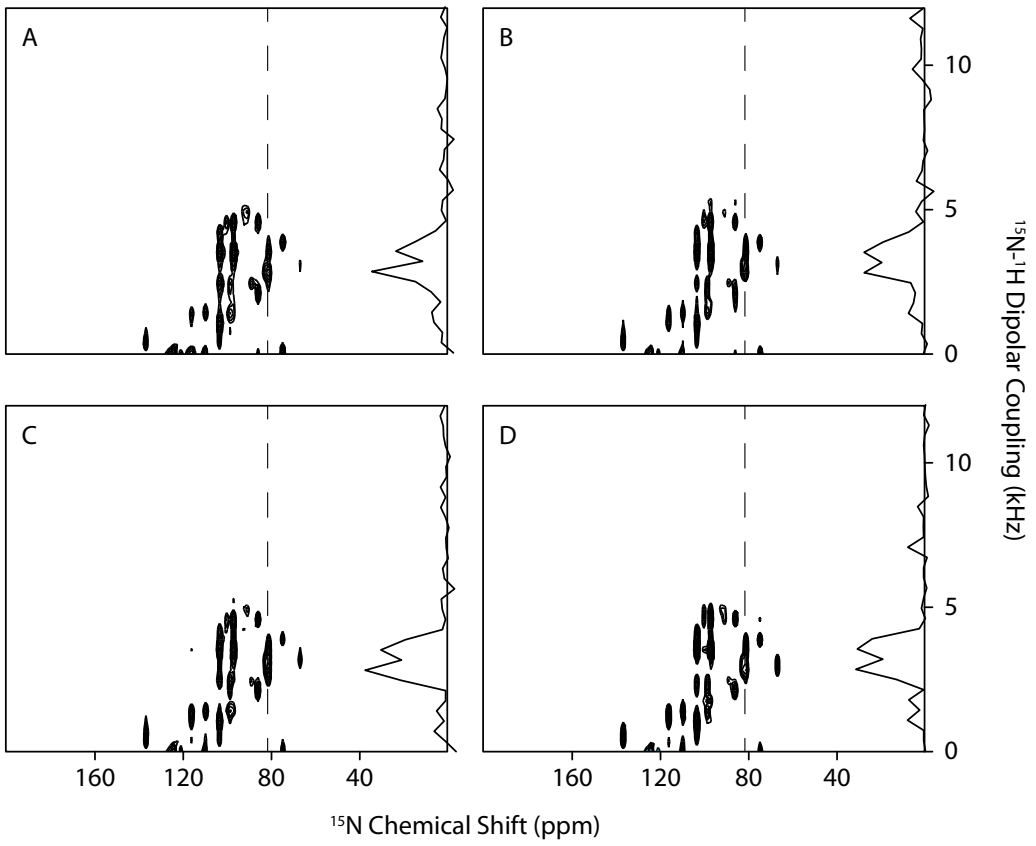

Figure 4.5 ^{15}N-detected SLF spectra of Pf1 protein in DHPC/DMPC bicelles.
A. Fully sampled spectrum with 80 t_1 points. Reconstructions from B. 50%, C. 33% and D. 25% sampling. Lagrange multiplier is 0.01. The slices are extracted from 81 ppm.

The optimization NUS schemes is illustrated with SLF spectra obtained using the SAMPI4 experiment on the membrane-bound form of uniformly ^{15}N labeled Pf1 coat protein in DMPC (1,2-dimyristoyl-*sn*-glycero-3-phosphocholine) / DHPC (1,2-dihexanoyl-*sn*-glycero-3-phosphocholine) bicelles. The sensitivity (signal-to-noise ratio ~10) and line widths of spectra are similar to those in the simulations. The SLF spectrum was acquired with 80 t1 points, shown in Figure 4.5.A, to which was applied Fourier transformation in the t_1 dimension without additional processing. The reconstructions from 50%, 33%, and 25% NUS with a 20% uniform sampling region are shown in Figure

4.5.B, 4.5.C, and 4.5.D, respectively. All the reconstructions yield well-resolved spectra, which suggests that the optimized NUS schemes are applicable to SLF experiments of membrane proteins in phospholipid bilayers.

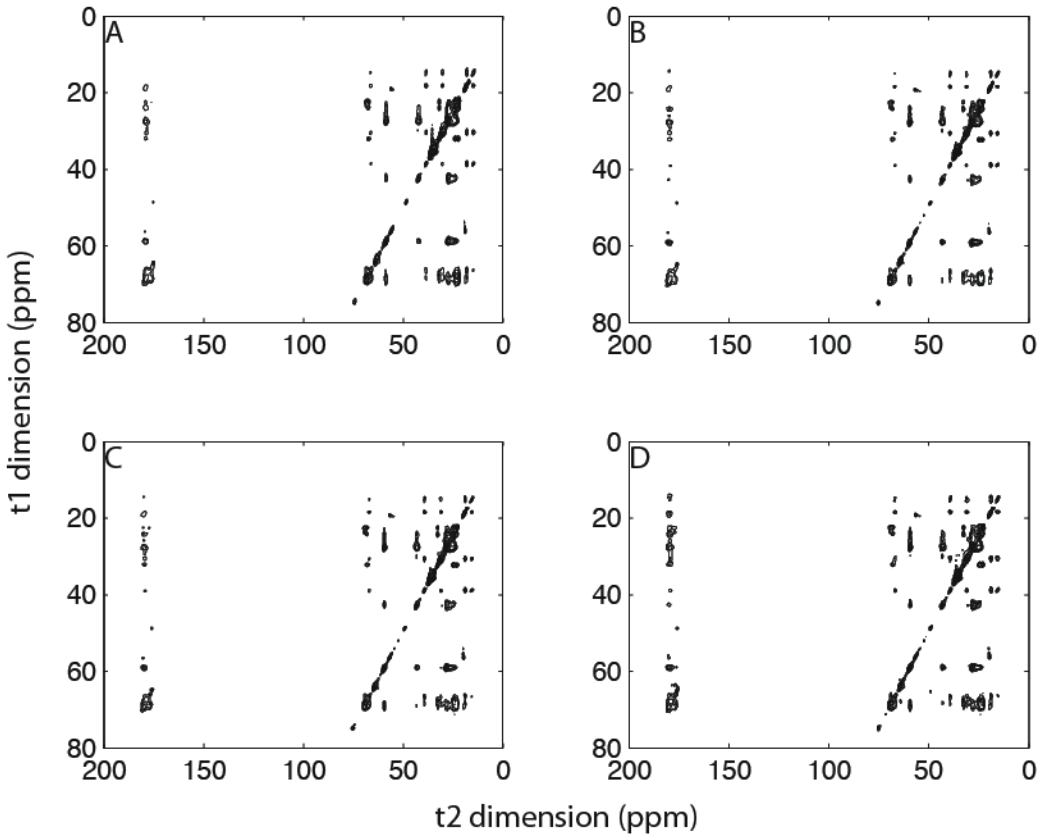

Figure 4.6 $^{13}C/^{13}C$ correlation spectra of MerF protein in 14-O-PC liposome with 20ms mixing time.
A. Fully sampling Fourier transform spectrum with 64 scans. Reconstructions from B. 50%, C. 33% and D. 25% sampling also with 64 scans.

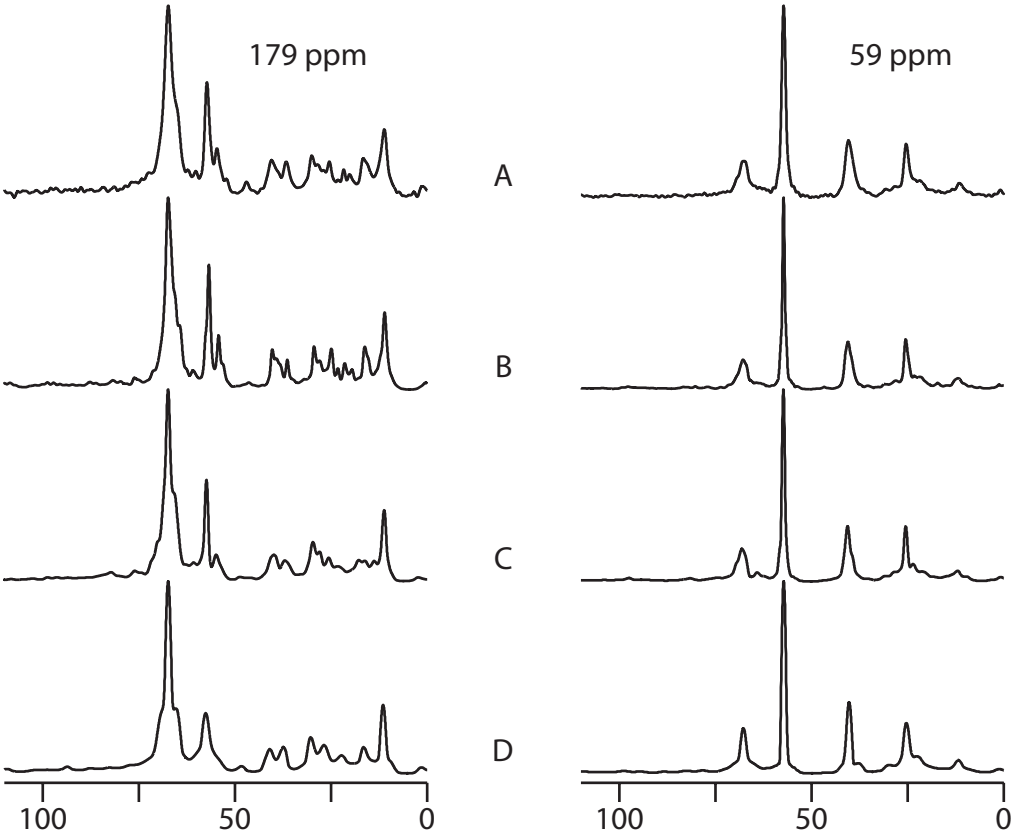

Figure 4.7 Slices extracted from 59 ppm and 179 ppm in the t2 dimension from the $^{13}C/^{13}C$ correlation spectra of MerF protein in 14-O-PC liposome.
From the bottom to the top, regular experiment, reconstructions from 50%, 33%, and 25% respectively, where the strongest peaks are normalized. The average signal to noise ratios of cross peaks in 50%, 33%, and 25% sampling spectra are 1.48, 0.90, and 0.78 folds relative to the regular spectrum, respectively.

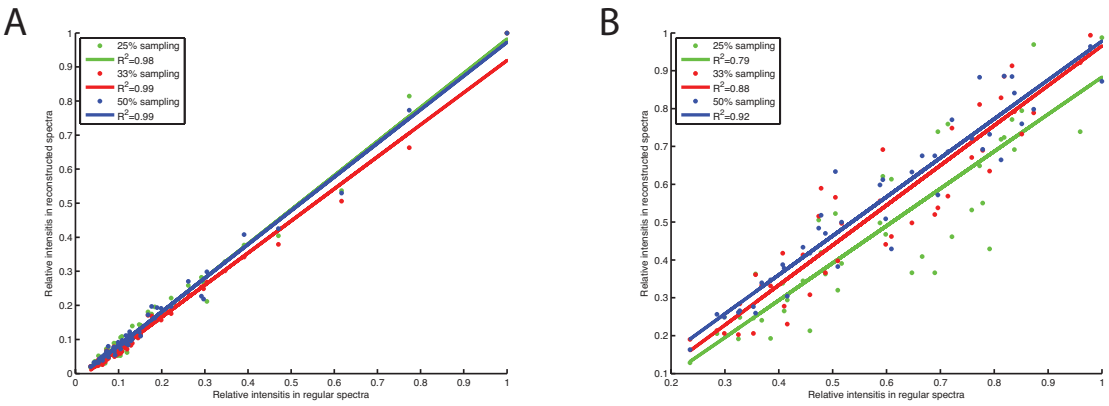

Figure 4.8 Correlation plots of the intensities between regular and reconstructed spectra of the $^{13}C/^{13}C$ correlation spectra of MerF protein in 14-O-PC liposome.
All the intensities are normalized to their own spectra. A. Correlation plots of diagonal and cross peaks. B. Correlation plots of cross peaks.

Using a 20% uniform sampling region, we demonstrated the application of NUS with two-dimensional $^{13}C/^{13}C$ correlation experiments on the membrane protein MerF in aligned bicelles. 96 t_1 complex points were acquired in the conventional $^{13}C/^{13}C$ correlation experiment (Figure 4.6.A) and 48, 32, and 24 t_1 complex points were acquired in the NUS experiments, shown in Figure 4.6.B, 4.6.C, and 4.6.D, respectively. No significant differences were observed between the regular and reconstructed spectra. We extracted spectral slices at 59 ppm and 179 ppm, which are representative of the Cα and CO spectral regions in Figure 4.7, where the strongest peaks are normalized. The signals are successfully reconstructed from the sparse region (59 ppm) with various sampling percentages. When the sampling percentage is < 25%, the line shapes are simplified, which may result in distortions. An advantage of using oriented sample solid-state NMR spectroscopy for protein structure determination is that it is based on frequency measurements, and line shape distortions or broadenings do not affect the results. For the crowded region (179 ppm), reconstructions from 50% data compare favorably with the

regular signals and even provide improved signal-to-noise ratios [148]. However, fine structure of the signals is lost as the sampling percentage is reduced. These effects are caused by over-compression, which means that either the sampling percentage is too low or the information in a crowded region is too large to compress. To compare the reconstructed and regular spectra, we measured the intensities of 61 diagonal and cross peaks, and plot the correlations in Figure 4.8. The overall (diagonal and cross peaks) correlations show very high fidelity between reconstructed and regular spectra, which are insensitive to the sampling percentages. For the cross peaks, the high correlations (~0.9) are found with 33% and 50% sampling, but decrease to about 0.8 for 25% sampling. The average signal-to-noise ratios of cross peaks in 50%, 33%, and 25% sampling spectra are 1.48, 0.90, and 0.78, respectively, relative to the regular spectrum, which reflects the impact of T_2 on the signal-to-noise ratios due to the relative increase in noise towards the end of the FIDs. The results are consistent with the sensitivity enhancement equation in that the maximum enhancement is achieved when the maximum acquisition (t_{max}) is $1.26T_2$ [148]. In this experiment T_2 is about 3ms and t_{max} is 3.8ms for 50% sampling, and the largest enhancement is obtained under these conditions. Another way to evaluate the sensitivity of NUS schemes has been proposed according to the sampling points, spectral widths and T_2 [149]. The "relative sensitivity" of these three sampling schemes (50%, 33%, and 25%) are 0.58, 0.46 and 0.38, and the "peak-to-side-lobe ratio" of them are 6.61, 5.13, and 5.97. Even though, the signal-to-noise ratios decrease slightly, the overall performance of the experiments is still improved when the savings in total experimental time is taken into account.

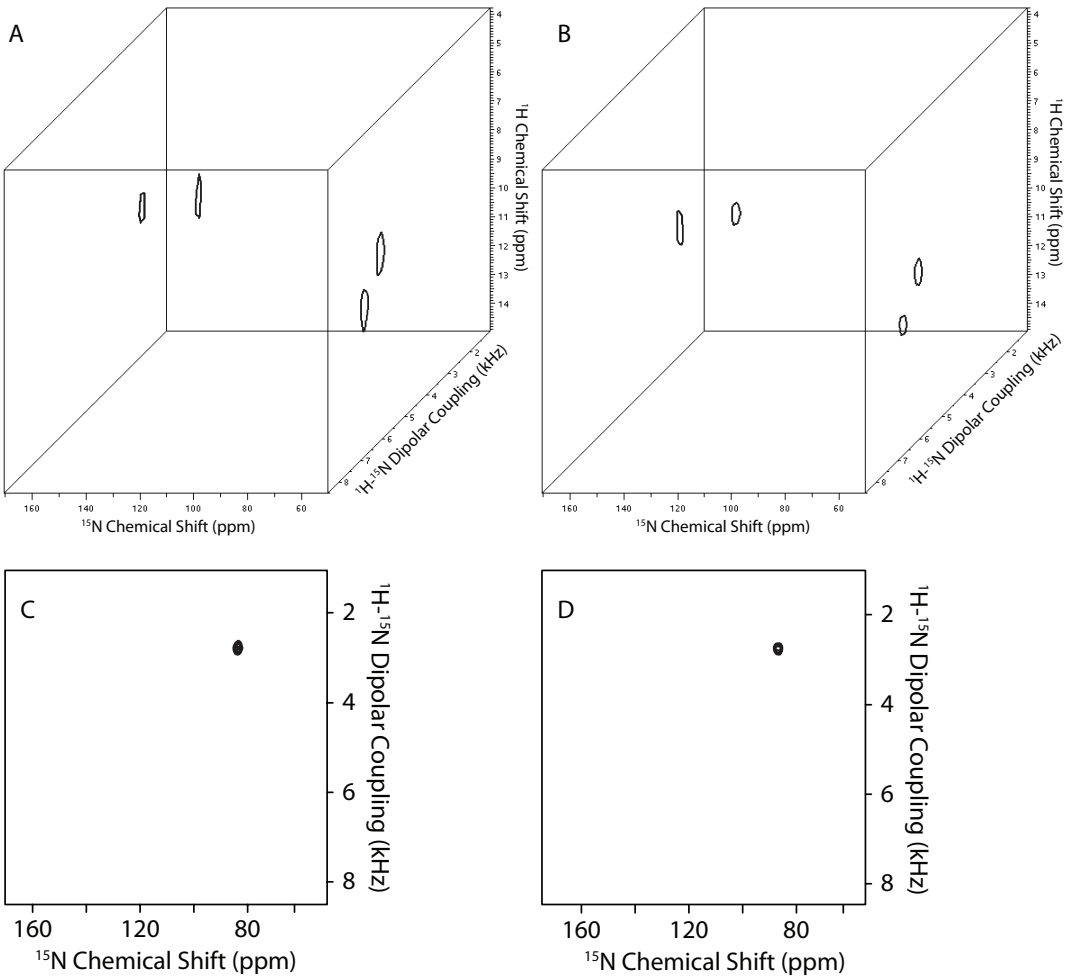

Figure 4.9 Three-dimensional HETCOR-SAMMY spectrum and its reconstructed spectra of ^{15}N-labeled NAL single crystal.
A. Conventional three-dimensional HETCOR-SAMMY spectrum (32 t1 complex points, 96 t2 points). B. Reconstructed three-dimensional HETCOR-SAMMY spectrum 614 points (20%). C, and D. are the two-dimensional planes extracted from the ^{1}H chemical shift at 12 ppm in A.,and B., respectively.

We also incorporated the NUS schemes described above into a three-dimensional HETCOR/SLF experiment[150], which provides correlations among ^{1}H chemical shifts, ^{1}H-^{15}N dipolar couplings, and the ^{15}N chemical shifts measured in the direct dimension. The conventional (Figure 4.9.A and 4.9.C) and NUS (Figure 4.9.B and 4.9.D) experiments are first demonstrated on a single crystal of ^{15}N-labeled N-acetyl-leucine

(NAL) at an arbitrary orientation. 20% of the sampling points (614 points) were selected based on the same rules as employed in the two-dimensional NUS schemes, and the size of the uniform sampling region is 20% of the selected sampling points. 20% NUS spectra show comparable results with the fully sampling spectra; however, compared to the performance in solution NMR experiments, there should be opportunities for further optimization [141] even for the broader line widths encountered in solid-state NMR spectra.

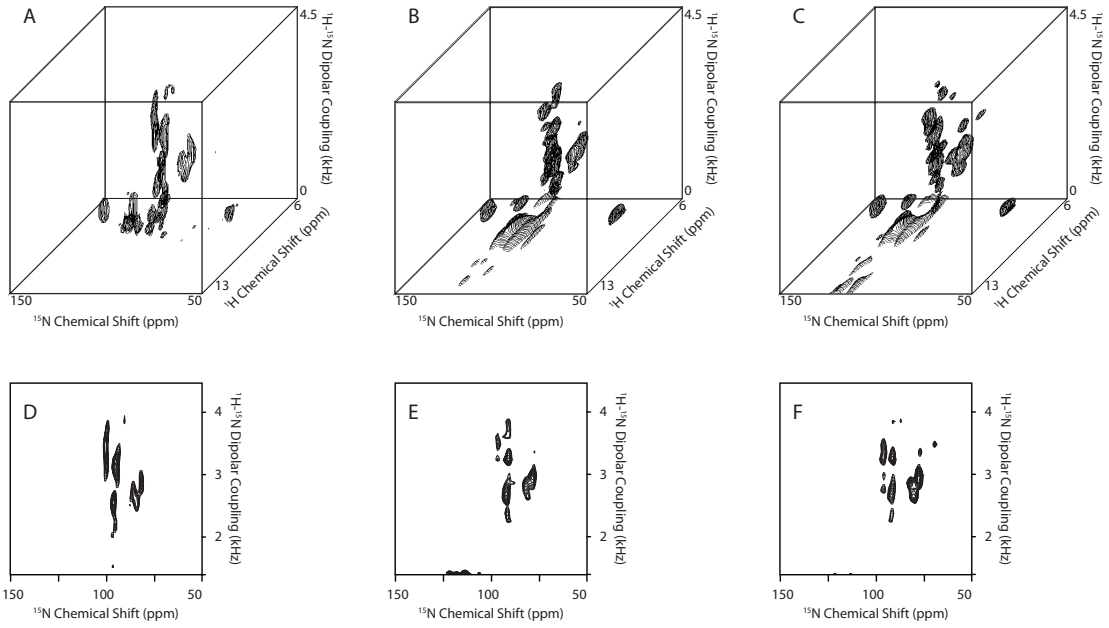

Figure 4.10 Three-dimensional HETCOR-SAMMY spectrum and its reconstructed spectra of ^{15}N-labeled pf1 coat proteins.
A. Conventional three-dimensional HETCOR-SAMMY spectrum (20 t1 complex points, 32 t2 points, and 40 scans). B. Reconstructed three-dimensional HETCOR-SAMMY spectrum (212 points, and 40 scans). C. Reconstructed three-dimensional HETCOR-SAMMY spectrum (212 points, and 120 scans). D, E., and F. are the two-dimensional planes extracted from the ^{1}H chemical shift at 9.5 ppm in A., B., and C., respectively.

4.4 Discussion

In practice, the usual strategy to efficiently obtain the data in multidimensional NMR experiments is to highly truncate the indirect dimensions, and then apply LP to recover some of the lost resolution. If necessary, further resolution is obtained by adding dimensions to the experiments; however, the line widths are sacrificed in order to acquire a three- or four- dimensional spectrum within a reasonable amount of time. We performed the NUS version of the experiment by sampling 33% of the full set of data points experiment in two ways: by reconstructing the spectrum with the same number of scans, which means we only utilize one-third of the experimental time required for the spectra shown in Figure 4.10.B and 4.10.E (40 scans, 4 s recycle delay); and by reconstructing the spectrum with three times the number of scans which means we utilize the same amount of the experimental time but each data set has 1.7 times the signal-to-noise ratio shown in Figure 4.10.C and 4.10.F (120 scans, 4 s recycle delay). In both cases spectra with improved resolution were obtained.

CS was originally proposed to reconstruct sparse data. In NMR spectroscopy, sparse data most closely resemble solution NMR spectra, which have signals with relatively high signal-to-noise ratios and narrow line widths spread over a large frequency range. We investigated the performance of CS for solid-state NMR studies of proteins with broader line widths and a wide range of signal-to-noise ratios, which is challenging because the conditions are not ideal for CS, and the sizes of datasets available for processing are limited. To optimize the NUS scheme, knowledge of the line widths and signal-to-noise ratios of both conventional and reconstructed spectra are required. However, in most cases these can be quickly measured or estimated from preliminary

experiments on the same or similar samples. The results show that CS can provide reconstructions in two- and three- dimensional experiments using 25% - 33% sampling for spectra having signal-to-noise ratios ~ 10. The splitting artifacts are especially prominent in the low sensitivity and highly under-sampled experiments[137]. With these parameters the vast majority of signals are faithfully reproduced, although a few may be ambiguous following the reconstructions because of variations of the intensities. However, in terms of efficiency, only 25% - 33% of experimental time is required to obtain spectra with similar (or even higher) signal-to-noise ratios. In the future, wavelet transforms can be implemented [17], which transforms the spectral signals to the frequency domain and is advantageous for crowded spectra and solid-state NMR experiments associated strong spin interactions, such as dipolar coupling networks among like spins.

Using CS under optimized conditions it is possible to increase the efficiency, resolution, and signal-to-noise ratio of solid-state NMR spectra on stationary and spinning samples.

4.5 Experimental Methods

The generation of simulated FIDs, NUS schemes, and spectral reconstructions were performed with MATLAB (Mathworks, http://www.mathworks.com/) scripts. The IST algorithm is based on the pseudo-code proposed by Drori[18]. The direct dimension of the spectra was first processed with NMRpipe[151], and then, the indirect dimensions were reconstructed using the IST algorithm.

The two-dimensional NUS magic angle spinning solid-state NMR experiments were performed with a home-built $^{1}H/^{13}C/^{15}N$ triple resonance probe at 800 MHz $^{13}C/^{13}C$ correlation experiments utilized the dipolar assisted rotational resonance (DARR) pulse sequence[152] for mixing, and we also implemented the repetitive cross-polarization (REP-CP) contacts via equilibration-re-equilibration of the proton bath [153; 154] to improve $^{1}H/^{13}C$ magnetization transfer. A 60-residue truncated construct of a mercury transport protein, MerFt, [155] was incorporated into 14-O-PC proteoliposomes at pH=6. The protein to lipid molar ratio was 1:68, and the MAS rotors contained a total of ~2 mg protein. All the spectra were acquired with 20 ms mixing at 5°C and a spinning rate of 11,111 Hz.

Stationary sample solid-state NMR experiments were performed using a home-built $^{1}H/^{15}N$ double resonance probe on a Bruker Avance spectrometer (http://www.Bruker-Biospin.com) at a ^{1}H resonance frequency of 700 MHz Two-dimensional SLF and three-dimensional NUS HETCOR/SLF[150] experiments were performed with B_1 field strength of 50 kHz at 42 °C, and ^{1}H and ^{15}N carrier frequencies of 9 ppm and 100 ppm, respectively. 512 complex points were acquired with dwell time of 40 μs in the direct dimension. The sample consisted of 3 mg of the membrane-bound form of the uniformly ^{15}N-labeled 46-residue coat protein of bacteriophage Pf1 incorporated into q = 3.2 DMPC/DHPC bicelles[156] (q is the molar ratio of long chain to short chain lipids) .

Chapter 4, in full, is a reprint of the material “Sampling Scheme and Compressed Sensing Applied to Solid-State NMR Spectroscopy” as it appears in J. Magn. Reson. 237:40-48 by Lin EC, Opella SJ. The thesis author was the primary author of the paper.

Chapter 5 Covariance Spectroscopy in High-Resolution Multi-dimensional Solid-state NMR

5.1 Abstract

Covariance spectroscopy (COV), a statistical method that provides increased sensitivity, can be applied to two-dimensional high-resolution solid-state NMR experiments, such as homonuclear spin-exchange spectroscopy. We proposed the alternative States sampling scheme to the experimental time by 50%. By combining COV with other processing methods for non-uniform sampling (NUS), many different three-dimensional experiments can be performed with substantial increases in overall sensitivity. As an example, we show a three-dimensional homonuclear spin-exchange / separated-local-field (SLF) spectrum that enables the assignment of resonances and the measurement of structural restraints from a single experiment performed in a limited amount of time.

5.2 Introduction

There are many advantages to performing three- and higher dimensional experiments in NMR spectroscopy. This is an area that is well developed for high-resolution solution NMR, but has lagged somewhat for solid-state NMR, especially of proteins, largely because of the broader widths of single-line resonances and the complex

line shapes of powder patterns, and the generally lower signal-to-noise ratios of the spectra. For example, a three-dimensional combination of homonuclear spin-exchange and separated-local-field (SLF) spectroscopies can provide many distance and angular structural restraints, and full or partial resonance assignments in a single experiment[27; 82; 157; 158]. Therefore, it has the potential to accelerate and improve protein structure determination by solid-state NMR. However, using conventional uniform sampling (US) of the time domain signals in three dimensions, it often requires many days of signal averaging to perform. To reduce the total amount of time required to perform three- and higher-dimensional NMR experiments, several methods of processing US[126] and non-uniform sampled[15; 19; 40; 41; 43; 136; 159; 160] (NUS) signals have been proposed as replacements for conventional Fourier transformation of complete US free induction decays (FIDs). However, most of these methods require a minimal signal-to-noise ratio >10 for successful spectral reconstructions, and even this modest ratio may not be readily available for many of the protein samples of greatest interest. In addition, sparse data sets are typically required to avoid the introduction of spectral artifacts.

Here we describe applications of covariance (COV) spectroscopy to reconstruct spectra whose resonances have signal-to-noise ratios <10 and relatively broad linewidths. These include the use of sampling schemes based on the States method[161], which has the further benefit of reducing the time spent acquiring signals in half. We also demonstrate that it is possible to combine the NUS method of Compressed Sensing (CS)[15; 19] with COV to reconstruct a three-dimensional homonuclear spin-exchange/ separated-local-field spectrum with only 11.7% sampling compared to 100% US sampling without losing resolution, and with a diagonal in only one of the two-

dimensional spectral planes. The COV and CS processing were performed using Matlab (Mathworks, http://www.mathworks.com) scripts.

COV[22-24; 162; 163] is a statistical method that generates the indirect dimension according to the covariance of the direct dimension, saving the time required to acquire a full data set in the indirect dimension. The spectrum is generated according to Equation 5.1 [23]:

$$\mathbf{C}_{ij} = \frac{1}{N_1}\sum_{k=1}^{N_1}\Big(\mathbf{S}(k,i) - \big\langle\mathbf{S}(i)\big\rangle\Big)\Big(\mathbf{S}(k,j) - \big\langle\mathbf{S}(j)\big\rangle\Big) \qquad \text{Equation 5.1}$$

N_1 is the number of point in indirect dimension, S is the one-dimensional frequency spectrum at evolution time t_k for the indirect dimension, i and j are the indices of the frequencies, and the angle bracket of S is the average over time t_k at frequency ω_i. It has been shown that the covariance of a frequency pair represents the off-diagonal element in a two-dimensional Fourier transform spectrum[23; 24], and the variance of each frequency represents the diagonal element. The frequency evolutions in the t1 dimension are treated as trials to find correlations between signals. Some advantages are immediately apparent. The spectral width and the resolution of the indirect dimension are identical to those of the direct dimension, however they are independent of the dwell time and N_1 for isolated cross-peaks because the covariance matrix is symmetric and calculated from the data acquired in the direct dimension. Therefore, baseline and phase corrections, apodization, or other signal processing methods are not required in the t1 dimension. The noise level in the t1 dimension is only weakly dependent on N_1, and mostly determined by the data in the t2 dimension[162]. Consequently, high-resolution homonuclear correlation spectra can be obtained with a quite small value of N_1, as long

as N_1 is large, which can be verified 'on the fly'[164]. COV spectra can be obtained from either homo- or hetero-nuclear correlations, with the latter referred to as indirect covariance NMR spectroscopy[22].

We acquired the $^{15}N/^{15}N$ homonuclear spin-exchange spectrum of the 46-residue membrane-bound form of uniformly ^{15}N-labeled Pf1 coat proteins in macrodiscs, which consist of a phospholipid bilayer surrounded by a 'belt' protein[48]. Macrodiscs are large enough to magnetically align the protein-containing bilayers and to 'immobilize' the proteins in all directions while still enabling them to undergo rapid rotational diffusion about the bilayer normal. Both macrodiscs and bicelle samples have excess water present, therefore the proteins and lipids are fully hydrated. Moreover, macrodiscs possess the additional advantages over bicelles in that they are "detergent-free" and therefore have less potential to cause distortions of the protein structures [48]. Protein-containing bilayers aligned on glass plates also do not have detergent present, but are more difficult to keep fully hydrated due to heating from the radiofrequency irradiations.

5.3 Results and discussion

According to Equation 5.1, a homonuclear two-dimensional correlation spectrum can be obtained even when $N_1 = 1$; however, due to the absence of sufficient evolution for statistical verifications, the correlations will be incorrect. Similar situations (Figure 5.1.E and 5.1.H) are found for highly truncated sampling (Figure 5.1.B).

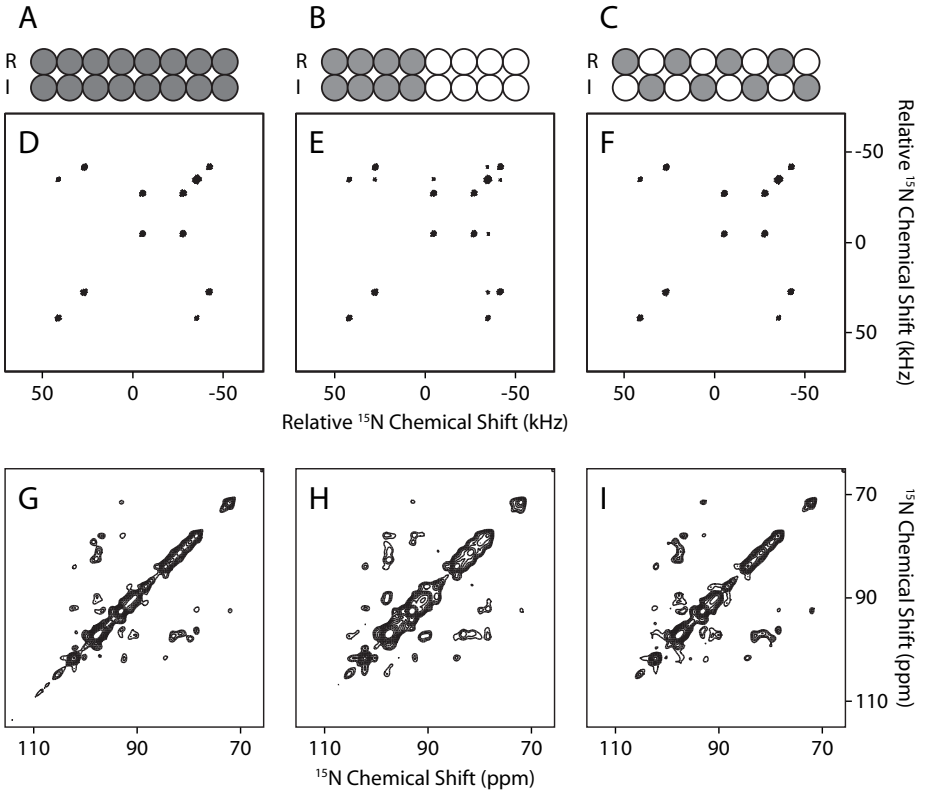

Figure 5.1 Sampling schemes, simulate spectra and experimental spectra of covariance NMR spectroscopy.

A., B., and C. are schematic diagrams of the sampling schemes. A. Conventional sampling. B. Highly truncated sampling. C. Alternative States sampling. D., E. and F are the simulated spectra generated from A., B. and C. sampling schemes, respectively. G., H., and I. are the ^{15}N/^{15}N homonuclear spin exchange spectra of the membrane-bound form of uniformly ^{15}N-labeled Pf1 coat protein in magnetically aligned (with the normal perpendicular to the field) macrodiscs, which are reconstructed by the sampling schemes, A. to C., respectively. R and I represent the real and imaginary points in the indirect dimension, and the filled and unfilled circles indicate the sampling and non-sampling points. 96 complex points were acquired in the regular covariance spectrum and 48 complex points were taken for demonstrating other sampling schemes (B and C). 3mg of ^{15}N-labeled Pf1 coat proteins were incorporated into 30mg DMPC (1,2- dimyristoyl-*sn*-glycero-3-phosphocholine) macrodiscs at pH 4.9[48]. The protein spectra were obtained by the conventional homonuclear PDSD (proton-driven spin diffusion) spin-exchange with a 3 sec mix time at 30°C, and the strength of B_1 field was 50 kHz. 1024 complex points were acquired with 20μs dwell time in the direct dimension, and 96 complex points were acquired with 100μs dwell time in the indirect dimension. The spectrum resulted from 500 scans of signal averaging for each time domain point. The experiments were performed on a Bruker Avance spectrometer with ^{1}H and ^{15}N frequencies of 699.70 and 70.90MHz by the home-built double-resonance MAGC probe.

To reduce the experimental time without building up incorrect correlations, we alternately sample real and imaginary parts of the signals (Figure 5.1.C) because when COV is applied with the States method, the sign does not rely on quadrature detection. In this way it is possible to both maintain spin evolution and reduce the experimental time by 50%. To demonstrate the idea, we randomly generated six ^{15}N resonances with different chemical shifts (23.4, -40.9, -34.6, -23.4, -7.7, 27.9 ppm), with 100 Hz line widths at a field strength corresponding to a 1H resonance frequency of 700 MHz. Notably, one pair of resonances is symmetric about the carrier frequency. We calculated 48 complex points with 100 μs dwell time in the indirect dimension as a conventional sampling scheme, and 24 complex points under the same conditions as an example of a highly truncated scheme. The signals were generated according to the alternative States sampling scheme. These simulated signals were processed with COV. Comparing to the covariance spectra with reasonable sampling points (Figure 5.1.D), the highly truncated sampling (Figure 5.1.E) results in artifacts due to the short evolutions. In contrast, the alternate (Figure 5.1.F) States sampling provides only the correct correlations.

The spectrum of the membrane-bound form of the uniformly ^{15}N labeled coat protein in aligned bilayers obtained with conventional sampling and processed by COV is shown in Figure 5.1.D. On larger membrane proteins, whose samples contain a smaller total amount of protein in the same volume, the sampling in the indirect dimension must be reduced in order to acquire the data for a two-dimensional spectrum with an adequate signal-to-noise ratio in a reasonable amount of time. The sensitivity enhancement by COV has been reported to be >20% when the dwell times of both dimensions are

identical[162; 163]. In our example, the signal-to-noise ratio resulting from COV is almost twice that from Fourier transformation. The dwell time in the direct dimension (20 μs) is smaller than that in the indirect dimension (100 μs), which results in the better sensitive in the frequency domain, and this benefit is brought to the indirect dimension via COV. In this spectrum, the average signal-to-noise ratio of the resonances obtained after Fourier transformation is <10. Notably, other NUS methods generally fail for spectra with such broad line widths and limited signal-to-noise ratios. We applied the alternative States sampling that also reduces the experimental time required to obtain the same signal-to-noise ratio. The result in Figure 5.1.I shows that it is possible to reconstruct the spectrum with a similar signal-to-noise ratio, while highly truncating sampling (Figure 5.1.H) already started to generate artifacts.

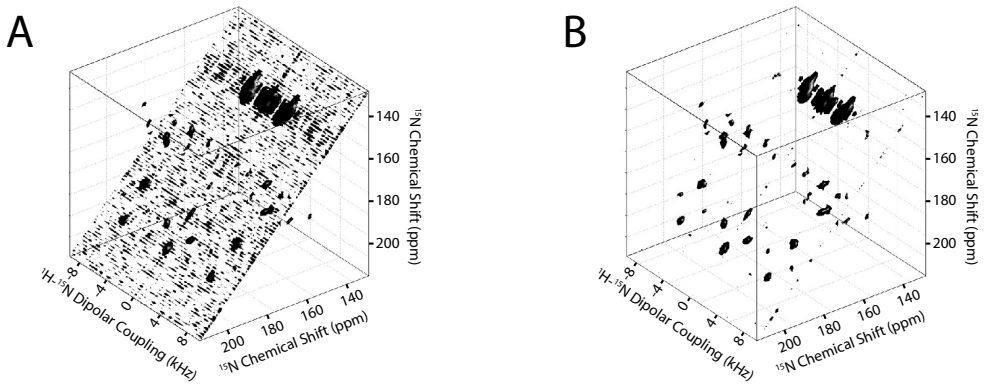

Figure 5.2 The reconstructions and signal processing of ^{1}H-^{15}N/^{15}N/^{15}N three-dimensional spectrum of a ^{15}N-labeled NAL single crystal.
A. The reconstructed ^{1}H-^{15}N/^{15}N/^{15}N three-dimensional spectrum of a ^{15}N-labeled NAL single crystal. B. The same spectrum without diagonal noise, which was removed by subtracting their average value. COV was applied to ^{15}N/^{15}N correlations for the reconstruction. 50 complex points were acquired using the alternate phase sampling scheme, which corresponds to 23.4% sampling, and the dipolar coupling dimension was reconstructed from 50% sampling (44 real points) by compressed sensing. The experiment was performed with 4 msec mix time under 38% MMHH conditions with a B_1 field of 52 kHz. The dwell time in the direct dimensions was 20 μs with 1024 complex points, and the dwell time in the t2 dimension was 100 μs. The spectrum resulted from 8 scans of signal averaging for each time domain point. The experiments were performed on a Bruker Avance spectrometer with ^{1}H and ^{15}N frequencies of 699.70 and 70.90MHz by the home-built double-resonance MAGC probe.

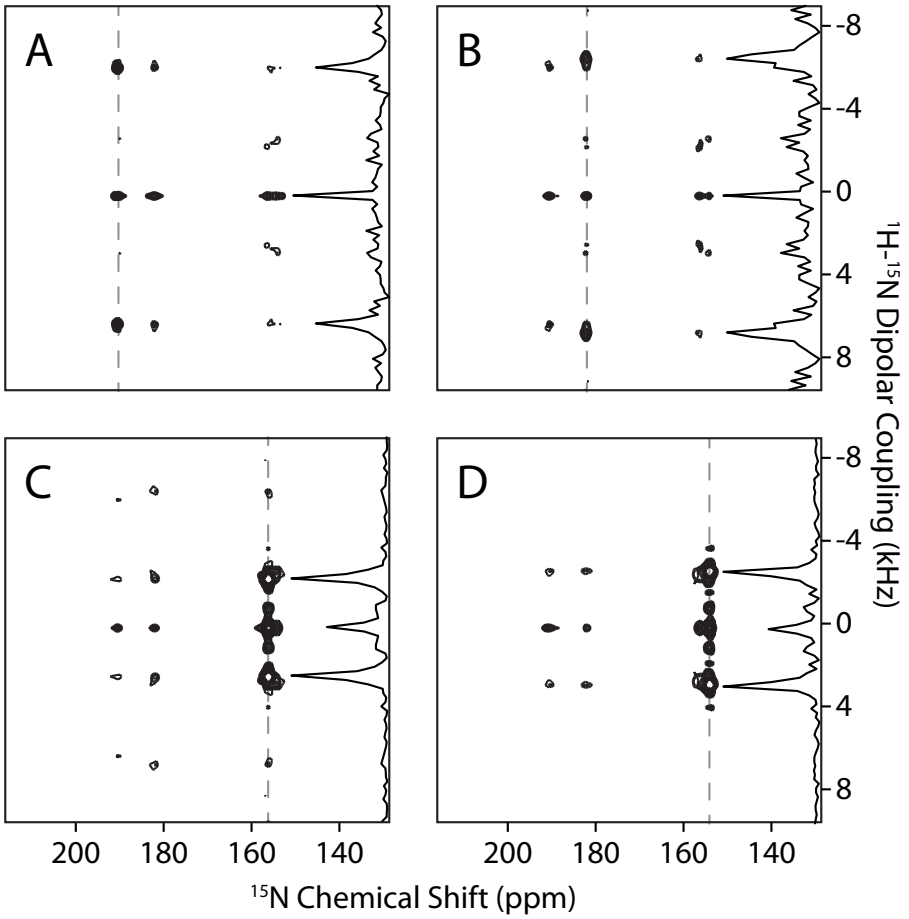

Figure 5.3 Spectral planes extracted from the there-dimensional spectrum of the resonances in ^{1}H-^{15}N/^{15}N/^{15}N three-dimensional spectrum of a ^{15}N-labeled NAL single crystal.
A. 192 ppm. B. 184 ppm. C. 157 ppm. D. 155 ppm. Artifacts generated in the SAMPI4 experiments for the small dipolar frequencies are found in low dipolar coupling regions (near 0 kHz) in C. and D. The signal-to-noise ratio of the lowest contour in each spectrum is 6. The dash lines in the spectra indicate the slices shown on the sides.

The tolerance of COV to low signal-to-noise ratios makes it feasible to accelerate the acquisition three-dimensional US/NUS spectra with low to moderate signal-to-noise ratios. We demonstrate this with a single crystal sample of ^{15}N N-acetyl leucine (NAL), which has four unique molecules in the unit cell, which results in four signals. The three-dimensional ^{15}N/^{15}N spin-exchange/^{1}H-^{15}N SLF experiment employs mismatched

Hartmann-Hahn (MMHH) spin diffusion for the homonuclear spin-exchange and SAMPI4 for measuring the heteronuclear dipolar couplings associated with individual chemical shift frequencies[165]. MMHH relies on the proton bath to assist spin-exchange among the dilute nuclei; therefore long-range correlations can be observed under this mechanism. Since the magnetizations tend to evenly distribute among the dilute spins via the proton bath, the magnetizations also have the opportunity to be deposited into other reservoirs of couplings, and it would make the spectra ambiguous for samples with weak signals[110; 166]. With this concern, we only applied MMHH to the single crystal spectrum, and applied a conventional homonuclear spin exchange (proton-driven spin diffusion, PDSD) to coat protein in bilayer samples. We reconstructed the ^{1}H-^{15}N dipolar coupling dimension and $^{15}N/^{15}N$ correlations by CS and COV, respectively, where the CS reconstructions are based on the NUS schemes that we previously optimized[160]. The reconstructed spectrum is shown in Figure 5.2.A, and the strong diagonal noise resulting from COV was readily removed by subtracting the average values (Figure 5.2.B)[167]. Spectral planes extracted from the three-dimensional spectrum for the four resonances are shown in Figure 5.3. They consist of doublets from the heteronuclear dipolar couplings associated with each of the resonances correlated via MMHH. 50% and 23.4% of points were sampled for the dipolar coupling and the indirect chemical shift dimensions, respectively, which results in 11.7% sampling compared to 100% US for the three-dimensional experiment. The line widths and line shapes of the resonances in the reconstructed spectral planes are comparable to those obtained from the corresponding two-dimensional experiments.

In conventional two-dimensional NMR[50; 52; 110; 168-170] approaches to structure determination, at least two separate experiments would be needed in order to make resonance assignments and measure structural restraints. By combining homonuclear spin exchange and SLF spectroscopies, the correlations and measurements of dipolar couplings and chemical shifts are obtained from a single spectrum. Moreover, the covariance spectra have intrinsically high-resolution and sensitivity, which makes this a general approach that can be incorporated into a variety of higher-dimensional experiments. The combination of benefits has the potential to substantially shorten the total amount of time spent performing experiments and signal averaging while improving the quality of structural restraints in structure determination of biopolymers by solid-state NMR. It is particularly applicable to membrane proteins studied by oriented sample (OS) solid-state NMR in stationary, aligned samples or in unoriented samples undergoing magic angle spinning.

Chapter 5, in full, is a reprint of the material “Covariance Spectroscopy in High-Resolution Multi-dimensional Solid-state NMR” as it appears in J. Magn. Reson. 239:57-60 by Lin EC, Opella SJ. The thesis author was the primary author of the paper.

Chapter 6 Structural determination of Vpu from HIV-1 by NMR in membrane environments

6.1 Abstract

Viral protein U (Vpu) from HIV-1, a small membrane protein composed of an α-helix in the transmembrane domain and two α-helices in the amphipathic cytoplasmic domain, downmodulates several cellular proteins, including, CD4, BST-2/CD317/tetherin, CCR7, and NTB-A. It interferes immune system, and enhances viral release. It is essential to characterize the structure and dynamics of Vpu in order to understand the mechanisms of protein-protein the interactions, and potentially to discover antiviral drugs. In this article, we describe the investigations of cytoplasmic domain of Vpu and full-length Vpu in several lipid environments by NMR spectroscopy. Results from constructs suggest that results from the two helices in the cytoplasmic domain form a U-shape, although the length of inter-helical loop in the cytoplasmic domain and the orientation of the third helix vary with the lipid composition. The C-terminal helix is relative flexible and provides accessibility for potential interaction partners.

6.2 Introduction

Viral protein U (Vpu) is one of the "accessory" proteins encoded by HIV-1. It is dispensable for viral replication *in vitro*; however, it appears to have multiple biological functions that are crucial for viral infectivity *in vivo*. Vpu removes newly synthesized CD4 receptors from the endoplasmic reticulum (ER), and causes subsequent degradation.

Thus, it prevents CD4 from binding to the viral envelope (Env) precursor, gp160, and as a result enhances viral infectivity[31; 34; 67]. Vpu also enhances the release of newly formed virus particles by antagonizing the human immune restriction factor BST-2/CD317 (tetherin), which otherwise prevents their release[33; 171; 172]. Recently Vpu has been shown to induce downmodulation of natural killer (NK) cell receptor NK, T-cell, B-cell antigen (NTB-A), and prevent HIV-Infected cells from degranulation and lyses by NK cells[68; 69]. Vpu is also found to downregulate the chemokine receptor CCR7 from the cell surface, and subsequently reduce the ability of $CD4^+$ T cells to migrate into the lymph nodes, where it helps with priming and assembly of immune responses[35].

Vpu is a small type I membrane protein, approximately 80-residues, which has two distinct domains, a hydrophobic transmembrane (TM) domain with helix-1 and an amphipathic cytoplasmic (Cyto) domain with helix-2 and helix-3. Loop-1 connects TM and Cyto domain and the loop-2 connects the two helices in the Cyto domain, and contains two conserved phosphorylation sites. These two domains are individually associated with the biological activities mentioned above that contribute to the pathogenicity of HIV-1 infection. Two constructs are discussed in the article: Cyto domain (28-81) of Vpu (VpuCyto), and full-length Vpu (VpuFull).

The interactions of Vpu with BST-2, NTB-A and CCR7 have been mapped to the TM domains of each pair of proteins, VpuTM is shown to employ the A10, A14, A18 and W22 helix face in the interactions by both biological and spectroscopic studies[35; 68; 173]. Also, the single site mutation of W22L is shown to inhibit the ability of Vpu to downregulate CD4[66]. Helix-2 in Vpu, which is in the cytoplasmic domain is required

for CD4 binding[174], the conserved DSGXXS phosphorylation site in loop-2 acts as a molecular adaptor to recruit β-TrCP, linking CD4 and/or BST-2 to the β-TrCP /SCF E3 ubiquitin ligase complex for degradation [31; 172; 175-180]. The tryptophan in the C-terminal helix of VpuCyto has been identified as a key residue to contribute to virus release enhancement, primarily due to the ability of Vpu to displace BST-2 from the virus assembly site[181; 182].

The structure of the TM domain of Vpu (VpuTM) has been well studied in various membrane systems including detergent micelles[183], lipid bicelles[184], lipid bilayers[65] by both solution and solid-state nuclear magnetic resonance (NMR) spectroscopy, whereas the Cyto domain has proven to be more difficult to study in large part because of its flexibility. Previously, the structure of Vpu39-81 from HIV strain HV1S1 has been studied in 50% TFE[185], aqueous solution[186] and DPC micelles[187] by solution NMR. Here, the structure and dynamics of VpuCyto from NL4-3 are characterized in both aqueous solution and isotropic DHPC micelles by circular dichroism (CD) spectroscopy, and solution NMR spectroscopy. The structure of VpuCyto in DHPC micelles is determined base on distance restraints obtained from paramagnetic relaxation enhancement (PRE) experiments and angular restraints obtained from residual dipolar coupling (RDC) measurements. In aqueous solution, VpuCyto is dynamically disordered; in contrasting DHPC micelles, it forms two helices in a U-shaped arrangement. Also, rotationally aligned (RA) solid-state NMR[1; 5; 8] experiments have been employed to study full-length Vpu in DMPC bilayers, which is a more biologically relevant membrane environment than micelles, and all the measurements are performed at 25 °C and pH 7.3, which are close to physiological

conditions. ^{15}N, ^{13}C chemical shift and ^{1}H-^{15}N, ^{1}H-^{13}C dipolar couplings were measured and converted to dihedral restraints and angular restraints for structure calculation. PRE effects were measured and used as additional distance restraints.

6.3 Materials and methods

6.3.1 Plasmids, Cells, and Reagents

Vpu expression plasmids for NL4-3 VpuFull and VpuCyto constructs were prepared similarly to those previously described[96; 188]. Synthesized DNA corresponding to VpuCyto (Integrated DNA Technologies) was ligated into phLV vector for expression as a Trp-leader fusion. Synthesized DNA for the VpuFull sequence was inserted into pET31b(+) vector (Agilent Technologies) for expression as a KSI fusion. For both constructs, the methionines were mutated to leucine to assist protein purification, and were shown to have no effect on the properties of Vpu. Expression plasmids encoding mutant VpuCyto-L41C, VpuCyto-A74C and VpuFull-L41C were constructed using the QuikChange Lightning Site-Directed Mutagenesis Kit (Agilent Technologies), and the primers were synthesized by Integrated DNA Technologies. BL21-CodonPlus competent cells were obtained from Agilent, and Overexpress C41(DE3) competent cells were obtained from Lucigen.

The chelated manganese was prepared by adding manganese sulfate ($MnSO_4$) to ethylenediaminetetraacetic acid (EDTA) (0.5 M) as a 2:1 molar ratio in 20mM HEPES pH 7.3 buffer, and a MnEDTA precipitate was formed overnight. The precipitated complex was centrifuged, washed with water and methanol, and dried by lyophilization.

The lipids 1,2-dihexanoyl-sn-glycero-3-phosphocholine (DHPC) and 1,2-dimyristoyl-sn-glycero-3-phosphocholine (DMPC) were purchased from Avanti Polar Lipids, Inc. S-(1-oxyl-2,2,5,5-tetramethyl-2,5-dihydro-1H-pyrrol-3-yl)methyl methanesulfonothioate (MTSL), 5-DOXYL-stearic acid, free radical (5DSA), ascorbic acid and deuterium oxide (D_2O) were obtained from Sigma. ^{13}C-glucose and $(^{15}NH_4)_2SO_4$ were obtained from Cambridge Isotope Laboratories. TrisHCl buffer were obtained from Teknova, Inc. Dithiothreitol (DTT) and HEPES buffer were purchased from Invitrogen Corporation.

6.3.2 Protein Expression

The expression and purification of VpuFull, VpuCyto and mutants were performed similarly to the methods described previously[96; 188]. Briefly, the proteins were overexpressed in BL21-CodonPlus competent cells and Overexpress C41 (DE3) competent cells, respectively for VpuCyto and VpuFull in LB or minimal M9 growth media with $(^{15}NH_4)_2SO_4$ and/or ^{13}C-glucose for preparation of unlabeled or isotopically labeled samples. The proteins were isolated using nickel affinity chromatography, and then separated from the fusion partner by cyanogen bromide cleavage, followed by reverse phase high performance liquid chromatography (HPLC) for final purification. The molecular weight of the purified protein was confirmed to be correct using SDS-PAGE and Matrix-assisted laser desorption/ionization *(*MALDI) mass spectrometry. Milligram amounts of the isotopically labeled protein were obtained for the NMR experiments.

6.3.3 Sample Preparation

Protein samples for solution NMR were prepared by dissolving purified and lyophilized VpuCyto protein powder in either aqueous solution with 10%(V/V) D_2O with the pH adjusted to 3.0, or aqueous solution containing 100 mM DHPC with 10% (v/v) D_2O with the pH adjusted to 4.0. For RDC measurements, DHPC containing VpuCyto was weakly aligned in vertically stretched 6% polyacrylamide gels, as previously described[189]. Proteoliposome samples for solid-state MAS experiments were prepared by first mixing purified lyophilized Vpu powder with DMPC powder (1:3.5 mass ratio) and dissolving in 10% SDS buffer to obtain a clear solution with 10mg/mL DMPC concentration. Then the sample was diluted 20-fold, and incubated at room temperature for 4 hours. Subsequently, SDS was removed from the solution by first dialysis against 20mM HEPES, pH 7.3 buffer overnight, and then 5 days dialysis against 20 mM KCl in 20 mM HEPES, pH 7.3. After dialysis, the proteoliposomes were collected by ultracentrifugation at 235,000 ×g for overnight at 15 °C. The concentrated proteoliposome sample was packed into a 3.2 mm MAS rotor for solid-state NMR experiments.

To measure PRE, the cysteines in each of the mutants were covalently linked to (1-oxyl-2,2,5,5-tetramethyl-3-pyrroline-3-methyl) methanesulfonate (MTSL) using the following protocol[190]. Purified, lyophilized mutant protein powder was dissolved in 8 M urea in 20 mM TrisHCl, pH 8.0 with 20-fold molar excess of dithiothreitol (DTT) and incubated for 2 hours. Then the protein solution was run over a G10 desalting column pre-equilibrated with urea buffer to remove DTT. A 10-fold excess of MTSL dissolved in acetonitrile was added to the reduced protein, and the mixture was incubated in the dark

at room temperature overnight. Free MTSL was separated from MTSL-labeled protein by passing the sample through a G10 desalting column followed by dialyzed against water for a day. The protein precipitated during dialysis, and the MTSL-labeled protein was obtained by lyophilization. For solution NMR measurements, MTSL-labeled protein was refolded in 100 mM DHPC micelles with a final protein concentration of ~0.1 mM. For MAS experiments, MTSL-labeled protein was reconstituted into proteoliposomes with DMPC, as previously described. MTSL-labeled protein was reduced by addition a 10-fold excess of ascorbic acid in either micelles or liposomes. 5SDA and/or MnEDTA were incorporated into either VpuCyto in 100 mM DHPC or VpuFull in DMPC proteolipsomes to a final concentration of 0.5 mM for 5SDA and 1 mM for MnEDTA respectively.

6.3.4 NMR Spectroscopy and Data Processing

The solution NMR experiments were performed on a Bruker AVANCE 600 MHz and a Varian 800MHz spectrometers equipped with a 5 mm z-axis pulse-field gradient and $^{1}H/^{15}N/^{13}C$ triple resonance cryoprobes. All of the experiments were performed at 50 °C. ^{1}H-^{15}N HSQC experiments were acquired with 2048 and 256 points in the direct and indirect dimensions, respectively. Triple resonance HNCA, HNCACB, HN(CO)CA and HNCO experiments were performed on uniformly ^{13}C and ^{15}N labeled protein for the backbone amide resonance assignments. The side-chain assignments were completed using HCC(CO)NH, CC(CO)NH and TOCSY-HSQC experiments. ^{1}H chemical shifts were referenced to the H_2O resonance frequency at 50 °C, ^{13}C chemical shifts were referenced to TPS, and ^{15}N chemical shift were referenced to AMS. ^{15}N-edited NOESY-

HSQC (mixing time, 120 ms) and ^{13}C-edited NOESY-HSQC (mixing time, 120 ms) experiments were performed to collect distance restraints. ^{15}N T_1 measurements were recorded with relaxation delays of 20, 220, 420, 620, 820, 1020, 1320, and 1520 ms.^{15}N T_2 measurements were recorded with relaxation delays of 10, 30, 50, 70, 90, 130, and 170 ms. Both T_1 and T_2 relaxation time were fitted and calculated using SPARKY (T. D. Goddard and D. G. Kneller, SPARKY 3, University of California, San Francisco). Heteronuclear ^{1}H-^{15}N NOEs were obtained using a gradient sensitivity enhanced ^{1}H-^{15}N NOE experiment, recorded with and without ^{1}H saturation after a relaxation delay of 4 s. The heteronuclear NOE values for each residue were calculated by comparing the peak intensities of cross-peaks in the presence and absence of ^{1}H saturation. RDCs were measured with HSQC in-phase and anti-phase (IPAP) experiments.

For solid-state MAS experiments, ^{13}C-detected cross polarization (CP) spectra were acquired with MAS spinning speed of 5,000 Hz from 5 °C to 30 °C to determine the minimum temperature that allows VpuFull to undergo fast rotational diffusion about the bilayer normal, ^{13}C/^{13}C correlations were obtained with proton-driven spin diffusion (PDSD)[191] and dipolar-assisted rotational resonance (DARR)[152; 192] mixings, and ^{13}C/^{15}N transfer were obtained with SPECIFIC-CP[193]. The ^{15}N and ^{13}Cα chemical shifts were assigned with 3D NCACX and NCOCX experiments. The ^{1}H-^{13}C and ^{1}H-^{15}N dipolar couplings were assigned base on a combination of assigned chemical shifts and 3D SLF experiments including ^{1}H-^{13}C/N/Cα and ^{1}H-^{15}N/N/Cα, where $R18^{7}_{1}$ pulse sequences[194] were implemented to acquire heteronuclear dipolar couplings. All the experiments were performed at 700 MHz home-built triple-resonance MAS probe with Bruker Advance console. The details of solid-state NMR experiments are listed in Table

6.1. All of the NMR data were processed using NMRPipe[151] and analyzed with Sparky. All of the figures were prepared using Sparky. The resonance intensities and chemical shifts were extracted using Sparky.

Table 6.1 The details of solid-state NMR experiments[a].

Two-dimensional $^{13}C/^{13}C$ correlation	
PDSD / DARR Mixing time [ms]	50 / 200
Acquisition time (t1 / t2) [ms]	2.6 / 12.9
Carrier frequency (t1 / t2) [ppm]	40 / 100
$\pi/2$ pulse (^{1}H / ^{13}C) [μs]	5 / 2.7
CP contact time [μs]	400
CP pulse shape (^{1}H)	Linear (100-50%)
CP rf field strength (^{1}H / ^{13}C) [kHz]	70 / 100
^{1}H decoupling field strength (sw-TPPM) [kHz]	100
Recycle delay (s) / number of acquisitions	2 / 1280, 3840 (PRE)
Spectral width (F1 / F2) [kHz]	12.32 / 39.68

Two-dimensional $^{15}N/^{13}C\alpha$ correlation	
Acquisition time (t1 / t2) [ms]	8.5 / 10.2
Carrier frequency (t1 / t2) [ppm]	120 / 100
$\pi/2$ pulse (^{1}H / ^{13}C) [μs]	5 / 2.7
CP contact time ($^{1}H/^{15}N$) [μs]	1000
CP pulse shape (^{1}H)	Linear (100-50%)
CP rf field strength (^{1}H / ^{15}N) [kHz]	75 / 43
SPECIFIC-CP contact time (^{15}N / ^{13}C) [μs]	4000
SPECIFIC-CP pulse shape (^{13}C)	Linear (100-90%)
SPECIFIC-CP rf field strength (^{15}N / ^{13}C) [kHz]	43 / 33
^{1}H decoupling field strength (sw-TPPM) [kHz]	100
Recycle delay (s) / number of acquisitions	2 / 2624
Spectral width (F1 / F2) [kHz]	2.84 / 50

Two-dimensional ^{1}H-$^{13}C/^{13}C\alpha$ SLF	
Acquisition time (t1 / t2) [ms]	5.28 / 10.24
Carrier frequency (^{1}H / ^{13}C) [ppm]	8 / 100
$\pi/2$ pulse (^{1}H / ^{13}C) [μs]	2.7 / 5
CP contact time [μs]	400
CP pulse shape (^{1}H)	Linear (100-50%)
CP rf field strength (^{1}H / ^{13}C) [kHz]	70 / 100
$R18^{7}_{1}$ pulse length [μs]	5
^{1}H decoupling field strength (sw-TPPM) [kHz]	100
Recycle delay (s) / number of acquisitions	2 / 512
Spectral width (F1 / F2) [kHz]	30.03 / 100

Table 6.1 The details of solid-state NMR experiments, Continued.

Two-dimensional ^{1}H-$^{15}N/^{13}C\alpha$ SLF	
Acquisition time (t1 / t2) [ms]	1.2 / 10.24
Carrier frequency (^{1}H / ^{13}C / ^{15}N) [ppm]	8 / 100 / 120
$\pi/2$ pulse (^{1}H / ^{13}C / ^{15}N) [μs]	2.7 / 5 / 5.8
CP contact time ($^{1}H/^{15}N$) [μs]	1000
CP pulse shape (^{1}H)	Linear (100-50%)
CP rf field strength (^{1}H / ^{15}N) [kHz]	75 / 43
SPECIFIC-CP contact time ($^{15}N/^{13}C$) [μs]	4000
SPECIFIC-CP pulse shape (^{13}C)	Linear (100-90%)
SPECIFIC-CP rf field strength (^{15}N / ^{13}C) [kHz]	43 / 33
$R18^{7}_{1}$ pulse length [μs]	5
^{1}H decoupling field strength (sw-TPPM) [kHz]	100
Recycle delay (s) / number of acquisitions	2 / 1216
Spectral width (F1 / F2 / F3) [kHz]	10 / 50

Two-dimensional TOBSY $^{13}C/^{13}C$ correlation	
Acquisition time (t1 / t2) [ms]	9.5 / 20.48
Carrier frequency (t1 / t2) [ppm]	80 / 80
$\pi/2$ pulse (^{1}H / ^{13}C) [μs]	2.7 / 5
J-evolution period for $^{1}H/^{13}C$ transfer and refocusing [ms]	1
Adiabatic pulse shape / pulse length	tanh tan / 90
TOBSY mixing period [ms]	11.34
^{1}H decoupling field strength (sw-TPPM) [kHz]	50
Recycle delay (s) / number of acquisitions	2 / 64
Spectral width (F1 / F2) [kHz]	26.32 / 50

Three-dimensional assignments	$^{15}N/^{13}C\alpha/^{13}C$	$^{15}N/^{13}C'/^{13}C$
Acquisition time (t1 / t2 / t3) [ms]	1.51 / 2.82 / 10.2	1.11 / 8.5 / 10.2
Carrier frequency (t1 / t2 / t3) [ppm]	120 / 55 / 100	120 / 175 / 100
$\pi/2$ pulse (^{1}H / ^{13}C / ^{15}N) [μs]	2.7 / 5 / 5.8	2.7 / 5 / 5.8
CP contact time ($^{1}H/^{15}N$) [μs]	1000	1000
CP pulse shape (^{1}H)	Linear (100-50%)	Linear (100-50%)
CP rf field strength (^{1}H / ^{15}N) [kHz]	75 / 43	75 / 43
SPECIFIC-CP contact time ($^{15}N/^{13}C$) [μs]	4000	4000
SPECIFIC-CP pulse shape (^{13}C)	Linear (100-90%)	Linear (100-90%)
SPECIFIC-CP rf field strength (^{15}N / ^{13}C) [kHz]	43 / 33	43 / 33
^{1}H decoupling field strength (sw-TPPM) [kHz]	100	100
DARR mixing time [ms]	20	20
Recycle delay (s) / number of acquisitions	2 / 240	2 / 480
Spectral width (F1 / F2 / F3) [kHz]	5.67 / 10.56 / 50	5.67 / 10.56 / 50

Table 6.1 The details of solid-state NMR experiments, Continued.

Three-dimensional SLF	^{1}H-^{15}N/^{15}N/$^{13}C\alpha$	^{1}H-^{13}C/^{15}N/$^{13}C\alpha$
Acquisition time (t1 / t2 / t3) [ms]	2.21 / 8.5 / 10.2	1.11 / 8.5 / 10.2
Carrier frequency (^{1}H / ^{13}C / ^{15}N) [ppm]	8 / 100 / 120	8 / 100 / 120
$\pi/2$ pulse (^{1}H / ^{13}C / ^{15}N) [μs]	2.7 / 5 / 5.8	2.7 / 5 / 5.8
CP contact time (^{1}H/^{15}N) [μs]	1000	1000
CP pulse shape (^{1}H)	Linear (100-50%)	Linear (100-50%)
CP rf field strength (^{1}H / ^{15}N) [kHz]	75 / 43	75 / 43
SPECIFIC-CP contact time (^{15}N/^{13}C) [μs]	4000	4000
SPECIFIC-CP pulse shape (^{13}C)	Linear (100-90%)	Linear (100-90%)
SPECIFIC-CP rf field strength (^{15}N / ^{13}C) [kHz]	43 / 33	43 / 33
$R18^{7}_{1}$ pulse length [μs]	5	5
^{1}H decoupling field strength (sw-TPPM) [kHz]	100	100
Recycle delay (s) / number of acquisitions	2 / 576	2 / 512
Spectral width (F1 / F2 / F3) [kHz]	10.01 / 2.5 / 39.68	30.03 / 2.5 / 39.68

[a]All the experiments were acquired with 10,000 Hz of spinning rate, at 25 °C. Abbreviations used in the table: CP, cross-polarization; PDSD, proton driven spin diffusion; DARR, dipolar assisted rotational resonance; sw-TPPM, frequency-swift two-pulse phased-modulated; SPECIFIC-CP, spectrally induced filtering in combination with CP; TOBSY, through-bond correlation spectroscopy.

6.3.5 CD Measurement

The secondary structures of VpuCyto in aqueous media and DHPC micelles were analyzed by CD spectroscopy in the far UV (176–260 nm) region. Lyophilized protein was dissolved in either H_2O or 100mM DHPC to a final concentration of 1 mg/mL to obtain the spectra. Samples were transferred to a 0.1 mm path-length cell for data collection. (NSG Precision Cells, Inc., Farmingdale, NY) Data were collected on an AVIV model 2.98 at 25 °C, in 1.0 nm wavelength interval. Data was analyzed using an online server DichroWeb[195; 196].

6.3.6 Structure Calculation

Structure calculations for VpuCyto in DHPC micelles were carried out using Xplor-NIH[16] *ab initio* simulated annealing protocol with two steps: (1) high temperature simulated annealing, and (2) refinement. The initial structures were

generated from a extended random coil base on dihedral angle restraints derived from TALOS+[197] and distance restraints derived from the NOE cross-peaks in the simulated annealing. Residual dipolar couplings as angular restraints and paramagnetic relaxation data as distance restraints were incorporated during the refinement step. Simulated annealing was performed with a starting temperature of 3500 K and cooling to 25 K in steps of 12.5 K. kdih = 400 kcal mol^{-1} rad^{-2}. Knoe was rampped from 2 to 50 kcal mol^{-1} $Å^{-2}$. The refinement was performed with Xplor-NIH torsion angle molecular dynamics and experimental restraints included. The temperature was cooled to 50 K from an initial value of 2000 K in steps of 12.5 K. kdih = 400 kcal mol^{-1} rad^{-2}, knoe = 40 kcal mol^{-1} A^{-2}, krdc was ramped from 0.2 to 2 kacal mol^{-1} rad^{-2}. A total of 100 structures were generated in the refinement step, and the 20 structures with lowest-energy were used for analysis. For structure calculation of VpuFull in proteoliposome, a three-step process was employed, and the lowest structures were chose as the initial structure for refinement in the following step. Dipolar couplings and torsion angle were used in the initial determination, and distance restraints between the residues and the plane distance restraints[198] were added into the second and third steps, sequentially, where kdih = 400 kcal mol^{-1} rad^{-2}, ^{1}H-^{15}N krdc was ramped from 0.01 to 2 kacal mol^{-1} rad^{-2}, and ^{1}H-^{13}C krdc was ramped from 0.01 to 1 kacal mol^{-1} rad^{-2}, know was rampped from 2 to 40 kcal mol^{-1} $Å^{-2}$, kplane was rampped from 0.01 to 5 kcal mol^{-1} $Å^{-2}$.

6.4 Results and discussion

Both uniformly ^{15}N-labeled VpuCyto and VpuFull were reconstituted into 100mM DHPC micelles. Well-resolved, fully assigned ^{1}H-^{15}N HSQC NMR spectra were obtained for both polypeptides (Figure 6.1.B and 6.1.C). The two spectra overlap to a great extent, indicating that the structure of VpuCyto construct is representative of the cytoplasmic domain of full-length Vpu.

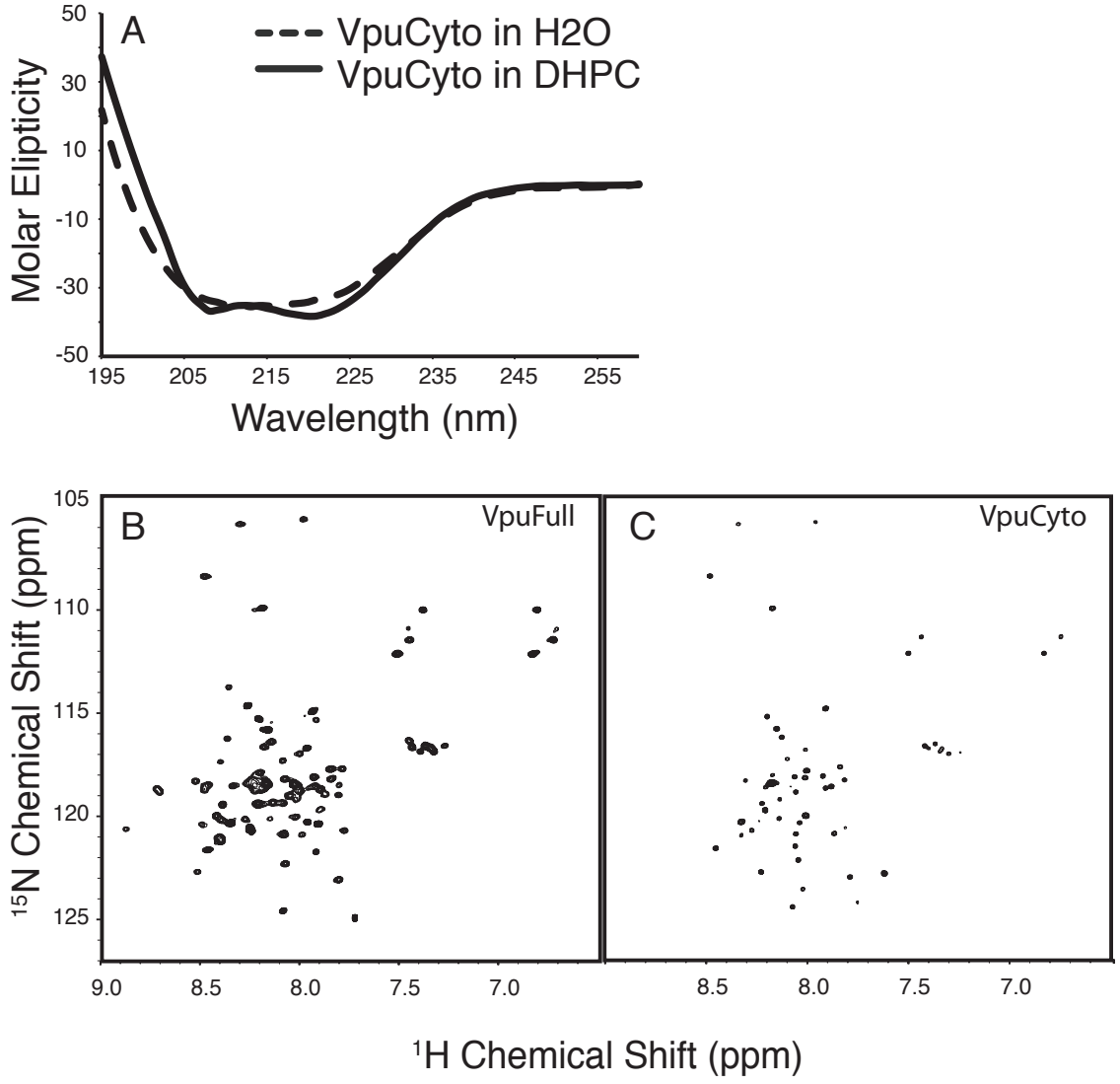

Figure 6.1 Secondary and tertiary structure analysis of VpuCyto.
A. Comparison of CD spectra of VpuCyto in aqueous media (dashed line) and 100 mM DHPC micelles (solid line). B. $^{1}H/^{15}N$ HSQC spectrum of VpuFull in 100 mM DHPC micelles. C. $^{1}H/^{15}N$ HSQC spectrum of VpuCyto in 100 mM DHPC micelles.

6.4.1 Secondary structure and dynamics of VpuCyto in aqueous media and DHPC micelles

The secondary structure features of VpuCyto in aqueous solution and DHPC micelles were determined by CD and NMR spectroscopy. The CD spectrum of VpuCyto in aqueous media (Figure 6.1.A) shows 37.5% helical content, 10.2% strand content, 22% turns and 31% disordered region. In DHPC micelles, VpuCyto was estimated to be 81.8% helix and 12.7% disordered. Based on the CD data, VpuCyto appears to be 44.3% more helical in the presence of DHPC micelles. This indicates that the cytoplasmic domain is affected by the lipid environment, and not freely soluble in the aqueous environment.

The secondary structure of VpuCyto in both conditions can also be confirmed by solution NMR experiments as well. VpuCyto in aqueous solution showed a relatively short T_1 (from 690 ms to 1000 ms) and long T_2 (from 210 ms to 600 ms), indicating that the protein is undergoing rapid reorientation, and the backbone is highly mobile. Also the negative ^{1}H-^{15}N heteronulcear NOE value throughout the protein sequence suggests that the internal motions of VpuCyto in aqueous media are fast. However, T_1, T_2 and NOE showed non-uniform distribution, where the terminal and inter-helical loop region (51-58) have longer T_1, longer T_2 and more negative ^{1}H-^{15}N heteronulcear NOE than the helical regions. The variation in T_1, T_2 and ^{1}H-^{15}N heteronuclear NOE agrees with CD data, suggests that there is a structural distinction between the helical regions and loop region in aqueous media, and the structure is not fully disordered. In contrast, the Cα chemical shift index has values around +1 ppm, which cannot be categorized as helix. In addition, TALOS+ only predict residue 62-70 as helix, and failed to predict any secondary structure for the rest of the protein due to the low order parameters. VpuCyto

may be in an intermediate state between well structured and fully disordered, with the helix-3 somewhat more structured.

In DHPC micelles, plots of the relative intensity of resonances peaks in the HSQC spectrum, and the Cα chemical shift index (Figure 6.2.G and 6.2.H) indicate two distinct helical religions connected by a mobile inter-helical loop. These helical regions are also consistent with the RDC data acquired in a 6% polyacrylamide stretched gel. While incorporated into DHPC micelles, with the increase of the protein-micelles complex size, the mobility is drastically lowered as shown by the significant decrease of T_2 relaxation (70 ms to 170 ms). In addition, same trends were observed for T_1, T_2 and ^{1}H-^{15}N heteronuclear NOE, suggesting a significant dynamic difference between the helical regions and the loop region. Overall, helices helix-3 and helix-2 exhibit similar restricted backbone dynamics, with similar values of ^{1}H-^{15}N heteronuclear NOEs, order parameters and ^{1}H-^{15}N HSQC peak intensities, in DHPC micelles. While residues at the N-, C-terminus and loop are significantly more flexible, with smaller values of the ^{1}H-^{15}N NOE and greater peak intensities.

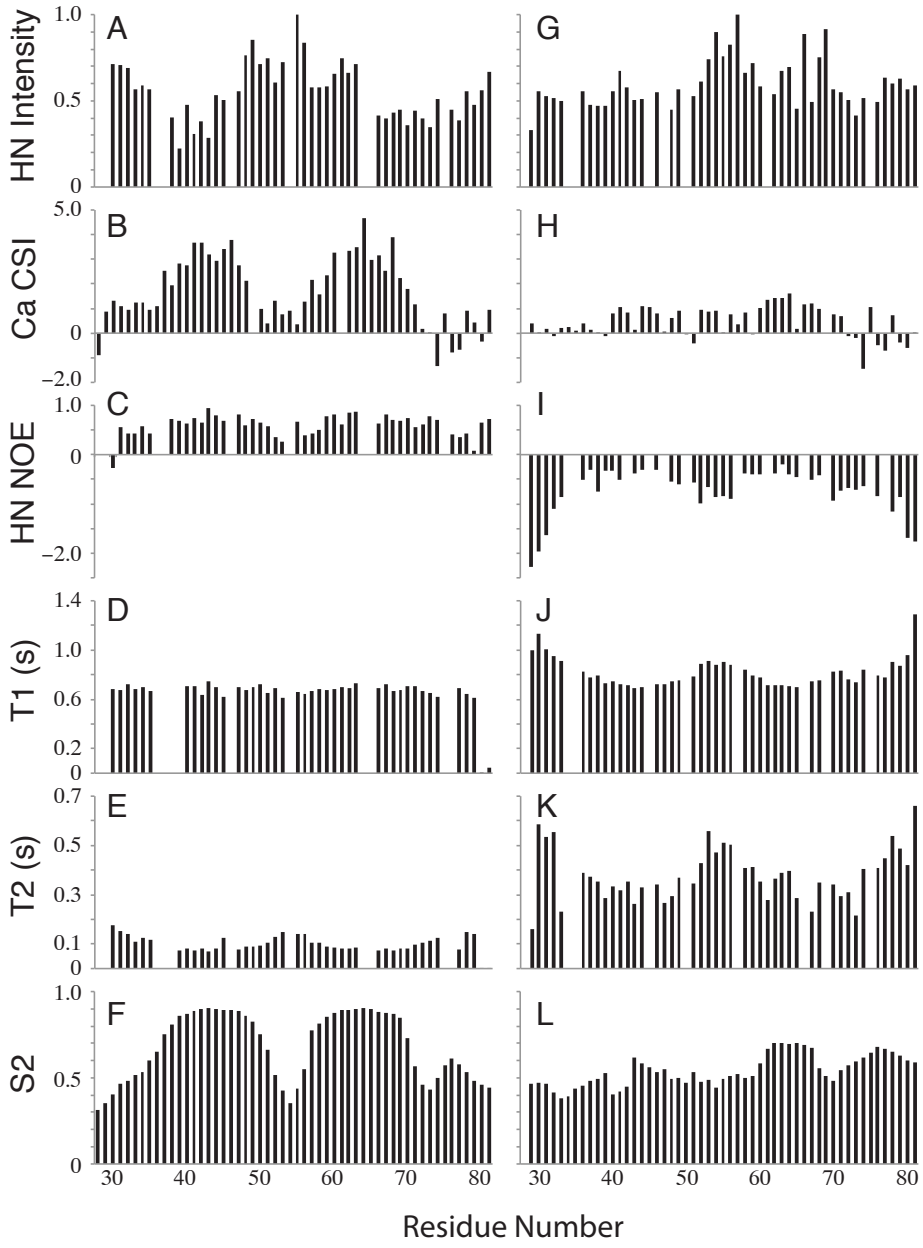

Figure 6.2 Secondary structure and dynamics of VpuCyto in aqueous and DHPC micelles.
A. $^{1}H/^{15}N$ HSQC resonance intensity plot. B. Cα chemical shift index. C. ^{1}H-^{15}N heteronuclear NOE. D. T_1 relaxation. E T_2 relaxation. F. order parameters derived from TALOS+. G. ^{1}H-^{15}N HSQC resonance intensity plot. H. Cα chemical shift index. I. ^{1}H-^{1}N heteronuclear NOE. J. T_1 relaxation. K. T_2 relaxation. L. order parameters derived from TALOS+. A.-F. are obtained from VpuCyto in H_2O. G.-L. are obtained from VpuCyto in 100 mM DHPC micelles.

6.4.2 Orientation restraints of VpuCyto derived from RDC measurements

Residual dipolar coupling measurements not only provide reliable information on the secondary structure of the protein, but also relative orientations of the helical regions in the protein. As shown in Figure 6.3.A, residues in both N- and C-terminal and the loop regions have close to 0 Hz RDCs, which is an indication of the mobile properties of these regions. The RDC values of the helical region were fit by two separate dipolar waves with very different amplitude, indicating a considerable angle difference between the helices. These RDC values can be used as angular restraints in structure calculation[199].

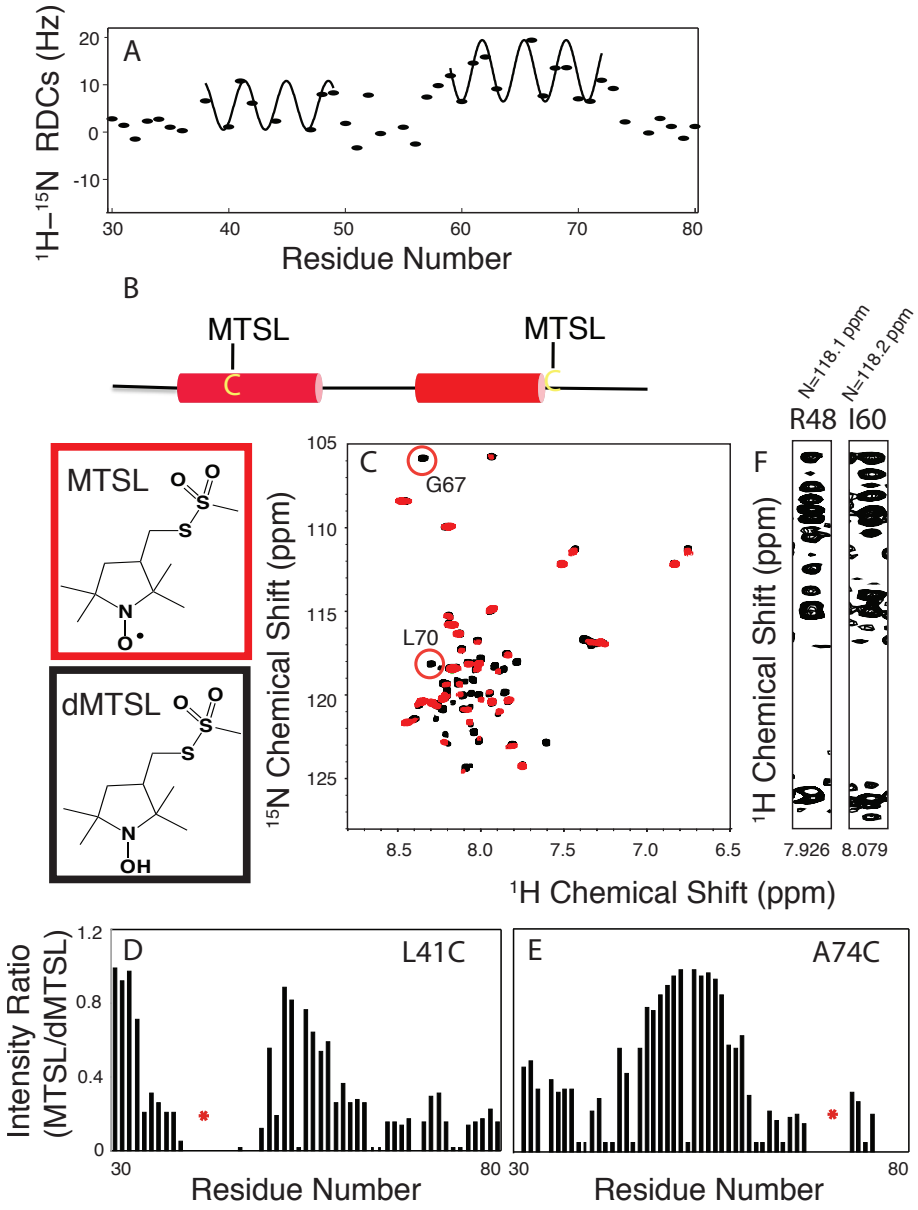

Figure 6.3 NMR measurements for structure calculation of VpuCyto in DHPC micelles. A. Residual dipolar couplings obtained from weakly aligned sample in 6% polyacrylamide stretch gel. B. A cartoon showing the location in secondary structure of VpuCyto where residues are mutated to cysteines and attached to MTSL, and the chemical structure of MTSL (red box) and its reduced form (black box). C. Overlap ^{1}H-^{15}N HSQC spectra of L41C VpuCyto with MTSL label (red) and its reduced diamagnetic label (black). D. Intensity plot shows PRE intenisty ration (I_{para}/I_{dia}) for L41C VpuCyto. E. Intensity plot shows PRE intenisty ration (I_{para}/I_{dia}) for A74C VpuCyto. F. Strip plots from 3D ^{15}N-edited HSQC-NOESY experiment showing long-range ^{1}H-^{1}H NOE between R48 and I60.

6.4.3 Distance restraints of VpuCyto derived from PRE measurements

PRE provides an alternative source of long-range distance restraints for structure determination of helical membrane protein, which usually lack "long-range" ^{1}H-^{1}H NOE in micelles environment. For PRE measurements, first a paramagnetic probe is incorporated into the protein. Then the coupling of the electron to the nuclear spins contributes to the relaxation of the nuclear spin, which is inversely proportional to the distance between the electron and nuclear spin. MTSL is a widely used nitroxide spin label. It is covalently attached to the thio group of cysteine residue in the protein. The secondary structure and motion information were considered before determining the optimal place for spin labels throughout VpuCyto. Residues at three positions 41, 62 and 74 locate at helix-2, helix-3 and the C-terminal region respectively were mutated to cysteine independently for MTSL attachment. ^{1}H-^{15}N HSQC spectra were collected on samples containing L41C-MTSL VpuCyto, S61C-MTSL VpuCyto and A74C-MTSL VpuCyto. In both of the L41C and A74C HSQC spectra, only residues near the mutation site showed small chemical shift changes compare to wild type spectra, which indicates that the mutation and the spin label did not change the protein structure dramatically. The S61C sample showed quite significant changes, so it was discarded for PRE measurement. The ^{1}H-^{15}N HSQC spectra (Figure 6.3.C) illustrate the overlapped spectra of the L41C-MTSL VpuCyto in red and it's reduced in black. Residues close to the mutation sites L41C were broadened deyond detection. Observable reductions in intensity due to PRE were also observed for residue 67, 70, even they were not close to L41C in the sequence, which indicates they are close to L41 in the tertiary fold of the

structure. The normalized PRE intensity ratio versus residue number for L41C VpuCyto and A74C VpuCyto are plotted (Figure 6.3.D and 6.3.E), and it is obvious that when the spin label is added to L41C, not only residues near 41, but also those at helix-3 and near C-terminus were broadened. Similarly, for MTSL-A74C, not only the residues in C-terminal region were broadened, the intensities of residues at the helix-2 were also significantly reduced. To ensure that the PRE effect is not intermolecular instead of intramolecular, protein concentration were limited to 0.1 mM during data acquisition; additionally, the intensity plot did not change significantly upon addition of unlabeled VpuCyto sample to the MTSL labeled sample, indicating that no internuclear PRE effect were observed in the first place.

The MTSL samples provided 72 PRE restraints that were particularly useful in defining distances and orientations between helix-2 and helix-3 in VpuCyto. Distance restraints were calculated base on the measured peak intensity ratios (I_{para}/I_{dia}) as described by Wagner[190] and Liang[200], and only intensity ratios in the range of 15% to 85% were selected for distance measurement. The global correlation time of each residue (5 ns - 10 ns) was calculated based on T_1 and T_2 of the wild type VpuCyto in micelles[201; 202]. The calculated PRE distances were incorporated into the structure calculations with a lower bound of 4 Å and upper bound of 4 Å as compensation for the inaccuracy in correlation time and other measurements.

6.4.4 VpuCyto backbone structure in DHPC micelles

During the structure calculation of VpuCyto in DHPC micelles, torsion angle restraints were obtained from TALOS+ with chemical shift input of HN, N, CA, CB, C’

and HA. Angular restraints were obtained from one RDC datasets with Da, Rh calculated by Xplor-NIH. Distance restraints were provided by ^{15}N NOESY-HSQC NOE mainly for short range, and by PRE mainly for long range. Although torsion angle, RDCs, and NOEs provide sufficient information to anneal the VpuCyto to two helices, they are not enough to converge a set of structures to lower backbone RMSD. The inclusion of long-range distance restraints from PRE data was essential to produce the 3D structures. Ensembles of 20 lowest energy structures calculated with only dihedrals and NOEs (Figure 6.4.A), dihedral, NOEs and RDCs (Figure 6.4.B), and dihedral, NOEs, RDCs and PREs (Figure 6.4.C) with decreasing ensemble RMSDs, are exampled in Figure 6.4.

VpuCyto consists of two helices exhibiting a U-shape structure in DHPC micelles that are relatively well defined with an RMSD of 2.95 Å over all backbone atoms for a family of 20 VpuCyto structures (Figure 6.4.D). Disregarding the disordered terminal region, the helix-2-loop-helix-3 motif was well defined within the structure ensemble with 1.24 Å RMSD. The modest variations in the helices suggest that they are relatively rigid. The inter-helical loop itself appears to have RMSD of 0.7 Å. Along with a number of NOEs observed in residue 50-59 in the loop region, surprisingly it suggests that, the loop adopts as well defined structure. All the charged residues occur on either the end of the helices and the terminal region (Arg30, Lys31, Asp77, Asp80 and Asp81) or were restricted to the outer surface of the U-shape structure (Arg36, Arg40, Arg44, Gu65 and Glu69), presumably exposed to the aqueous media. The U-shape set of two helices also renders the more hydrophobic phase in the core of the structure.

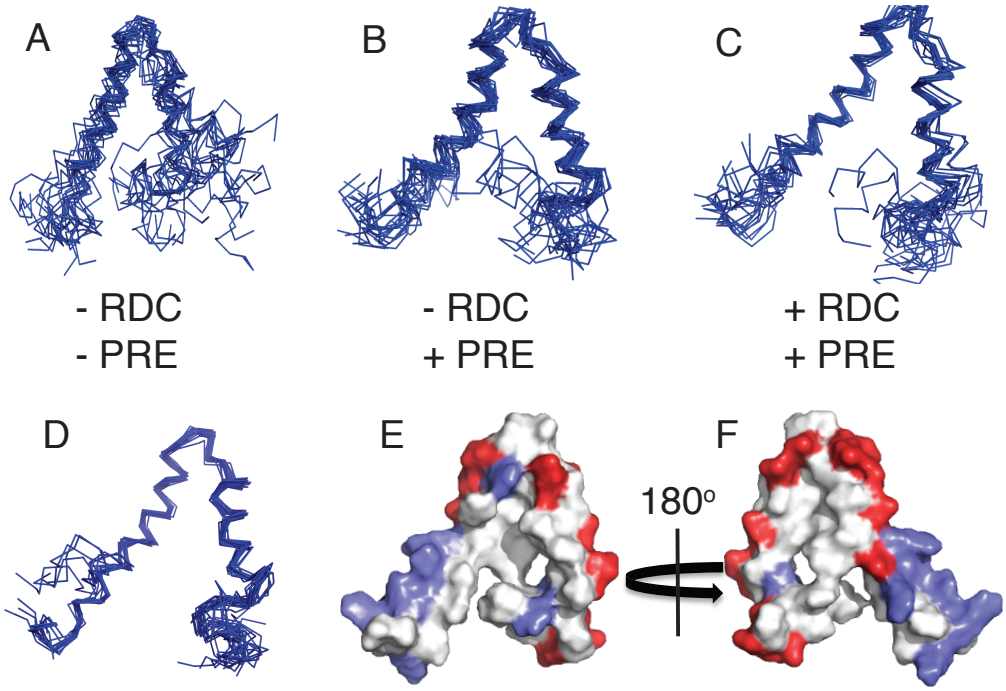

Figure 6.4 Structure refinement of VpuCyto in DHPC micelles.
Ensembles with 20 lowest energy structures obtained from A. Refinement with only chemical shift. B. Refinement with chemical shift and PRE. C. Refinement with both PRE and RDC. D. 20 lowest energy structure out of 100 from final refinement. E. The surface view of the lowest energy structure with acidic residues labeled red and basic residues labeled blue. F. 180^{o} rotate through y-axis of E.

6.4.5 Association of VpuCyto with the micelles

The depth of micelle insertion of VpuCyto backbone amide sites is reflected by the distance-dependent broadening effects of MnEDTA and 5SDA (Figure 6.5.A, 6.5.B). MnEDTA is a bulky paramagnetic reagent restricted to the aqueous environment; when MnEDTA was added to VpuCyto incorporated in DHPC micelles, signals of residues that are accessible to MnEDTA in solution are broadened, and the corresponding intensities are lowered; residues associated with the hydrophobic region of the micelles are less affected. Signals of residues that are broadened by MnEDTA are colored red (Figure

6.5.C). Addition of MnEDTA results in complete disappearance of signals from both N- and C-termini due to their exposure in the aqueous solvent and MnEDTA. In addition, signals of residue 34-40 in helix-2 completely disappeared, suggesting that the N terminal half of the helix-1 is located outside the micelles. Notably, in the completely exposed C-terminal region, resonances signals of W76 amide, it's indole nitrogen and H73 amide are not completely elimination by MnEDTA, suggesting their partial insertion in the micelles. The aromatic side chains of tryptophan and histidine are frequently found inserted in membranes as a result of the dipole moment of their aromatic ring interacting with the PC head group. Moreover, the loop region, believed to be highly mobile, is less broadened by MnEDTA than the terminal region. This suggests that the loop is more restricted in mobility as a result of partially micelle association, compared to the solvent exposed terminal region, and this finding agrees with what we observed in structure determination. The line broadening effects were not observed equally for both helices, and these in helix-2 were less affected, indicating that it is more structured and embedded in the center of the micelles. 5SDA is a fatty acid with an 18-carbon hydrophobic chain that has a nitroxide group labeled at the fifth carbon position close to the headgroup. When incorporated into the DHPC micelles, the 5SDA partitions to the hydrophobic interior of the micelles, and the spin label is at the center of the micelles. Thus, it can be used to probe the portion of protein embedded in the micelles. Signals of residues that are broadened by 5SDA are colored yellow, and those less affected are colored blue in Fig 6.4.D. Apparently, opposite effects were observed compare to MnEDTA. The residues at helix-3 were slightly more affected than those of helix-2, and the C-terminal region seemed to be more affected than the N-terminal region, and W76 and especially its

indole signals are the most broadened among all the residues. This is evidence that W76 is embedded in the micelles. Overall, line-broadening was invariant for VpuCyto in DHPC micelles with 5SDA compared to MnEDTA. The possible explanations are: (1) both DHPC and 5SDA are dynamic and undergoing rapid rearrangement, and it is possible that at the nitroxide group is not always inserted the center of the micelles but sometimes located near the head group region; (2) due to the amphipathic nature of VpuCyto, it is highly mobile and is not firmly embedded in the micelle, but more likely loosely associated with the micelles. Regardless of the protein dynamics, there is a consensus of the relative orientation of VpuCyto to the micelles (Figure 6.11.B).

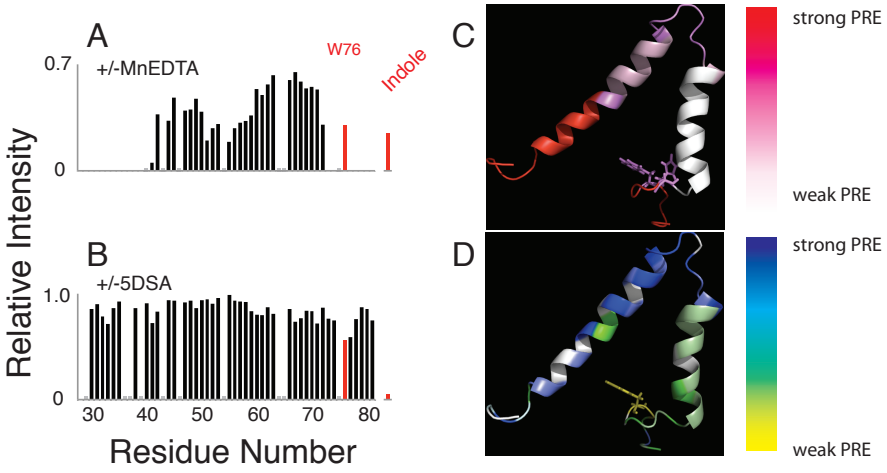

Figure 6.5 Micelles association of VpuCyto.

A. ^{1}H-^{15}N HSQC resonances intensity change measured before and after addition of MnEDTA. B. ^{1}H-^{15}N HSQC resonances intensity change measured before and after addition of 5SDA. C. Residues colored according to the PRE effect observed upon addition of MnEDTA. D Residues colored according to the PRE effect observed upon addition of 5SDA.

As compared to the previous VpuCyto structure in DPC micelles[187], there are some major differences. First, both helices in DPC micelles are substantially shorter, science helix-2 spans from I39- E48, and helix-3 spans from Q61-R69; whereas in DHPC, helix-2 spans from R34-E50, and helix-3 spans from E57-L70. Correspondingly, the inter-helical loop in DPC micelles is much longer. Also, the inter-helical distance is shorter in DPC (7 Å) than in DHPC (9 Å). In addition, the relative orientations of the two helices in the two structures are also different. The differences may arise from the difference in sequence, as well as the difference of the micelle environment.

6.4.6 VpuFull undergoes fast rotational diffusion at 25°C

Heteronuclear dipolar couplings are averaged when the samples are spinning at 54.7°, the magic angle, and therefore, MAS solid-state NMR requires recoupling pulse sequences to measure the dipolar couplings. The heteronuclear dipolar couplings measured from the unoriented proteins are uninformative, because of the powder averaging and the bond lengths (amide bonds or C-H bond at Cα) are essentially identical. However, when the proteins are undergoing fast rotational diffusion about the bilayer normal, the tensors are partially averaged, resulting in a "reduced powder pattern"[61; 203-205], whose parallel edges reflect the dipolar couplings upon the magnetic field. In order to measure the angular-dependent heteronuclear dipolar couplings, it is necessary find the condition of fast rotational diffusion for the proteins, and this technique is known as rotationally aligned (RA) solid-state NMR.

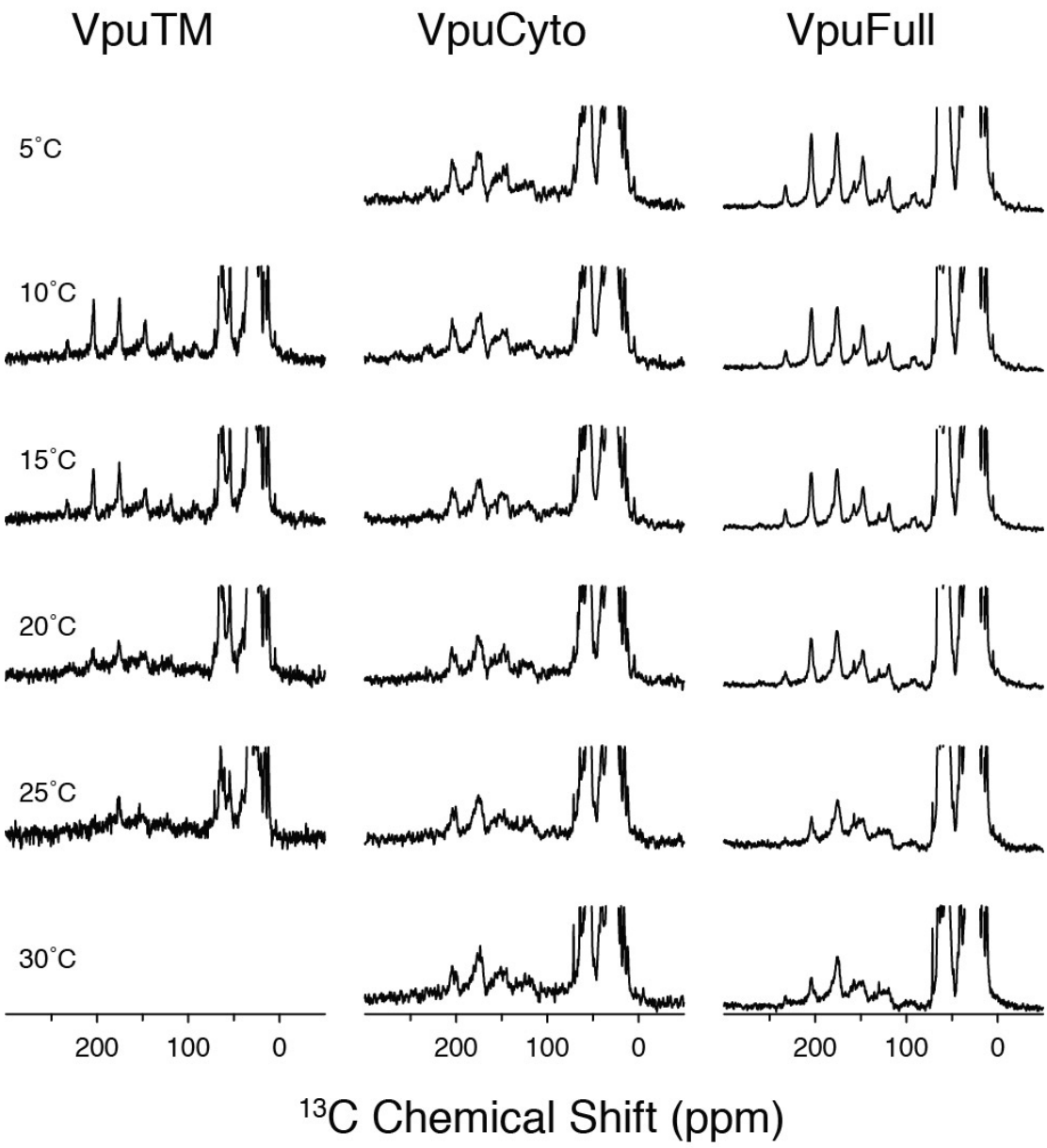

Figure 6.6 1D ^{13}C spectra of three constructs of Vpu.
A, VpuTM. B. VpuCyto. and C. VpuFull. All the spectra were acquired at 5,000 Hz spinning rate at various temperatures. VpuTM is frozen below 15 °C and undergoing fast rotational diffusion at 25 °C.

A series of ^{13}C CP spectra (Figure 6.6) were acquired at different temperature to find the minimum temperature for Vpu undergoing rotational diffusion with the low spinning rate (5,000 Hz) by observing the $^{13}C'$ sidebands. The results show that VpuTM has fast rotational diffusion when the temperature is higher than 25°C. On the other hand, no powder pattern is found even when VpuCyto is at 5°C, suggesting that the cytoplasmic domain is relatively dynamic. At high temperature, the ratios of the first left sideband to the signals of carbonyl carbon of VpuCyto is 0.5, which is relatively high comparing to VpuTM, showing the orientation of cytoplasmic domain is parallel to the lipid surface. By comparing the spectra of VpuTM, VpuCyto, and VpuFull, we find that the spectra of VpuFull are the combinations of the ones of VpuTM and VpuCyto. So, even the sidebands are not fully disappeared at high temperature in the spectra of VpuFull, we still can confirm that VpuFull is undergoing fast rotational diffusion at 25°C. Moreover, the reduced dipolar powder patterns are measured by ^{1}H-^{13}C/^{13}C and ^{1}H-^{15}N/^{13}C separated local field (SLF) experiments (Figure 6.7), provide direct evidence that Vpu is undergoing fast rotational diffusion at this temperature. Figure 6.8.A and 6.8.B shows that we can obtain high-resolution ^{13}C/^{13}C and ^{13}C/^{15}N correlation spectra under these experimental conditions, and the spectral resolutions are further improved in three-dimensional experiments.

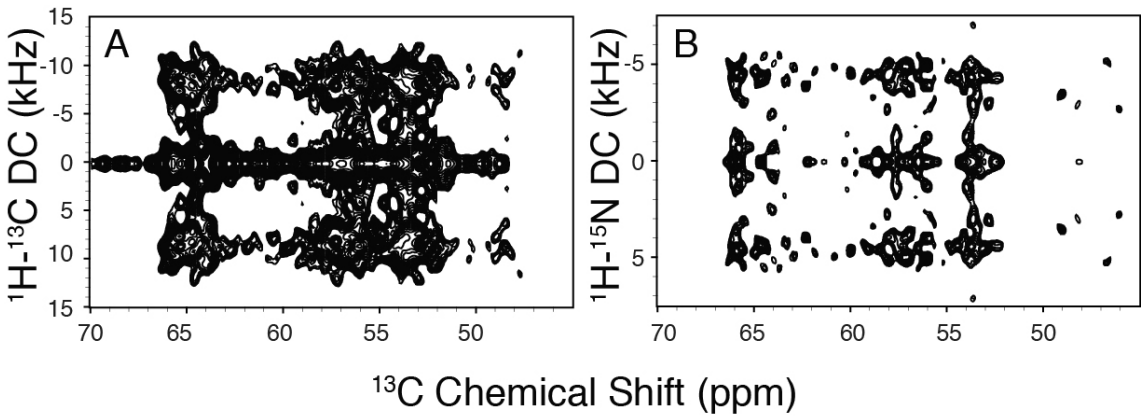

Figure 6.7 ^{1}H-^{13}C/^{13}C and ^{1}H-^{15}N/^{13}C SLF spectra of VpuFull.
A. ^{1}H-^{13}C/^{13}C SLF spectrum. B. ^{1}H-^{15}N/^{13}C SLF spectrum. The various dipolar couplings obtained from both experiments show that VpuFull is undergoing fast rotational diffusion, and single-site resolution is achievable when VpuFull is incorporated in proteoliposomes at 25 °C.

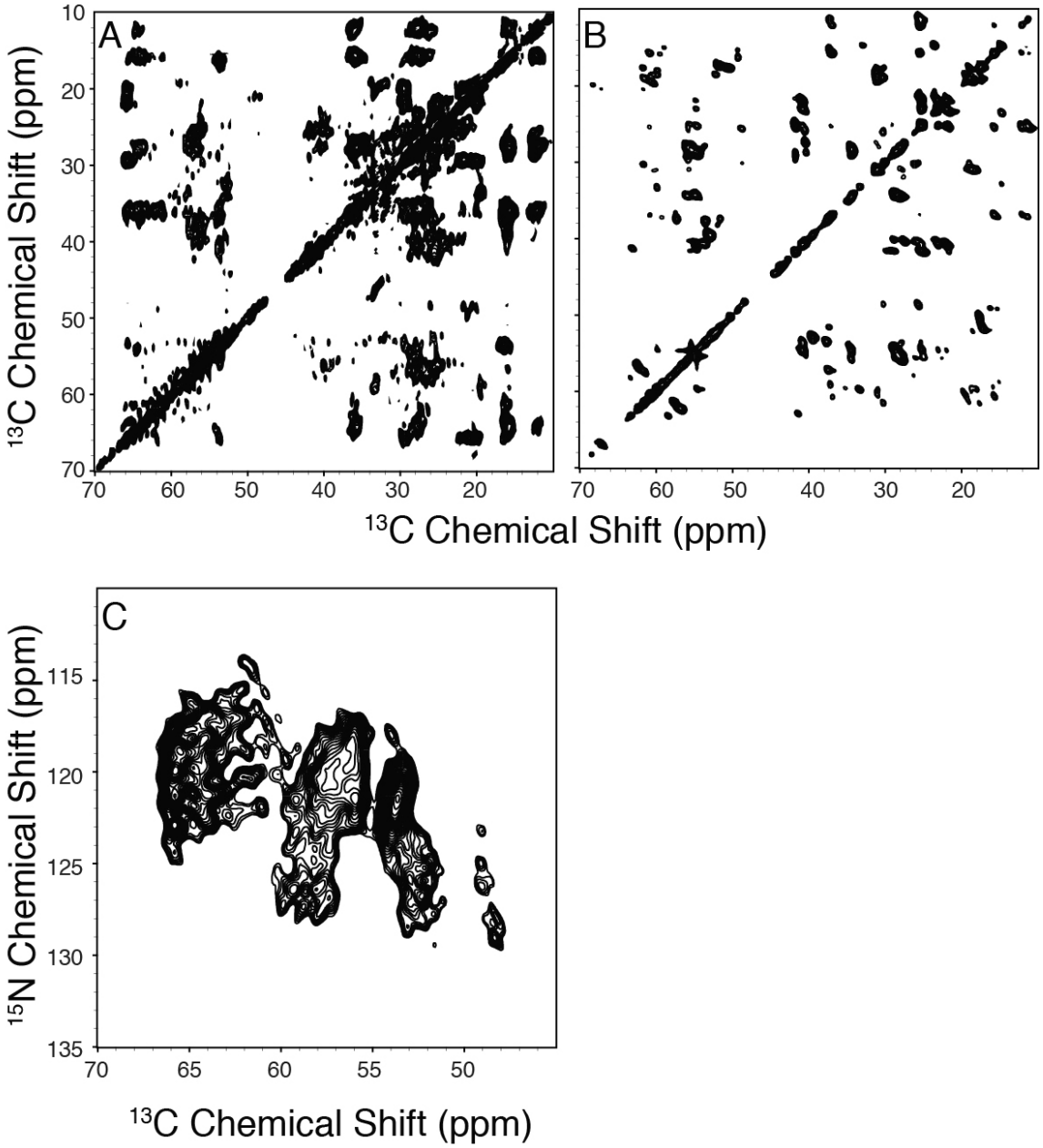

Figure 6.8 Correlation spectra of VpuFull.
A. $^{13}C/^{13}C$ correlation spectrum obtained with 50 ms PDSD mixing. B. $^{15}N/^{13}C$ HETCOR spectrum, where the $^{15}N/^{13}C$ transfer is obtained from SPECIFIC-CP. Both experiments show single-site resolution is achievable when VpuFull is incorporated in proteoliposomes at 25 °C. C. $^{13}C/^{13}C$ TOBSY spectrum of VpuFull in proteoliposomes. J-coupling based $^{13}C/^{13}C$ correlation spectrum indicates the mobile region of VpuFull. These resonances are contributed from about 30 residues, and they are partially assigned according to the chemical shifts and the cross-validations of L41C-MTSL and MnEDTA PRE experiments. The PRE experiments will be discussed in the following sections.

Table 6.2 List of chemical shifts and dipolar couplings of VpuFull in proteoliposomes.

Residue	^{15}N chemical shift (ppm)	^{13}Cα chemical shift (ppm)	^{13}C' chemical shift (ppm)	^{1}H-^{15}N dipolar couplings (kHz)	^{1}H-^{13}C dipolar couplings (kHz)
I8	119.52	65.30	175.90	8.5	
V9	119.93	66.80	176.69	8.5	18.1
A10	116.54	55.39	175.62		15.2
L11	119.26	58.53	176.15	7.7	17.7
V12	119.70	66.77	175.68	10.6	6.9
V13	120.64	66.66	175.57	4.5	12.9
A14	121.48	54.52	176.03	3.5	14.5
I15	115.91	63.85	176.20	7.4	17.6
I16	122.12	65.29	176.00	9.2	18.6
I17	121.84	65.05	176.14	4.3	16.4
A18	121.44	54.31	177.07	9.5	5.9
I19	116.00	64.61	176.98	10.3	18.3
V20	122.70	66.74	175.87	4.8	17.1
V21	120.20	66.56	175.67	4.5	14.6
W22	121.45	56.54	177.27	8.2	15.3
S23	118.8	60.19	175.99	9.1	15.0
I24	115.36	64.66	176.99		14.9
V25	121.10	66.96	176.59	6.0	16.9
I26	120.79	64.54	176.03	8.4	
I27	122.04	66.56	175.75	8.6	
Q35	120.84	60.81	174.68	7.6	
R36	116.76	60.34	177.83		15.3
K37	120.94	60.81	174.94	7.8	
I38	118.10	63.39	176.31		19.6
D39	119.20	56.44	176.81		
R40	121.63	54.80	177.05	7.8	14.8
L41	118.82	58.25	177.62	9.2	2.4
I42	118.20	63.42	176.63	8.5	
D43	119.59	56.96	176.55	6.3	13.5
R44	121.76	57.08	176.97	8.1	18.6
L45	120.35	57.78	175.88	8.6	16.6
I46	119.07	65.05	175.97	8.9	15.4
E47	122.35	60.12	177.29	8.0	7.3
R48	122.48	56.98	176.83	6.7	9.2
E59	117.57	58.99	177.28		
I60	119.07	65.55	176.01	7.4	16.2
S61	117.32	58.05	175.87	8.6	15.8
A62	120.23	52.83	175.95	5.9	3.4
L63	115.86	56.65	176.98		16.0
V64	119.73	66.96	176.86	8.6	17.8
E65	118.47	58.28	176.50	5.3	
L66	115.81	58.05	175.97	8.0	13.9
G67	103.05	46.51	173.83	1.3	
V68	115.55	66.44	175.66	6.5	
E69	120.24	59.42	176.01	7.2	18.2
L70	125.55	60.04	174.02	9.2	13.4

6.4.7 Secondary structures of VpuFull in proteoliposomes

The mobile regions of Vpu are determined by TOBSY (total through-bond correlation spectroscopy)[206; 207], which is a J-coupling based $^{13}C/^{13}C$ correlation spectrum. J-coupling is relatively small in solid-state NMR, and it is only observed when the residues are mobile enough to average out the dipolar couplings. Complementarily, dipolar based NCACX and NCOCX experiments provides the information of immobile or structured parts of VpuFull, which allow us to assign the chemical shifts of ^{15}N, $^{13}C\alpha$ and $^{13}C'$, sequentially. In these assignment experiments, the magnetization is transferred from amide protons to ^{15}N with CP, and then to $^{13}C\alpha$ or $^{13}C'$ by SPECIFIC-CP, and the $^{13}C/^{13}C$ correlations are achieved with DARR mixing.

About 30 residues are found in the TOBSY spectrum (Figure 6.8.C) based on their chemical shifts. Even though site-specific assignments are infeasible due to the lack of assignment experiment, we narrow down the assignments by considering the dynamics studies of VpuCyto in micelles. Most of residues are found in the second loop and both termini, suggesting these regions are highly dynamic in the lipid bilayer environment. 43 immobile residues are assigned by NCACX and NCOCX experiments (Figure 6.9.A), and their dipolar couplings are found from ^{1}H-$^{15}N/^{15}N/^{13}C$ and ^{1}H-$^{13}C/^{15}N/^{13}C$ three-dimensional SLF experiments, consequentially. All the measurements of chemical shifts and dipolar couplings are listed in Table 6.2. Three dipolar waves are found in the plot of dipolar coupling versus residue number (Figure 6.9.B), which only exist when the secondary structures are helices. The length and tilting angle of helix-1 agrees with the previous findings[65; 183; 184; 208].

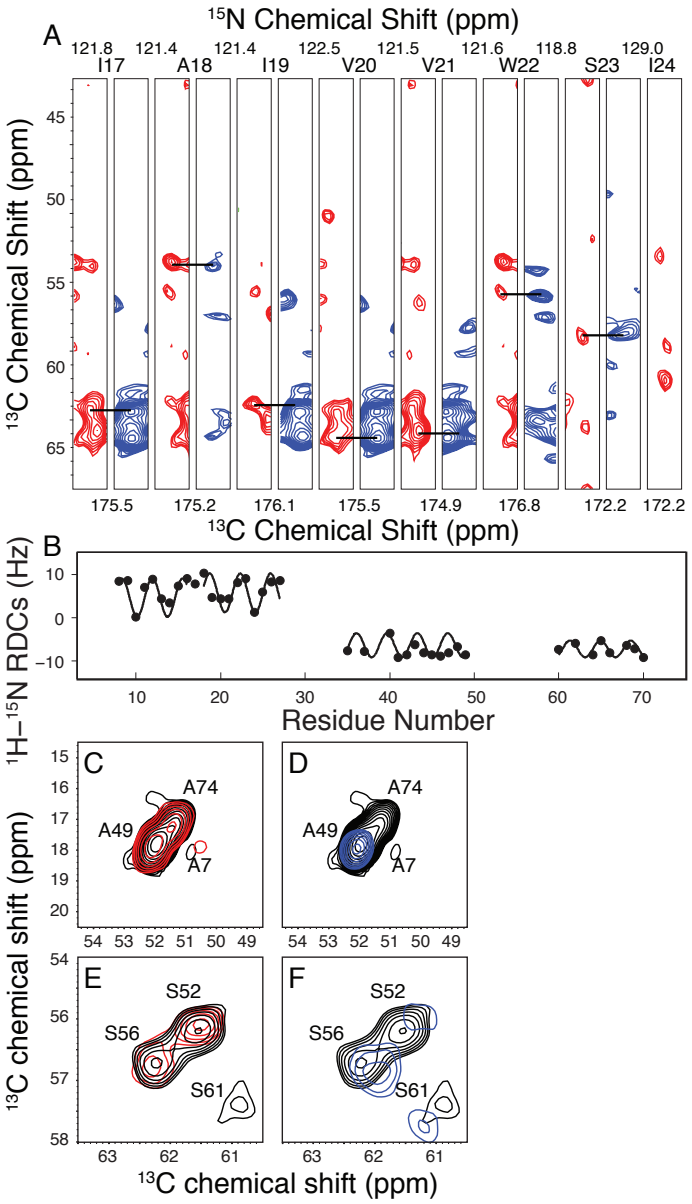

Figure 6.9 NMR measurements for structure calculation of VpuFull in DMPC proteoliposomes.

A. Strip plots from NCACX (red) and NCOCX (blue) demonstrate the backbone walk on VpuFull. B. The dipolar couplings are measured according to the assignments. Three dipolar waves are found from the plot of ^{1}H-^{15}N dipolar coupling versus residue number, which confirms the helical characters in VpuFull. C. and E. The comparison of alanines (C.) and serines (E.) in L41C-MTSL VpuFull (red) and reduced L41C-MTSL VpuFull (black). D. and F. The comparison of alanines (D.) and serines (F.) in reduced L41C-MTSL VpuFull (black) and reduced L41C-MTSL VpuFull presenting in MnEDTA solution (blue).

6.4.8 Tertiary structures of VpuFull in proteoliposomes

Dipolar couplings and CSAs provide angular restraints to determine the orientations of secondary structures. However, we would obtain degeneracies from structural calculations only relying on the angular restraints. For instance, the two helices in the cytoplasmic domain could be linear or form a U-shape based on the analysis of dipolar couplings. Distance restraints provide valuable information to fully understand the relations between the secondary structures. In solid-state NMR, the distance restraints could be extract from spin diffusion with long mixing time. For instance, the correlation of serine pair is found in Mercury transporter protein F (MerF) with 200 ms DARR mixing[155].

Since no significant correlations are found from $^{13}C/^{13}C$ correlation with DARR mixing up to 200 ms for VpuFull, two PRE approaches are applied to obtain the long-range restraints: (1) MTSL is labeled on L41C VpuFull to probe the distances of neighbor nuclei. (2) MnEDTA is utilized to distinguish if the residues are exposed in the solution or embed in the lipids, which helps us to understand how the cytoplasmic domain of the full-length Vpu interacts with lipids. The intensities of the resonances from TOBSY spectra are varied based the different geometry information obtained from PRE experiments, and therefore, we can further assign the resonance for the mobile region site-specifically. For instance, A7, A49 and A74 are found in the TOBSY spectra (Figure 6.8.C), yet they are ambiguous without assignment experiments. The intensities are reduced by L41C-MTSL, suggesting the helix-2 and helix-3 form a U-shape conformation, and these resonances are assigned according to the ratios of the L41C-MTSL and its reduced form (Figure 6.9.C). On the other hand, A74 disappears from the

MnEDTA experiment showing (Figure 6.9.D), which indicates A74 is exposed to the solvent. Similarly, we can assign serines according to the changes of intensities when the Cyto domain is a U-shape (Figure 6.9.E). S61 is less affected from MnEDTA solution, suggestions that S61 in helix-3 may face to the lipids or slightly embeded into the lipids, and S52 and S56 are more exposed in the solution (Figure 6.9.F).

Refined structures driven only from dipolar couplings give many possible conformations (Figure 6.10.A), where the relative orientations between helix-2 and helix-3 are allowed to form either linear or U-shape. By considering the distant restraints obtain from L41C-MTSL VpuFull, the helix-3 is folded back, yet the relative orientation between cytoplasmic domain and membrane surface is still ambiguous (Figure 6.10.B). Helix-3 is further confined around lipid surface by introducing the plane distance restraint that obtained from MnEDTA experiment (Figure 6.10.C). The RMSD of ten lowest structures shows that all the helices are well defined, whose RMSD are 0.48 Å, 0.31 Å, and 0.23 Å for helix-1, helix-2, and helix-3, respectively. Most of the variations come from the loop regions (loop-1 is 1.92 Å and loop-2 is 2.74 Å), and the RMSD of the structural region (7-70) is significantly improved and converges at 5.18 Å. Loop-2 found in VpuFull is longer and more flexible comparing to VpuCyto. Helix-3 was observed to have a high degree of flexibility, which may be attributed to fewer structural restraints imposed in the calculation or the intrinsic dynamics properties. The relative mobility of helix-3 can be seen in the ten structures with the lowest energy.

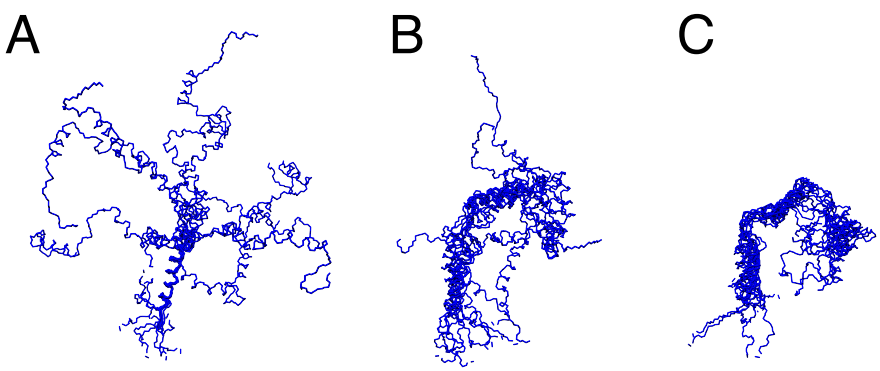

Figure 6.10 Structure refinement of VpuFull in DMPC proteoliposomes.
Ten lowest structures obtained in each step, and the structure with the lowest energy was used as the initial structure for the refinement in the next step. The restraints used in each step: A. ^{1}H-^{15}N and ^{1}H-^{13}C dipolar couplings and dihedral angles. B. Distance restraints driven from L41C-MTSL VpuFull and the restraints used in (A.). C. Plane distance restraints driven from MnEDTA experiment and the restraints used in (B.).

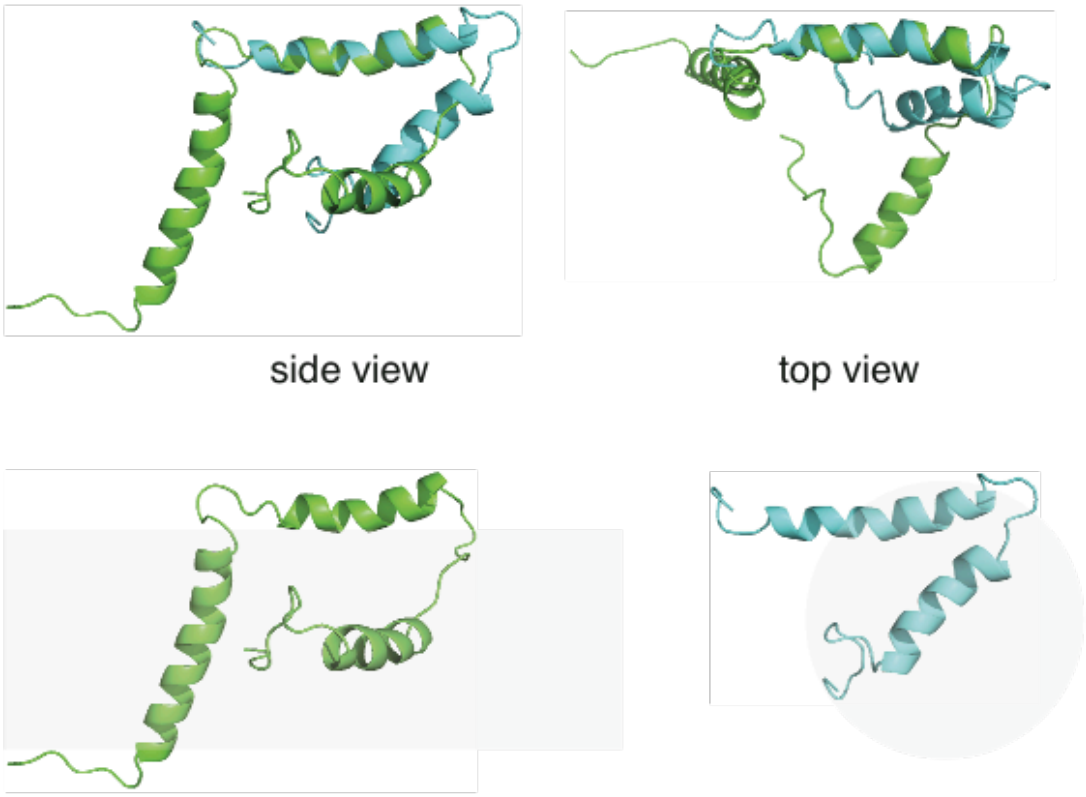

Figure 6.11 Structure comparison of VpuCyto and VpuFull.
A. Cartoon representation of VpuFull in DMPC proteoliposomes. B. Cartoon representation of VpuCyto in DHPC micelles. C. Alignment of VpuFull and VpuCyto structures.

6.4.9 Structure comparison of VpuCyto and VpuFull

Both constructs have well-defined helix-2 and helix-3 (Figure 6.11). The lengths of both helices are longer in VpuCyto in DHPC micelles, and loop-2 is shorter and partially structured in VpuCyto. These features may be caused by the interactions with the short-chain lipids. Helix-3 partially inserts into micelles. It may stabilize itself and gain length. The insertion of helix-3 would also reduce the flexibility of loop-2 and result

in a structured inter-helical loop. In contrast, loop-2 is longer and flexible in VpuFull, which might make helix-3 movable on the hydrophobic/hydrophilic interface, and loop-1 is also relative dynamic, which agrees the observation from N-terminal of VpuCyto. Both loops are crucial to make Vpu dynamic intrinsically.

6.5 Conclusion

NMR spectroscopy is a versatile technique that can be used to investigate structure, dynamics and interactions of membrane proteins in a variety of membrane environments with variable parameters ranging from lipid composition, temperature, and ion concentration to pH. Especially, with the advent of novel solid-state MAS experiments, structure determination of membrane proteins can be performed in phospholipid bilayer systems at physiological condition.

In this article, two constructs of Vpu were studied by solution and solid-state NMR. The dynamics of VpuCyto were investigated in both aqueous solution and DHPC micelles by solution NMR. VpuCyto is believed to be in an intermediate state between fully structured and fully disordered in aqueous media, while in micelles two helices are distinguishable. The 3D structure of VpuCyto in DHPC micelles at pH 4 were obtained base on NMR measurements of chemical shift, NOE, RDC and PRE. In the structure of VpuCyto in DHPC micelles, helix-2 and helix-3 are found to adopt a U-shape. Loop-2 is partially structured, which could be caused by the interactions with the micelles, and both termini are highly mobile. On the other hand, the structure of VpuFull is solved in DMPC proteoliposomes at pH 7.3, which are close to the physiological conditions, by solid-state MAS NMR experiments. Isotropic chemical shifts, ^{1}H-^{15}N and ^{1}H-^{13}C dipolar couplings

and PRE distance restraints are measured for structural refinement. Three well-defined helices are obtained from TM and Cyto domain as expected. Helix-2 and helix-3 adopt are loose U-shape on the bilayer surface. Loop-2 is longer than it has been found in VpuCyto in micelles, leading to a longer inter-helical distance between helix-2 and helix-3, as well as the increase in the flexibility of helix-3, which is wobbling on the lipid surface according to the ten lowest structures.

Both TM and Cyto domains have biological functions. The TM/TM interactions of Vpu/BST-2 and Vpu/NTB-A have been study by NMR, which give promising results with the findings in the biological experiments. The studies of interactions of Cyto domain in the molecular level are still missed. To fully reveal the properties and functions in the molecular level, it will be worth to carefully study dynamics of the Cyto domain of full-length Vpu presenting in long-chain lipid, such as, nanodiscs, and study the interactions with its biological components by solution and solid-state NMR.

Chapter 6 is currently being prepared for submission for publication of the material.

Chapter 7 Conclusion

Solid-state NMR has solved several structures of membrane proteins in their native environments, such as, Vpu, P7, MerF, and CXCR1, showing this technique is proper and robust. Oriented-sample (OS) solid-state NMR gives high-resolution spectra based on the mechanically or magnetically aligned samples. Under this condition, separated-local-field (SLF) experiments, such as, PISEMA, SAMMY, PISEMO, etc., measure the heteronuclear dipolar couplings while ^{1}H homonuclear dipolar couplings are suppressed in t1 dimension, and acquires chemical shift anisotropies (CSAs) in t2 dimension. Heteronuclear dipolar couplings and CSAs are anisotropic tensors, which are treated as angular restraints during structure refinement. The heteronuclear dipolar couplings measured by OS solid-state NMR have larger scaling factors than the ones acquired in rotationally aligned (RA) solid-state NMR. In practical, large scaling factors result in more precise measurements, and this effect is eminent especially when dipolar couplings are small, for instance, ^{15}N-^{13}C dipolar couplings. Traditionally, these pulse sequences are applied to ^{15}N-labeled samples to obtain the backbone structures, where we only need to suppress ^{1}H homonuclear dipolar couplings.

To further examine the side-chain conformations, it requires uniformly ^{13}C-labeled samples; however, both ^{1}H and ^{13}C homonuclear dipolar couplings would reduce the signals. Dual-PISEMO (D-PISEMO) has been introduced to address this issue, which employs multi-pulse on both channels simultaneously to remove the dipolar couplings. The line widths in the t1 dimension have been significantly improved in uniformly ^{13}C-

labeled NAL single crystal showing that homonuclear dipolar couplings are suppressed, and D-PISEMO also works on the biological samples. Moreover, we can acquire the signals during the windows between the pulses, called window-detection (WD), which offers the chance to directly observe dipolar couplings in one-dimensional experiments. Shiftless spectroscopy can utilize WD-PISEMO and applies to uniformly ^{13}C-labeled samples in the future.

Another challenge in solid-state NMR is to improve the efficiency of ^{15}N-^{13}C transfers due to their small dipolar couplings (<1 kHz). The irradiation of 1H with the mismatch condition during the cross-polarization (CP) between ^{15}N and ^{13}C causes the magnetization transfer through the ^{1}H bath, and this mechanism has been demonstrated that the magnetization transfer can fully rely on ^{1}H bath in the ^{15}N, $^{13}C_{\alpha}$-labeled NAL single crystal. We also showed that ^{1}H mismatch irradiation is a complementary method to CP for biological samples.

Non-uniform sampling (NUS) is an alternative approach to accelerate the high-dimensional experiments. We introduce compressed sensing (CS) to solid-state NMR spectroscopy and improve the reproducibility of reconstructions by adding the uniform sampling region in the sampling schemes. CS is able to reconstruct most of high-resolution spectra, for instance, homonuclear or heteronuclear correlation spectra, or SLF spectra. When the signal-to-noise ratio is higher than 10, CS can recover the spectra with 25% ~ 33% of data.

Instead of applying Fourier transform to the indirect dimension to obtain the high-dimensional spectra, covariance (COV) NMR spectroscopy provides high-sensitivity and high-resolution homonuclear correlation spectra by calculating the covariance of the

frequency-domain signals in the indirect dimension. We proposed the alternative States sampling scheme to sample the signals between cosine- and sine-modulated signals, which could further reduce at least 50% of experimental time without raising artifacts.

Vpu is one of the accessory proteins from HIV-1, consisting by 81 residues, which has one helix in the transmembrane domain and two helices in the cytoplasmic domain. The studies of solution NMR and biological experiments suggest that the cytoplasmic domain is highly dynamic and this effect could reduce the sensitivity and resolution in OS solid-state NMR. To deal with this problem, we use RA solid-state NMR to measure the perpendicular edges of the reduced dipolar powder patterns when the proteins are undergoing fast rotational diffusion presenting the proteoliposomes, which is equivalent to measurements of dipolar couplings from OS solid-state NMR, and they provide the restraints during the structure refinements. About 30 residues are found in the J-coupling based ^{13}C-^{13}C correlation spectrum, suggesting Vpu is partial dynamic, and based on the literatures and dynamic studies in solution NMR, we know that these residues are mainly from C-terminal, and the loop regions. To understand the tertiary structure of Vpu, we also use paramagnetic relaxation enhancement (PRE) experiments to probe the distances among the helices and the relative distances from the membrane surface. Three helices are obtained from the refinements, and the loop between the second and the third helix is floppy, which provides the flexibility of the third helix. From our results, the third helix could partially embed into or lying on the membrane, which could involve in binding to or recruiting its interaction partners.

In summary, my thesis describes the method developments of solid-state NMR, from signal processing to pulse sequences, and also provides an application to solve

membrane protein Vpu by solid-state NMR. Understanding the structure of Vpu not only provides the biological insights, but also shows that solid-state NMR spectroscopy is a robust technology to solve the membrane protein structures with various sizes and dynamics.

Bibliography

[1] B.B. Das, S.H. Park, and S.J. Opella, Membrane protein structure from rotational diffusion. Biochimica et Biophysica Acta (BBA) - Biomembranes 1848 (2015) 229-245.

[2] B.B. Das, E.C. Lin, and S.J. Opella, Experiments Optimized for Magic Angle Spinning and Oriented Sample Solid-State NMR of Proteins. The Journal of Physical Chemistry B 117 (2013) 12422-12431.

[3] S.H. Park, B.B. Das, F. Casagrande, Y. Tian, H.J. Nothnagel, M. Chu, H. Kiefer, K. Maier, A.A. De Angelis, F.M. Marassi, and S.J. Opella, Structure of the chemokine receptor CXCR1 in phospholipid bilayers. Nature 491 (2012) 779-783.

[4] S.J. Opella, and F.M. Marassi, Structure determination of membrane proteins by NMR spectroscopy. Chem. Rev. 104 (2004) 3587-3606.

[5] S.J. Opella, Structure Determination of Membrane Proteins in Their Native Phospholipid Bilayer Environment by Rotationally Aligned Solid-State NMR Spectroscopy. Acc. Chem. Res. 46 (2013) 2145-2153.

[6] J. Radoicic, G.J. Lu, and S.J. Opella, NMR structures of membrane proteins in phospholipid bilayers. Q. Rev. Biophys. 47 (2014) 249-283.

[7] F.M. Marassi, B.B. Das, G.J. Lu, H.J. Nothnagel, S.H. Park, W.S. Son, Y. Tian, and S.J. Opella, Structure determination of membrane proteins in five easy pieces. Methods 55 (2011) 363-369.

[8] B.B. Das, H.J. Nothnagel, G.J. Lu, W.S. Son, Y. Tian, F.M. Marassi, and S.J. Opella, Structure Determination of a Membrane Protein in Proteoliposomes. J. Am. Chem. Soc. 134 (2012) 2047-2056.

[9] B. Alberts, D. Bray, J. Lewis, M. Raff, K. Roberts, J.D. Watson, and A. Grimstone, Molecular Biology of the Cell (3rd edn). Trends in Biochemical Sciences 20 (1995) 210-210.

[10] E. Wallin, and G.V. Heijne, Genome-wide analysis of integral membrane proteins from eubacterial, archaean, and eukaryotic organisms. Protein Science 7 (1998) 1029-1038.

[11] J.P. Overington, B. Al-Lazikani, and A.L. Hopkins, How many drug targets are there? Nat Rev Drug Discov 5 (2006) 993-996.

[12] K.-N. Hu, V.S. Bajaj, M. Rosay, and R.G. Griffin, High-frequency dynamic nuclear polarization using mixtures of TEMPO and trityl radicals. J. Chem. Phys. 126 (2007) 044512-7.

[13] C.-G. Joo, K.-N. Hu, J.A. Bryant, and R.G. Griffin, In Situ Temperature Jump High-Frequency Dynamic Nuclear Polarization Experiments: Enhanced Sensitivity in Liquid-State NMR Spectroscopy. J. Am. Chem. Soc. 128 (2006) 9428-9432.

[14] D.A. Hall, D.C. Maus, G.J. Gerfen, S.J. Inati, L.R. Becerra, F.W. Dahlquist, and R.G. Griffin, Polarization-Enhanced NMR Spectroscopy of Biomolecules in Frozen Solution. Science 276 (1997) 930-932.

[15] K. Kazimierczuk, and V.Y. Orekhov, Accelerated NMR Spectroscopy by Using Compressed Sensing. Angew. Chem. Int. Edit. Engl. 50 (2011) 5556-5559.

[16] M. Lustig, D.L. Donoho, J.M. Santos, and J.M. Pauly, Compressed Sensing MRI. IEEE Signal Proc. Mag. 25 (2008) 72-82.

[17] M. Lustig, D. Donoho, and J.M. Pauly, Sparse MRI: The application of compressed sensing for rapid MR imaging. Magn. Reson. Med. 58 (2007) 1182-1195.

[18] I. Drori, Fast l1 minimization by iterative thresholding for multidimensional nmr spectroscopy. EURASIP J. Adv. Sig. Pr. 1 (2007).

[19] D.L. Donoho, Compressed sensing. IEEE T. Inform. Theory 52 (2006) 1289-1306.

[20] I. Noda, Generalized two-dimensional correlation method applicable to infrared, Raman, and other types of spectroscopy. Applied spectroscopy 47 (1993) 1329-1336.

[21] I. Noda, Two-dimensional infrared (2D IR) spectroscopy: theory and applications. Applied Spectroscopy 44 (1990) 550-561.

[22] F. Zhang, and R. Brüschweiler, Indirect Covariance NMR Spectroscopy. J. Am. Chem. Soc. 126 (2004) 13180-13181.

[23] R. Brüschweiler, and F. Zhang, Covariance nuclear magnetic resonance spectroscopy. J. Chem. Phys. 120 (2004) 5253-5260.

[24] R. Brüschweiler, Theory of covariance nuclear magnetic resonance spectroscopy. J. Chem. Phys. 121 (2004) 409-414.

[25] Y. Tian, G. Lu, F. Marassi, and S. Opella, Structure of the membrane protein MerF, a bacterial mercury transporter, improved by the inclusion of chemical shift anisotropy constraints. J. Biomol. NMR 60 (2014) 67-71.

[26] S.H. Park, F.M. Marassi, D. Black, and S.J. Opella, Structure and Dynamics of the Membrane-Bound Form of Pf1 Coat Protein: Implications of Structural Rearrangement for Virus Assembly. Biophys. J. 99 (2010) 1465-1474.

[27] A.C. Zeri, M.F. Mesleh, A.A. Nevzorov, and S.J. Opella, Structure of the coat protein in fd filamentous bacteriophage particles determined by solid-state NMR spectroscopy. Proc. Natl. Acad. Sci. USA 100 (2003) 6458-63.

[28] X. Jia, E. Weber, A. Tokarev, M. Lewinski, M. Rizk, M. Suarez, J. Guatelli, and Y. Xiong, Structural basis of HIV-1 Vpu-mediated BST2 antagonism via hijacking of the clathrin adaptor protein complex 1, 2014.

[29] J.G. Magadán, F.J. Pérez-Victoria, R. Sougrat, Y. Ye, K. Strebel, and J.S. Bonifacino, Multilayered Mechanism of CD4 Downregulation by HIV-1 Vpu Involving Distinct ER Retention and ERAD Targeting Steps. PLoS Pathog 6 (2010) e1000869.

[30] A. Tokarev, and J. Guatelli, Misdirection of membrane trafficking by HIV-1 Vpu and Nef. Cellular logistics 1 (2011) 90-102.

[31] M. Dube, M. Bego, C. Paquay, and E. Cohen, Modulation of HIV-1-host interaction: role of the Vpu accessory protein. Retrovirology 7 (2010) 114.

[32] J. Guatelli, Interactions of Viral protein U (Vpu) with Cellular Factors. in: P. Spearman, and E.O. Freed, (Eds.), HIV Interactions with Host Cell Proteins, Springer Berlin Heidelberg, 2009, pp. 27-45.

[33] S.J.D. Neil, T. Zang, and P.D. Bieniasz, Tetherin inhibits retrovirus release and is antagonized by HIV-1 Vpu. Nature 451 (2008) 425-430.

[34] N. Roy, G. Pacini, C. Berlioz-Torrent, and K. Janvier, Mechanisms underlying HIV-1 Vpu-mediated viral egress. Frontiers in Microbiology 5 (2014).

[35] Peter W. Ramirez, M. Famiglietti, B. Sowrirajan, Ana B. DePaula-Silva, C. Rodesch, E. Barker, A. Bosque, and V. Planelles, Downmodulation of CCR7 by HIV-1 Vpu Results in Impaired Migration and Chemotactic Signaling within CD4+ T Cells. Cell Reports 7 (2014) 2019-2030.

[36] S. Bolduan, T. Reif, M. Schindler, and U. Schubert, HIV-1 Vpu mediated downregulation of CD155 requires alanine residues 10, 14 and 18 of the transmembrane domain. Virology 464–465 (2014) 375-384.

[37] S. Bolduan, P. Hubel, T. Reif, V. Lodermeyer, K. Höhne, J.V. Fritz, D. Sauter, F. Kirchhoff, O.T. Fackler, M. Schindler, and U. Schubert, HIV-1 Vpu affects the anterograde transport and the glycosylation pattern of NTB-A. Virology 440 (2013) 190-203.

[38] A.S. Stern, K.-B. Li, and J.C. Hoch, Modern Spectrum Analysis in Multidimensional NMR Spectroscopy: Comparison of Linear-Prediction Extrapolation and Maximum-Entropy Reconstruction. J. Am. Chem. Soc. 124 (2002) 1982-1993.

[39] J.C. Hoch, and A.S. Stern, Maximum entropy reconstruction, spectrum analysis and deconvolution in multidimensional nuclear magnetic resonance, Methods in enzymology, Academic Press, 2002, pp. 159-178.

[40] S. Sibisi, J. Skilling, R.G. Brereton, E.D. Laue, and J. Staunton, Maximum entropy signal processing in practical NMR spectroscopy. Nature 311 (1984) 446-447.

[41] G.J. Daniell, and P.J. Hore, Maximum entropy and NMR-A new approach. J. Magn. Reson. 84 (1989) 515-536.

[42] T. Luan, V. Jaravine, A. Yee, C. Arrowsmith, and V. Orekhov, Optimization of resolution and sensitivity of 4D NOESY using Multi-dimensional Decomposition. J. Biomol. NMR 33 (2005) 1-14-14.

[43] V.Y. Orekhov, I. Ibraghimov, and M. Billeter, Optimizing resolution in multidimensional NMR by three-way decomposition. J. Biomol. NMR 27 (2003) 165-173-173.

[44] S.H. Park, B.B. Das, A.A. De Angelis, M. Scrima, and S.J. Opella, Mechanically, Magnetically, and ,ÄúRotationally Aligned,Äù Membrane Proteins in Phospholipid Bilayers Give Equivalent Angular Constraints for NMR Structure Determination. The Journal of Physical Chemistry B (2010) null-null.

[45] S.J. Opella, A.C. Zeri, and S.H. Park, Structure, dynamics, and assembly of filamentous bacteriophages by nuclear magnetic resonance spectroscopy. Annu. Rev. Phys. Chem. 59 (2008) 635-57.

[46] T.A. Cross, and S.J. Opella, NMR of fd coat protein. J Supramol Struct 11 (1979) 139-45.

[47] C.R. Sanders, and G.C. Landis, Reconstitution of membrane proteins into lipid-rich bilayered mixed micelles for NMR studies. Biochemistry 34 (1995) 4030-4040.

[48] S.H. Park, S. Berkamp, G.A. Cook, M.K. Chan, H. Viadiu, and S.J. Opella, Nanodiscs versus Macrodiscs for NMR of Membrane Proteins. Biochemistry 50 (2011) 8983-8985.

[49] A. Ramamoorthy, and S.J. Opella, Two-dimensional chemical shift/heteronuclear dipolar coupling spectra obtained with polarization inversion spin exchange at the magic angle and magic-angle sample spinning (PISEMAMAS). Solid State Nucl. Magn. Reson. 4 (1995) 387-92.

[50] C. Wu, A. Ramamoorthy, and S. Opella, High-resolution heteronuclear dipolar solid-state NMR spectroscopy. J. Magn. Reson. A109 (1994) 270-272.

[51] A.A. Nevzorov, M.F. Mesleh, and S.J. Opella, Structure determination of aligned samples of membrane proteins by NMR spectroscopy. Magn. Reson. Chem. 42 (2004) 162-71.

[52] A.A. Nevzorov, and S.J. Opella, A "magic sandwich" pulse sequence with reduced offset dependence for high-resolution separated local field spectroscopy. J. Magn. Reson. 164 (2003) 182-6.

[53] C.H. Wu, and S.J. Opella, Proton-detected separated local field spectroscopy. J. Magn. Reson. 190 (2008) 165-170.

[54] W.I. Goldburg, and M. Lee, Nuclear Magnetic Resonance Line Narrowing by a Rotating rf Field. Physical Review Letters 11 (1963) 255-258.

[55] W.K. Rhim, A. Pines, and J.S. Waugh, Violation of the Spin-Temperature Hypothesis. Physical Review Letters 25 (1970) 218.

[56] J.S. Waugh, L.M. Huber, and U. Haeberlen, Approach to High-Resolution nmr in Solids. Physical Review Letters 20 (1968) 180-182.

[57] M.F. Mesleh, G. Veglia, T.M. DeSilva, F.M. Marassi, and S.J. Opella, Dipolar waves as NMR maps of protein structure. J. Am. Chem. Soc. 124 (2002) 4206-7.

[58] F.M. Marassi, and S.J. Opella, Using pisa pies to resolve ambiguities in angular constraints from PISEMA spectra of aligned proteins. J. Biomol. NMR 23 (2002) 239-42.

[59] F.M. Marassi, and S.J. Opella, A solid-state NMR index of helical membrane protein structure and topology. J. Magn. Reson. 144 (2000) 150-5.

[60] C.H. Wu, and S.J. Opella, Shiftless nuclear magnetic resonance spectroscopy. J. Chem. Phys. 128 (2008) 052312.

[61] S.H. Park, A.A. Mrse, A.A. Nevzorov, A.A. De Angelis, and S.J. Opella, Rotational diffusion of membrane proteins in aligned phospholipid bilayers by solid-state NMR spectroscopy. J. Magn. Reson. 178 (2006) 162-5.

[62] M.H. Levitt, Symmetry in the design of NMR multiple-pulse sequences. J. Chem. Phys. 128 (2008) 052205.

[63] Y.K. Lee, N.D. Kurur, M. Helmle, O.G. Johannessen, N.C. Nielsen, and M.H. Levitt, Efficient dipolar recoupling in the NMR of rotating solids. A sevenfold symmetric radiofrequency pulse sequence. Chem. Phys. Lett. 242 (1995) 304-309.

[64] M.H. Levitt, Symmetrical composite pulse sequences for NMR population inversion. II. Compensation of resonance offset. J. Magn. Reson. 50 (1982) 95-110.

[65] B.B. Das, H. Zhang, and S.J. Opella, Dipolar Assisted Assignment Protocol (DAAP) for MAS solid-state NMR of rotationally aligned membrane proteins in phospholipid bilayers. J. Magn. Reson. 242 (2014) 224-232.

[66] J.G. Magadán, and J.S. Bonifacino, Transmembrane domain determinants of CD4 Downregulation by HIV-1 Vpu. Journal of virology 86 (2012) 757-772.

[67] R. Willey, F. Maldarelli, M. Martin, and K. Strebel, Human immunodeficiency virus type 1 Vpu protein induces rapid degradation of CD4. Journal of virology 66 (1992) 7193-7200.

[68] B. Sowrirajan, and E. Barker, The Natural Killer Cell Cytotoxic Function Is Modulated by HIV-1 Accessory Proteins. Viruses 3 (2011) 1091-1111.

[69] A.H. Shah, B. Sowrirajan, Z.B. Davis, J.P. Ward, E.M. Campbell, V. Planelles, and E. Barker, Degranulation of Natural Killer Cells Following Interaction with HIV-1-Infected Cells Is Hindered by Downmodulation of NTB-A by Vpu. Cell Host & Microbe 8 (2010) 397-409.

[70] J. Richard, and É.A. Cohen, HIV-1 Vpu Disarms Natural Killer Cells. Cell Host & Microbe 8 (2010) 389-391.

[71] M. Meselson, and F. Stahl, The replication of DNA in Escherichia coli. Proceedings of the National Academy of Sciences of the United States of America 44 (1958) 671.

[72] T.A. Cross, J.A. DiVerdi, and S.J. Opella, Strategy for nitrogen NMR analysis of biopolymers. J. Am. Chem. Soc. 104 (1982) 1759-1761.

[73] M. Ikura, L.E. Kay, and A. Bax, A novel approach for sequential assignment of proton, carbon-13, and nitrogen-15 spectra of larger proteins: heteronuclear triple-

resonance three-dimensional NMR spectroscopy. Application to calmodulin. Biochemistry 29 (1990) 4659-4667.

[74] A. McDermott, T. Polenova, A. Bockmann, K.W. Zilm, E.K. Paulsen, R.W. Martin, and G.T. Montelione, Partial NMR assignments for uniformly (13C, 15N)-enriched BPTI in the solid state. J. Biomol. NMR 16 (2000) 209-219.

[75] D.M. Schneider, R. Tycko, and S.J. Opella, High-resolution solid-state triple nuclear magnetic resonance measurement of 13C-15N dipole-dipole couplings. J. Magn. Reson. 73 (1987) 568-573.

[76] J.S. Waugh, Uncoupling of local field spectra in nuclear magnetic resonance: Determination of atomic position in solids. Proc Natl Acad Sci U S A 73 (1976) 1394-1397.

[77] Z. Gu, and S.J. Opella, Three-dimensional 13C shift/1H-15N coupling/15N shift solid-state NMR correlation spectroscopy. J. Magn. Reson. 138 (1999) 193-198.

[78] N. Sinha, F.V. Filipp, L. Jairam, S.H. Park, J. Bradley, and S.J. Opella, Tailoring 13C labeling for triple-resonance solid-state NMR experiments on aligned samples of proteins. Magn. Reson. Chem. 45 Suppl 1 (2007) S107-115.

[79] G. Pake, Nuclear resonance absorption in hydrated crystals: fine structure of the proton line. J. Chem. Phys. 16 (1948) 327.

[80] A.A. Nevzorov, and S.J. Opella, Selective averaging for high-resolution solid-state NMR spectroscopy of aligned samples. J. Magn. Reson. 185 (2007) 59-70.

[81] S. Opella, and J. Waugh, Two-dimensional 13 C NMR of highly oriented polyethylene. J. Chem. Phys. 66 (1977) 4919-4924.

[82] T.A. Cross, and S.J. Opella, Protein structure by solid-state NMR. J. Am. Chem. Soc. 105 (1983) 306-308.

[83] Z.T. Gu, and S.J. Opella, Two- and three-dimensional 1H/13C PISEMA experiments and their application to backbone and side chain sites of amino acids and peptides. J. Magn. Reson. 140 (1999) 340-346.

[84] Y. Ishii, and R. Tycko, Multidimensional Heteronuclear Correlation Spectroscopy of a Uniformly 15N- and 13C-Labeled Peptide Crystal:‚Äâ Toward Spectral Resolution, Assignment, and Structure Determination of Oriented Molecules in Solid-State NMR. J. Am. Chem. Soc. 122 (2000) 1443-1455.

[85] N. Sinha, C.V. Grant, K.S. Rotondi, L. Feduik-Rotondi, L.M. Gierasch, and S.J. Opella, Peptides and the development of double- and triple-resonance solid-state NMR of aligned samples. J. Pept. Res. 65 (2005) 605-620.

[86] A. Pines, M. Gibby, and J. Waugh, Proton enhanced NMR of dilute spins in solids. J. Chem. Phys. 59 (1973) 569-590.

[87] W. Rhim, D. Elleman, and R. Vaughan, Analysis of multiple pulse NMR in solids. J. Chem. Phys. 59 (1973) 3740-3749.

[88] U. Haeberlen, and J.S. Waugh, Coherent Averaging Effects in Magnetic Resonance. Physical Review 175 (1968) 453-467.

[89] N. Sinha, C.V. Grant, S.H. Park, J.M. Brown, and S.J. Opella, Triple resonance experiments for aligned sample solid-state NMR of (13)C and (15)N labeled proteins. J. Magn. Reson. 186 (2007) 51-64.

[90] C.V. Grant, C.H. Wu, and S.J. Opella, Probes for high field solid-state NMR of lossy biological samples. J. Magn. Reson. 204 (2010) 180-188.

[91] C.V. Grant, Y. Yang, M. Glibowicka, C.H. Wu, S.H. Park, C.M. Deber, and S.J. Opella, A Modified Alderman-Grant Coil makes possible an efficient cross-coil probe for high field solid-state NMR of lossy biological samples. J. Magn. Reson. 201 (2009) 87-92.

[92] V. Cross, R. Hester, and J. Waugh, Single coil probe with transmission line tuning for nuclear magnetic double resonance. Review of Scientific Instruments 47 (1976) 1486.

[93] N. Sinha, C. Grant, C. Wu, A. De Angelis, S. Howell, and S. Opella, SPINAL modulated decoupling in high field double-and triple-resonance solid-state NMR experiments on stationary samples. J. Magn. Reson. 177 (2005) 197-202.

[94] F.D. Doty, R.R. Inners, and P.D. Ellis, A multinuclear double-tuned probe for applications with solids or liquids utilizing lumped tuning elements. Journal of Magnetic Resonance (1969) 43 (1981) 399-416.

[95] R. Martin, E. Paulson, and K. Zilm, Design of a triple resonance magic angle sample spinning probe for high field solid state nuclear magnetic resonance. Review of Scientific Instruments 74 (2003) 3045.

[96] F.M. Marassi, C. Ma, H. Gratkowski, S.K. Straus, K. Strebel, M. Oblatt-Montal, M. Montal, and S.J. Opella, Correlation of the structural and functional domains in the membrane protein Vpu from HIV-1. Proc. Natl. Acad. Sci. USA 96 (1999) 14336-41.

[97] S.H. Park, S. Prytulla, A.A. De Angelis, J.M. Brown, H. Kiefer, and S.J. Opella, High-resolution NMR spectroscopy of a GPCR in aligned bicelles. J. Am. Chem. Soc. 128 (2006) 7402-3.

[98] A.A. De Angelis, S.C. Howell, A.A. Nevzorov, and S.J. Opella, Structure determination of a membrane protein with two trans-membrane helices in aligned phospholipid bicelles by solid-state NMR spectroscopy. J. Am. Chem. Soc. 128 (2006) 12256-67.

[99] G.A. Cook, and S.J. Opella, NMR studies of p7 protein from hepatitis C virus. Eur. Biophys. J. 39 (2009) 1097-104.

[100] S.J. Opella, A.C. Zeri, and S.H. Park, Structure, dynamics, and assembly of filamentous bacteriophages by nuclear magnetic resonance spectroscopy. Annu. Rev. Phys. Chem. 59 (2008) 635-57.

[101] M.J. Baryro, T. Maly, N.R. Birkett, C.E. Bacphee, D. C.M., and R.G. Griffin, High-Resolution MAS NMR Analysis of PI3-SH3 Amyloid Fibrils: Backbone Conformation and Implications for Protofilament Assembly and Structure. Biochemistry 49 (2010) 7474-84.

[102] A.A. De Angelis, A.A. Nevzorov, S.H. Park, S.C. Howell, A.A. Mrse, and S.J. Opella, High-Resolution NMR Spectroscopy of Membrane Proteins in Aligned Bicelles. J. Am. Chem. Soc. 126 (2004) 15340-15341.

[103] N. Tjandra, and A. Bax, Direct Measurement of Distances and Angles in Biomolecules by NMR in a Dilute Liquid Crystalline Medium. Science 278 (1997) 1111-1114.

[104] T.A. Cross, J.A. DiVerdi, and S.J. Opella, Strategy for nitrogen NMR of biopolymers. J. Am. Chem. Soc. 104 (1982) 1759-1761.

[105] A.A. Nevzorov, and S.J. Opella, A "magic sandwich" pulse sequence with reduced offset dependence for high-resolution separated local field spectroscopy. J. Magn. Reson. 164 (2003) 182-6.

[106] C.H. Wu, and S.J. Opella, Proton-detected separated local field spectroscopy. J. Magn. Reson. 190 (2008) 165-170.

[107] C.H. Wu, and S.J. Opella, Shiftless nuclear magnetic resonance spectroscopy. J. Chem. Phys. 128 (2008) 052312.

[108] M.F. Mesleh, G. Veglia, T.M. DeSilva, F.M. Marassi, and S.J. Opella, Dipolar waves as NMR maps of protein structure. J. Am. Chem. Soc. 124 (2002) 4206-7.

[109] F.M. Marassi, and S.J. Opella, A solid-state NMR index of helical membrane protein structure and topology. J. Magn. Reson. 144 (2000) 150-5.

[110] A.A. Nevzorov, Mismatched Hartmann-Hahn Conditions Cause Proton-Mediated Intermolecular Magnetization Transfer between Dilute Low-Spin Nuclei in NMR of Static Solids. J. Am. Chem. Soc. 130 (2008) 11282-11283.

[111] N. Sinha, F.V. Filipp, L. Jairam, S.H. Park, J. Bradley, and S.J. Opella, Tailoring 13C labeling for triple-resonance solid-state NMR experiments on aligned samples of proteins. Magn. Reson. Chem. 45 Suppl 1 (2007) S107-115.

[112] E.C. Lin, C.H. Wu, Y. Yang, C.V. Grant, and S.J. Opella, 1H-13C separated local field spectroscopy of uniformly 13C labeled peptides and proteins. J. Magn. Reson. 206 (2010) 105-111.

[113] A. Pines, M.G. Gibby, and J.S. Waugh, Proton-enhanced nuclear induction spectroscopy. A method for high-resolution NMR of dilute spins in solids. J. Chem. Phys. 56 (1972) 1776-7.

[114] A. Pines, M. Gibby, and J. Waugh, Proton enhanced NMR of dilute spins in solids. J. Chem. Phys. 59 (1973) 569-590.

[115] J. Schaefer, R.A. McKay, and E.O. Stejskal, Double-cross-polarization NMR of solids. J. Magn. Reson. 34 (1979) 443-447.

[116] A. Ramamoorthy, C.H. Wu, and S.J. Opella, Three-dimensional solid-state NMR experiment that correlates the chemical shift and dipolar coupling frequencies of two heteronuclei. J. Magn. Reson. B107 (1995) 88-90.

[117] A.A. Nevzorov, S.H. Park, and S.J. Opella, Three-dimensional experiment for solid-state NMR of aligned protein samples in high field magnets. J. Biomol. NMR 37 (2007) 113-6.

[118] J. Xu, R. Soong, S.-C. Im, L. Waskell, and A. Ramamoorthy, INEPT-Based Separated-Local-Field NMR Spectroscopy: A Unique Approach To Elucidate Side-Chain Dynamics of Membrane-Associated Proteins. J. Am. Chem. Soc. 132 (2010) 9944-9947.

[119] J.R. Lewandowski, G. De Paëpe, and R.G. Griffin, Proton Assisted Insensitive Nuclei Cross Polarization. J. Am. Chem. Soc. 129 (2007) 728-729.

[120] N. Sinha, C.V. Grant, C.H. Wu, A.A. De Angelis, S.C. Howell, and S.J. Opella, SPINAL modulated decoupling in high field double- and triple-resonance solid-state NMR experiments on stationary samples. J. Magn. Reson. 177 (2005) 197-202.

[121] M. Bak, J. Rasmussen, and N. Nielsen, SIMPSON: a general simulation program for solid-state NMR spectroscopy. J. Magn. Reson. 147 (2000) 296-330.

[122] L. Müller, A. Kumar, T. Baumann, and R.R. Ernst, Transient Oscillations in NMR Cross-Polarization Experiments in Solids. Phys. Rev. Lett. 32 (1974) 1402.

[123] D.S. Thiriot, A.A. Nevzorov, and S.J. Opella, Structural basis of the temperature transition of Pf1 bacteriophage. Protein Sci. 14 (2005) 1064-70.

[124] D.S. Thiriot, A.A. Nevzorov, L. Zagyanskiy, C.H. Wu, and S.J. Opella, Structure of the coat protein in Pf1 bacteriophage determined by solid-state NMR spectroscopy. J. Mol. Biol. 341 (2004) 869-79.

[125] K.R. Thurber, and R. Tycko, Biomolecular solid state NMR with magic-angle spinning at 25 K. J. Magn. Reson. 195 (2008) 179-186.

[126] J.C. Hoch, and A.S. Stern, NMR Data Processing, Wiley-Liss, New York, 1996.

[127] D.H. Jones, and S.J. Opella, Application of Maximum Entropy reconstruction to PISEMA spectra. J. Magn. Reson. 179 (2006) 105-13.

[128] S. Sun, S. Yan, C. Guo, M. Li, J.C. Hoch, J.C. Williams, and T. Polenova, A Time-Saving Strategy for MAS NMR Spectroscopy by Combining Nonuniform Sampling and Paramagnetic Relaxation Assisted Condensed Data Collection. J. Phys. Chem. B 116 (2012) 13585-13596.

[129] S. Paramasivam, C.L. Suiter, G. Hou, S. Sun, M. Palmer, J.C. Hoch, D. Rovnyak, and T. Polenova, Enhanced Sensitivity by Nonuniform Sampling Enables Multidimensional MAS NMR Spectroscopy of Protein Assemblies. J. Phys. Chem. B 116 (2012) 7416-7427.

[130] Ē. Kupče, and R. Freeman, Projection-Reconstruction Technique for Speeding up Multidimensional NMR Spectroscopy. J. Am. Chem. Soc. 126 (2004) 6429-6440.

[131] Ē. Kupče, and R. Freeman, The radon transform: A new scheme for fast multidimensional NMR. Concept. Magnetic. Res. A 22A (2004) 4-11.

[132] H.S. Atreya, E. Garcia, Y. Shen, and T. Szyperski, J-GFT NMR for Precise Measurement of Mutually Correlated Nuclear Spin-Spin Couplings. J. Am. Chem. Soc. 129 (2006) 680-692.

[133] K. Kazimierczuk, A. Zawadzka, W. Koźmiński, and I. Zhukov, Random sampling of evolution time space and Fourier transform processing. J. Biomol. NMR 36 (2006) 157-168.

[134] M.T. Eddy, D. Ruben, R.G. Griffin, and J. Herzfeld, Deterministic schedules for robust and reproducible non-uniform sampling in multidimensional NMR. J. Magn. Reson. 214 (2012) 296-301.

[135] Y. Matsuki, M.T. Eddy, R.G. Griffin, and J. Herzfeld, Rapid Three-Dimensional MAS NMR Spectroscopy at Critical Sensitivity. Angew. Chem. Int. Edit. Engl. 49 (2010) 9215-9218.

[136] Y. Matsuki, M.T. Eddy, and J. Herzfeld, Spectroscopy by Integration of Frequency and Time Domain Information for Fast Acquisition of High-Resolution Dark Spectra. J. Am. Chem. Soc. 131 (2009) 4648-4656.

[137] A.S. Stern, D.L. Donoho, and J.C. Hoch, NMR data processing using iterative thresholding and minimum l1-norm reconstruction. J. Magn. Reson. 188 (2007) 295-300.

[138] D.J. Holland, M.J. Bostock, L.F. Gladden, and D. Nietlispach, Fast multidimensional NMR spectroscopy using compressed sensing. Angew. Chem. Int. Edit. Engl. 123 (2011) 6678-6681.

[139] Y. Shrot, and L. Frydman, Spatial/spectral encoding of the spin interactions in ultrafast multidimensional NMR. J. Chem. Phys. 131 (2009) 224516.

[140] M. Bostock, D. Holland, and D. Nietlispach, Compressed sensing reconstruction of undersampled 3D NOESY spectra: application to large membrane proteins. J. Biomol. NMR 54 (2012) 15-32.

[141] S. Hyberts, A. Milbradt, A. Wagner, H. Arthanari, and G. Wagner, Application of iterative soft thresholding for fast reconstruction of NMR data non-uniformly sampled with multidimensional Poisson Gap scheduling. J. Biomol. NMR 52 (2012) 315-327.

[142] K. Kazimierczuk, A. Zawadzka, and W. Kozminski, Optimization of random time domain sampling in multidimensional NMR. J. Magn. Reson. 192 (2008) 123-130.

[143] M. Mobli, A.S. Stern, and J.C. Hoch, Spectral reconstruction methods in fast NMR: Reduced dimensionality, random sampling and maximum entropy. J. Magn. Reson. 182 (2006) 96-105.

[144] S.G. Hyberts, K. Takeuchi, and G. Wagner, Poisson-Gap Sampling and Forward Maximum Entropy Reconstruction for Enhancing the Resolution and Sensitivity of Protein NMR Data. J. Am. Chem. Soc. 132 (2010) 2145-2147.

[145] S. Hyberts, D. Frueh, H. Arthanari, and G. Wagner, FM reconstruction of non-uniformly sampled protein NMR data at higher dimensions and optimization by distillation. J. Biomol. NMR 45 (2009) 283-294.

[146] S. Hyberts, H. Arthanari, and G. Wagner, Applications of Non-Uniform Sampling and Processing. Top. Curr. Chem. (2011) 1-24.

[147] C.A. Waudby, and J. Christodoulou, An analysis of NMR sensitivity enhancements obtained using non-uniform weighted sampling, and the application to protein NMR. J. Magn. Reson. (2012).

[148] D. Rovnyak, M. Sarcone, and Z. Jiang, Sensitivity enhancement for maximally resolved two-dimensional NMR by nonuniform sampling. Magn. Reson. Chem. 49 (2011) 483-491.

[149] M. Mobli, M.W. Maciejewski, A.D. Schuyler, A.S. Stern, and J.C. Hoch, Sparse Sampling Methods In Multidimensional NMR. Phys. Chem. Chem. Phys. 14 (2012) 10835-10843.

[150] G.J. Lu, S.H. Park, and S.J. Opella, Improved 1H amide resonance line narrowing in oriented sample solid-state NMR of membrane proteins in phospholipid bilayers. J. Magn. Reson. 220 (2012) 54-61.

[151] F. Delaglio, S. Grzesiek, G.W. Vuister, G. Zhu, J. Pfeifer, and A. Bax, NMRPipe: a multidimensional spectral processing system based on UNIX pipes. J. Biomol. NMR 6 (1995) 277-293.

[152] K. Takegoshi, S. Nakamura, and T. Terao, 13C-1H dipolar-assisted rotational resonance in magic-angle spinning NMR. Chem. Phys. Lett. 344 (2001) 631-637.

[153] W. Tang, and A.A. Nevzorov, Repetitive cross-polarization contacts via equilibration-re-equilibration of the proton bath: Sensitivity enhancement for NMR of membrane proteins reconstituted in magnetically aligned bicelles. J. Magn. Reson. 212 (2011) 245-248.

[154] A.A. Nevzorov, Ergodicity and efficiency of cross-polarization in NMR of static solids. J. Magn. Reson. 209 (2011) 161-166.

[155] G.J. Lu, Y. Tian, N. Vora, F.M. Marassi, and S.J. Opella, The Structure of the Mercury Transporter MerF in Phospholipid Bilayers: A Large Conformational Rearrangement Results From N-terminal Truncation. J. Am. Chem. Soc. (2013).

[156] S.H. Park, C. Loudet, F.M. Marassi, E.J. Dufourc, and S.J. Opella, Solid-state NMR spectroscopy of a membrane protein in biphenyl phospholipid bicelles with the bilayer normal parallel to the magnetic field. J. Magn. Reson. 193 (2008) 133-8.

[157] G.J. Lu, W.S. Son, and S.J. Opella, A general assignment method for oriented sample (OS) solid-state NMR of proteins based on the correlation of resonances through heteronuclear dipolar couplings in samples aligned parallel and perpendicular to the magnetic field. J. Magn. Reson. 209 (2011) 195-206.

[158] T. Cross, M. Frey, and S. Opella, Nitrogen-15 spin exchange in a protein. J. Am. Chem. Soc. 105 (1983) 7471-7473.

[159] V. Orekhov, I. Ibraghimov, and M. Billeter, MUNIN: A new approach to multi-dimensional NMR spectra interpretation. J. Biomol. NMR 20 (2001) 49-60-60.

[160] E.C. Lin, and S.J. Opella, Sampling scheme and compressed sensing applied to solid-state NMR spectroscopy. J. Magn. Reson. 237 (2013) 40-48.

[161] D.J. States, R.A. Haberkorn, and D.J. Ruben, A two-dimensional nuclear overhauser experiment with pure absorption phase in four quadrants. J. Magn. Reson. 48 (1982) 286-292.

[162] B. Hu, J.-P. Amoureux, J. Trebosc, M. Deschamps, and G. Tricot, Solid-state NMR covariance of homonuclear correlation spectra. J. Chem. Phys. 128 (2008) 134502-8.

[163] K. Takeda, Y. Kusakabe, Y. Noda, M. Fukuchi, and K. Takegoshi, Homo- and heteronuclear two-dimensional covariance solid-state NMR spectroscopy with a dual-receiver system. Phys. Chem. Chem. Phys. 14 (2012) 9715-9721.

[164] Y. Li, B. Hu, Q. Chen, Q. Wang, Z. Zhang, J. Yang, I. Noda, J. Trebosc, O. Lafon, J.-P. Amoureux, and F. Deng, Comparison of various sampling schemes and accumulation profiles in covariance spectroscopy with exponentially decaying 2D signals. Analyst 138 (2013) 2411-2419.

[165] R.W. Knox, G.J. Lu, S.J. Opella, and A.A. Nevzorov, A Resonance Assignment Method for Oriented-Sample Solid-State NMR of Proteins. J. Am. Chem. Soc. 132 (2010) 8255-8257.

[166] W. Tang, R. Knox, and A. Nevzorov, A spectroscopic assignment technique for membrane proteins reconstituted in magnetically aligned bicelles. J. Biomol. NMR 54 (2012) 307-316.

[167] B. Hu, J.-P. Amoureux, and J. Trebosc, Indirect covariance NMR spectroscopy of through-bond homo-nuclear correlations for quadrupolar nuclei in solids under high-resolution. Solid State Nuclear Magnetic Resonance 31 (2007) 163-168.

[168] S. Dvinskikh, K. Yamamoto, and A. Ramamoorthy, Heteronuclear isotropic mixing separated local field NMR spectroscopy. J. Chem. Phys. 125 (2006) 034507.

[169] S. Caldarelli, M. Hong, L. Emsley, and A. Pines, Measurement of Carbon-Proton Dipolar Couplings in Liquid Crystals by Local Dipolar Field NMR Spectroscopy. J. Phys. Chem. 100 (1996) 18696-18701.

[170] P. Robyr, B.H. Meier, and R.R. Ernst, Radio-frequency-driven nuclear spin diffusion in solids. Chem. Phys. Lett. 162 (1989) 417-423.

[171] N. Van Damme, D. Goff, C. Katsura, R.L. Jorgenson, R. Mitchell, M. Johnson, E.B. Stephens, and J. Guatelli, The interferon-induced protein BST-2/CD317 restricts release of virions from infected cells and is down-regulated from the cell surface by HIV-1 Vpu. Cell host & microbe 3 (2008) 245-252.

[172] R.S. Mitchell, C. Katsura, M.A. Skasko, K. Fitzpatrick, D. Lau, A. Ruiz, E.B. Stephens, F. Margottin-Goguet, R. Benarous, and J.C. Guatelli, Vpu Antagonizes BST-2–Mediated Restriction of HIV-1 Release via β-TrCP and Endo-Lysosomal Trafficking. PLoS Pathog 5 (2009) e1000450.

[173] M. Skasko, Y. Wang, Y. Tian, A. Tokarev, J. Munguia, A. Ruiz, E.B. Stephens, S.J. Opella, and J. Guatelli, HIV-1 Vpu Protein Antagonizes Innate Restriction

Factor BST-2 via Lipid-embedded Helix-Helix Interactions. J. Biol. Chem. 287 (2012) 58-67.

[174] E. Tiganos, X.-J. Yao, J. Friborg, N. Daniel, and E.A. Cohen, Putative alpha-helical structures in the human immunodeficiency virus type 1 Vpu protein and CD4 are involved in binding and degradation of the CD4 molecule. Journal of virology 71 (1997) 4452-4460.

[175] M. Hart, J. Concordet, I. Lassot, I. Albert, R. Del los Santos, H. Durand, C. Perret, B. Rubinfeld, F. Margottin, and R. Benarous, The F-box protein β-TrCP associates with phosphorylated β-catenin and regulates its activity in the cell. Current biology 9 (1999) 207-211.

[176] H.-M. Tervo, S. Homann, I. Ambiel, J.V. Fritz, O.T. Fackler, and O.T. Keppler, b-TrCP is dispensable for Vpu's ability to overcome the CD317/Tetherin-imposed restriction to HIV-1 release. Retrovirology 8 (2011).

[177] E. Miyagi, A.J. Andrew, S. Kao, and K. Strebel, Vpu enhances HIV-1 virus release in the absence of Bst-2 cell surface down-modulation and intracellular depletion. Proceedings of the National Academy of Sciences 106 (2009) 2868-2873.

[178] C. Goffinet, S. Homann, I. Ambiel, N. Tibroni, D. Rupp, O.T. Keppler, and O.T. Fackler, Antagonism of CD317 restriction of human immunodeficiency virus type 1 (HIV-1) particle release and depletion of CD317 are separable activities of HIV-1 Vpu. Journal of virology 84 (2010) 4089-4094.

[179] A.A. Tokarev, J. Munguia, and J.C. Guatelli, Serine-Threonine Ubiquitination Mediates Downregulation of BST-2/Tetherin and Relief of Restricted Virion Release by HIV-1 Vpu. Journal of Virology 85 (2011) 51-63.

[180] T. Kerkau, I. Bacik, J.R. Bennink, J.W. Yewdell, T. Hünig, A. Schimpl, and U. Schubert, The human immunodeficiency virus type 1 (HIV-1) Vpu protein interferes with an early step in the biosynthesis of major histocompatibility complex (MHC) class I molecules. The Journal of experimental medicine 185 (1997) 1295-1306.

[181] M. Jafari, J. Guatelli, and M.K. Lewinski, Activities of Transmitted/Founder and Chronic Clade B HIV-1 Vpu and a C-Terminal Polymorphism Specifically Affecting Virion Release. Journal of Virology 88 (2014) 5062-5078.

[182] M.W. McNatt, T. Zang, and P.D. Bieniasz, Vpu Binds Directly to Tetherin and Displaces It from Nascent Virions. PLoS Pathog 9 (2013) e1003299.

[183] S.H. Park, A.A. Mrse, A.A. Nevzorov, M.F. Mesleh, M. Oblatt-Montal, M. Montal, and S.J. Opella, Three-dimensional structure of the channel-forming trans-membrane domain of virus protein "u" (Vpu) from HIV-1. J. Mol. Biol. 333 (2003) 409-24.

[184] S.H. Park, A.A. De Angelis, A.A. Nevzorov, C.H. Wu, and S.J. Opella, Three-dimensional structure of the transmembrane domain of Vpu from HIV-1 in aligned phospholipid bicelles. Biophys. J. 91 (2006) 3032-42.

[185] V. Wray, D. Mertins, M. Kiess, P. Henklein, W. Trowitzsch-Kienast, and U. Schubert, Solution Structure of the Cytoplasmic Domain of the Human CD4 Glycoprotein by CD and 1H NMR Spectroscopy: Implications for Biological Functions. Biochemistry 37 (1998) 8527-8538.

[186] T. FEDERAU, U. SCHUBERT, J. FLOßDORF, P. HENKLEIN, D. SCHOMBURG, and V. WRAY, Solution structure of the cytoplasmic domain of the human immunodeficiency virus type 1 encoded virus protein U (Vpu). International journal of peptide and protein research 47 (1996) 297-310.

[187] M. Wittlich, B.W. Koenig, M. Stoldt, H. Schmidt, and D. Willbold, NMR structural characterization of HIV-1 virus protein U cytoplasmic domain in the presence of dodecylphosphatidylcholine micelles. FEBS Journal 276 (2009) 6560-6575.

[188] C. Ma, F.M. Marassi, D.H. Jones, S.K. Straus, S. Bour, K. Strebel, U. Schubert, M. Oblatt-Montal, M. Montal, and S.J. Opella, Expression, purification, and activities of full-length and truncated versions of the integral membrane protein Vpu from HIV-1. Protein Sci. 11 (2002) 546-57.

[189] D.H. Jones, and S.J. Opella, Weak alignment of membrane proteins in stressed polyacrylamide gels. J. Magn. Reson. 171 (2004) 258-69.

[190] J.L. Battiste, and G. Wagner, Utilization of site-directed spin labeling and high-resolution heteronuclear nuclear magnetic resonance for global fold determination of large proteins with limited nuclear overhauser effect data. Biochemistry 39 (2000) 5355-5365.

[191] N. Bloembergen, On the interaction of nuclear spins in a crystalline lattice. Physica 15 (1949) 386-426.

[192] K. Takegoshi, S. Nakamura, and T. Terao, 13C–1H dipolar-driven 13C–13C recoupling without 13C rf irradiation in nuclear magnetic resonance of rotating solids. J. Chem. Phys. 118 (2003) 2325-2341.

[193] M. Baldus, A.T. Petkova, J. Herzfeld, and R.G. Griffin, Cross polarization in the tilted frame: assignment and spectral simplification in heteronuclear spin systems. Mol. Phys. 95 (1998) 1197 - 1207.

[194] X. Zhao, M. Edén, and M.H. Levitt, Recoupling of heteronuclear dipolar interactions in solid-state NMR using symmetry-based pulse sequences. Chem. Phys. Lett. 342 (2001) 353-361.

[195] L. Whitmore, and B. Wallace, DICHROWEB, an online server for protein secondary structure analyses from circular dichroism spectroscopic data. Nucleic acids research 32 (2004) W668-W673.

[196] L. Whitmore, and B.A. Wallace, Protein secondary structure analyses from circular dichroism spectroscopy: methods and reference databases. Biopolymers 89 (2008) 392-400.

[197] Y. Shen, F. Delaglio, G. Cornilescu, and A. Bax, TALOS+: a hybrid method for predicting protein backbone torsion angles from NMR chemical shifts. J. Biomol. NMR 44 (2009) 213-223.

[198] X.-M. Gong, Y. Ding, J. Yu, Y. Yao, and F.M. Marassi, Structure of the Na, K-ATPase regulatory protein FXYD2b in micelles: Implications for membrane–water interfacial arginines. Biochimica et Biophysica Acta (BBA)-Biomembranes 1848 (2015) 299-306.

[199] M.F. Mesleh, S. Lee, G. Veglia, D.S. Thiriot, F.M. Marassi, and S.J. Opella, Dipolar waves map the structure and topology of helices in membrane proteins. J. Am. Chem. Soc. 125 (2003) 8928-35.

[200] B. Liang, J.H. Bushweller, and L.K. Tamm, Site-Directed Parallel Spin-Labeling and Paramagnetic Relaxation Enhancement in Structure Determination of

Membrane Proteins by Solution NMR Spectroscopy. J. Am. Chem. Soc. 128 (2006) 4389-4397.

[201] L.E. Kay, D.A. Torchia, and A. Bax, Backbone dynamics of proteins as studied by nitrogen-15 inverse detected heteronuclear NMR spectroscopy: application to staphylococcal nuclease. Biochemistry 28 (1989) 8972-8979.

[202] N.A. Farrow, R. Muhandiram, A.U. Singer, S.M. Pascal, C.M. Kay, G. Gish, S.E. Shoelson, T. Pawson, J.D. Forman-Kay, and L.E. Kay, Backbone dynamics of a free and a phosphopeptide-complexed Src homology 2 domain studied by 15N NMR relaxation. Biochemistry 33 (1994) 5984-6003.

[203] M. Hong, and T. Doherty, Orientation determination of membrane-disruptive proteins using powder samples and rotational diffusion: A simple solid-state NMR approach. Chem. Phys. Lett. 432 (2006) 296-300.

[204] B.A. Lewis, G.S. Harbison, J. Herzfeld, and R.G. Griffin, NMR structural analysis of a membrane protein: bacteriorhodopsin peptide backbone orientation and motion. Biochemistry 24 (1985) 4671-4679.

[205] R.F. Campbell, E. Meirovitch, and J.H. Freed, Slow-motional NMR line shapes for very anisotropic rotational diffusion. Phosphorus-31 NMR of phospholipids. J. Phys. Chem. 83 (1979) 525-533.

[206] J. Leppert, O. Ohlenschläger, M. Görlach, and R. Ramachandran, Adiabatic TOBSY in rotating solids. J. Biomol. NMR 29 (2004) 167-173.

[207] A. Lesage, M. Bardet, and L. Emsley, Through-bond carbon-carbon connectivities in disordered solids by NMR. J. Am. Chem. Soc. 121 (1999) 10987-10993.

[208] F.M. Marassi, C. Ma, J.J. Gesell, and S.J. Opella, Three-dimensional solid-state NMR spectroscopy is essential for resolution of resonances from in-plane residues in uniformly (15)N-labeled helical membrane proteins in oriented lipid bilayers. J. Magn. Reson. 144 (2000) 156-61.